Acoustic confinement of *Escherichia coli*

The impact on biofilm formation

Salomé Gutiérrez Ramos

Department of Engineering and Biomedical Physics
Centro de Investigacion y de Estudios Avanzados.
Unidad Monterrey

This dissertation is submitted for the degree of
Doctor of Philosophy in Engineering and Biomedical Physics

July 2018

It is not the voice that commands the story; it is the ear.

Declaration

I declare that this thesis has been composed solely by myself and that it has not been submitted, in whole or in part, in any previous application for a degree. Except where states otherwise by reference or acknowledgment, the work presented is entirely my own.

Salomé Gutiérrez Ramos
July 2018

Acknowledgements

“Where is the wisdom we have lost in knowledge?
Where is the knowledge we have lost in infomation?”

This T.S. Elliot quote has followed me throughout my life, wondering constantly this was my basal state. Luckily, thanks to this work I met the people that gave me the answers.

Dr.Aimee Wessel and Dr.Ramiro Godoy-Diana I lack to words to acknowledge everything that you did for me and this work. Thank you for your academic support, guidance but above all thank you from make me believe in the possibilities of making good science.

Dr.Carlos-Ruiz Suarez thank you for giving me the opportunity to work on your team and to enable me to go at the beginning of this work with Dr. Hoyos’s team. Your support during these years is immeasurable and I deeply appreciate it.

Also, I would like to acknowledgment my old and new friends that acted as a very efficient support system. And above all, to my family.

Finally, I appreaciated the economical help provided by CONACYT and the "Aide spécifique aux doctorants boursier" provided by Sorbonne Université.

Abstract

Brownian or self-propelled particles in aqueous suspensions can be trapped by acoustic fields generated by piezoelectric transducers usually at frequencies in the megahertz. The obtained confinement allows the study of rich collective behaviours like clustering or spreading dynamics in microgravity-like conditions. The acoustic field induces the levitation of self-propelled particles and provides secondary lateral forces to capture them at nodal planes. Here, we give a step forward in the field of confined active matter, reporting levitation experiments of bacterial suspensions of *Escherichia coli*. Clustering of living bacteria is monitored as a function of time, where different behaviours are clearly distinguished. Upon the removal of the acoustic signal, bacteria rapidly spread, impelled by their own swimming. Trapping of diverse bacteria phenotypes result in irreversible bacteria entanglements and in the formation of free-floating biofilms

Table of contents

List of figures

Chapter 1

Introduction

It has been four years since the World Health Organization warned us of the imminent arrival of *a post-antibiotic era*—-in which common infections and minor injuries could kill [128].

This year reports shows that, indeed, this was not an apocalyptic fantasy but rather a twenty-first century reality [129, 168]. The presence of *superbugs* (drug resistant microorganisms) has spread all over Earth; where drug-resistant tuberculosis, malaria and HIV are more common than ever [168]. The emergence of drug-resistant diseases is often related to the presence of persistent bacteria [33, 96, 173], mutation of microorganisms via gene transfer [40, 188], or the presence of complex communities of bacteria [86, 141], known as biofilms, that make difficult to eradicate of these microorganisms.

Even when the term biofilm may not form part of the popular lexicon, most people are familiar with biofilms in one way or another [172]. For example, without knowing, Van Leeuwenhoek was the first person to observe the microorganisms (or animalcules) conforming a dental-biofilm, or scurf as he called it [82]. Later, in 1940, once the golden age of microbiology had ended, it was recognized for the first time that surface-attached microorganisms exhibit different properties than they do as planktonic cells [79, 81]. However, the concept of biofilm-related infection and their importance in medicine was initiated in the early 1970 [82]. It was until 1985 that the term biofilm was introduced into medicine by J.W. Costerton [36]. At this time he demonstrated the increased antimicrobial resistance of biofilm growing bacteria compared to planktonic growing ones [36].

The biofilm definition coined by Costerton establish that a microbial biofilm is an aggregate of bacterial cells surrounded by a self-producing polymeric matrix [36]. Recent insights on biofilm development have shown that it is composed by aggregates of microorganisms,

separated by free spaces that are deprived from bacteria and are traveled by aqueous currents. This channels, which ensure the circulation of fluids, allow both the supply of nutrients to the embedded bacteria and the elimination of their degradation products [58, 166]. In fact, biofilms are not a homogeneous structure, they present complex architectures, which variations depend on the organisms that inhabit them and the environmental conditions [43]. Biofilms can be mono-species or poly-species, the latter are the most common in ecological environments and medical devices [46]. Moreover, biofilms may or may not adhere to surfaces [46, 143].

Biofilm formation is a multistage process that starts with microbial adhesion with a subsequent production and accumulation of an extracellular matrix composed by one or more polymeric substances as, proteins, polysaccharides, humic substances, extracellular DNA and sometimes molecules involve in cell-to-cell-communication [5].

Currently, there are well-established techniques to form and to evaluate biofilms, in table 1.1 some of them are summarized:

Table 1.1 Biofilm formation devices

Device	Technique	Biofilm type	Reference
Microtiter plates	S	SAB or ALIB	[136, 137, 162]
Caligary device	S	SAB	[24, 73, 127]
Ring test	S	SAB	[6, 27, 126]
Robbins device	F	FFB	[87, 91]
Drip-flow reactor	F	SAB	[63, 151]
Rotary reactor	F	SAB	[151, 154]
Flat plate reactor	F	SAB	[132]
Flow chamber	F	FFB	[163]
Microfluidic devices	S/F	SAB or FFB	[49, 144]

Note: S: static. **F:** flow. **SAB:**Surface-attached **FFB:**Free-floating
ALIB: air-liquid interface.

The application of the above devices, in combination with optical and genetics tools, has enabled the tremendous progress biofilm research has experienced in the past decades. Elucidating the genetic pathways, physiological responses or intracellular signal transduction pathways, such as those regulated by cyclic dimeric guanosine monophosphate (c-di-GMP), that underpin biofilm development and have contributed to the existent wealth of knowledge.

Nevertheless, our understating has only began to scratch the surface of the physical properties of mature biofilms or the complete understanding of the physics behind the developmental mechanisms of bacterial biofilms.

Recently, bacterial communities have caught the eye of physicist, in the rapidly growing field of active matter, and quantitative approaches to biofilm formation have been done. Active matter is composed of large numbers of active agents, each of which consumes energy in order to move or to exert mechanical forces. These "active systems" are intrinsically out of thermal equilibrium. Research on this field involve the study of synthetic systems or biological systems in a wide range of scales, including animal groups (macro scale), bacteria colonies, cellular tissues, among others. In particular, microorganism systems have served as model for observing the dynamic assembly and collective motility of self-propelled particles.

Motile bacteria are a clear example of an active agent, due to its self-propulsion. Bacteria exhibit diverse mechanisms of propulsion, but the one of our interest is the so-called run-and-tumble exhibited by *Escherichia coli (E.coli)*.

E.coli individual motion consists of periods of straight line swimming (runs), interrupted by brief bursts of rotational motion (tumble) that change the direction of the trajectory. This dynamic is diffusive at large scales, just like Brownian motion. However, when bacteria are in a collective, fascinating properties are displayed, which are originated by the interplay of individual self-propulsion and the interaction among individual in the group [174].

Typically, the emergent collective motion on bacteria is studied under confinement, as in recipient with finite walls, such as microchips, agar plates, and more recently, this phenomena has been studied under magnetic and optical confinement.

Collective behavior of bacteria in confined space

1. Agar substrates

Bacteria colonies are one of the simplest systems consisting of many interactive microorganisms, hence, a number of studies have focused on the experimental and theoretical aspects of its formation and on the related collective behavior [174]. On the 70's *E.coli* bands were experimentally studied and also modeled [90]. Since then it became evident than the bacteria within the colonies growing on wet agar surfaces produces a variety of collective motion

patterns, see Figure 1.1.

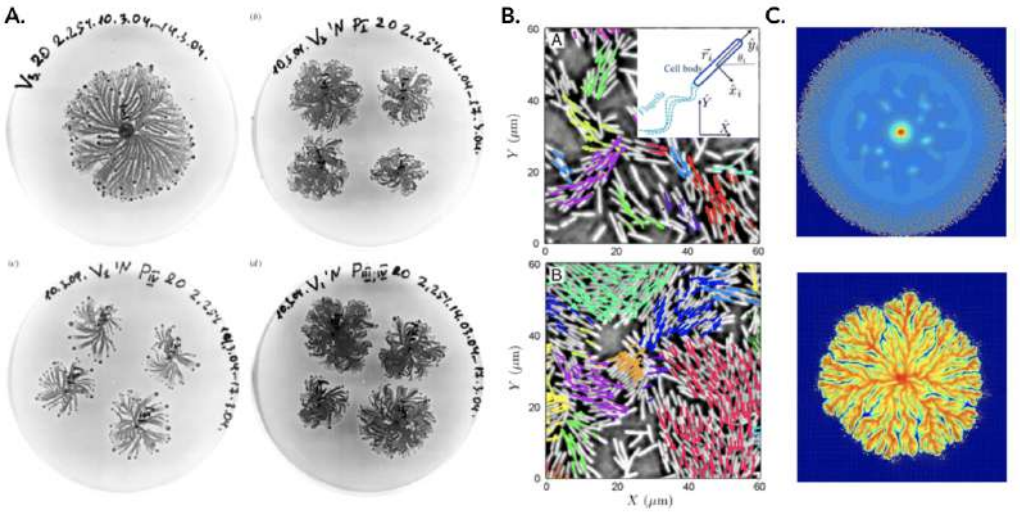

Fig. 1.1 **Collective motion on agar surfaces. A.** Vortices exhibit by*Paenibacillus vortex*. Each plate is inoculated with bacteria that grew on different zones of the mother plate [84].**B.** Instantaneous configurations at two densities of *Bacillus subtilis*.The velocity vectors are over-layered on the raw images of bacteria. **C.** Two dimensional velocity fields superimposed on color plots of n-vectors, with zero magnitude vectors are represented by a dot, which describes bacterial dynamics both within and near the boundary of the colony [105].

2. Thin films

One method for observing active bacterial systems is to disperse a certain concentration of bacterial suspension in a free-standing soap with micro-metric thickness and use micron-sized particles to track the flow [101]. Under this configuration it has been observed that the majority of the bacterial suspension fluid self-organize into an active bacterial film [123].

3. Lab-on-a-chip

There is a myriad of experimental experiments that track the orientation of cells in a confined and dense bacterial suspension. This ranges from the analysis of suspensions of aerobic bacteria confined in a microchannel than exhibit bioconvective plumes, and on scales much larger than a cell,the presence of high-speed jets straddled by vortex streets produced by the hydrodynamic interactions between swimming cells [112].

Other experiments have enable the direct measurements of the bacterial flow field generated by individual swimming Escherichia coli both far from and near to a solid surface. Also, the quantification of cell–cell interactions and its link with the assemblages of biofilaments, and flocks [47].

The emergence of self-sustained meso-scale turbulence dominated by short-range interactions [179] and the existence of a transition from quasi-two-dimensional collective swimming to three-dimensional turbulent behavior [3, 157, 186, 185].

Additionally the presence of he “Zooming BioNematic” (ZBN) in nearly close-packed populations of the swimming bacterium *Bacillus subtilis* that is analogous to the molecular alignment of nematic liquid crystals[29].

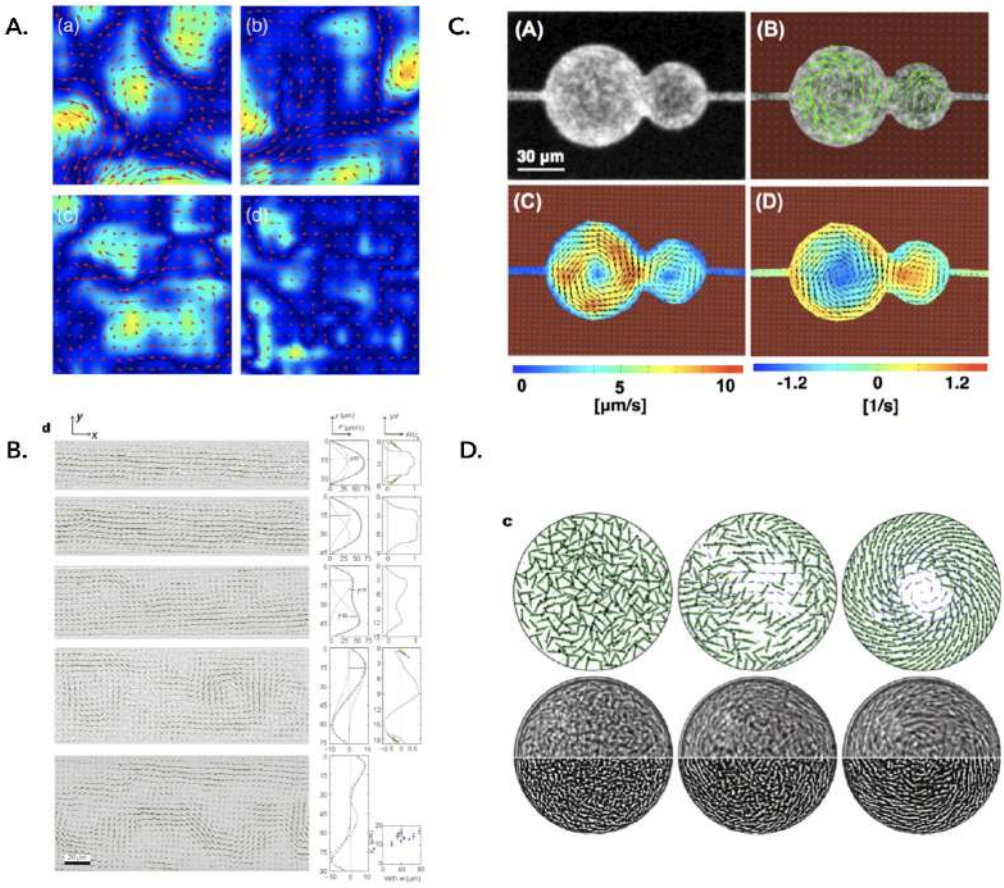

Fig. 1.2 **Collective motion on agar surfaces. A.** Vortices exhibit by *Paenibacillus vortex*. Each plate is inoculated with bacteria that grew on different zones of the mother plate [84].**B.** Instantaneous configurations at two densities of *Bacillus subtilis*.The velocity vectors are overlayered on the raw imagesof bacteria. **C.** Two dimensional velocity fields superimposed on color plots of n-vectors, with wero magnitud vector are represented by a dot, which describes bacterial dynamics both within and near the boundary of the colony [105].

4. Magnetic traps

Experiments with magnetotatic bacteria have provided information of the rheology as a function of the magnetic field applied. It has been shown that in the limit of low shear rate, the rheology exhibits a constant shear stress, called actuated stress, which depends on the swimming activity of the particles and its induced by the magnetic field. It can be positive (brake state) or negative (motor state) [176]. Some other experiments showed that these magnetic responsive bacteria produce magnetic crystals that align the cells with an external magnetic field. Also, at dense suspension the increased interaction between magnetotactic bacteria alters the ability of any individual cell to align with an applied magnetic field [16].

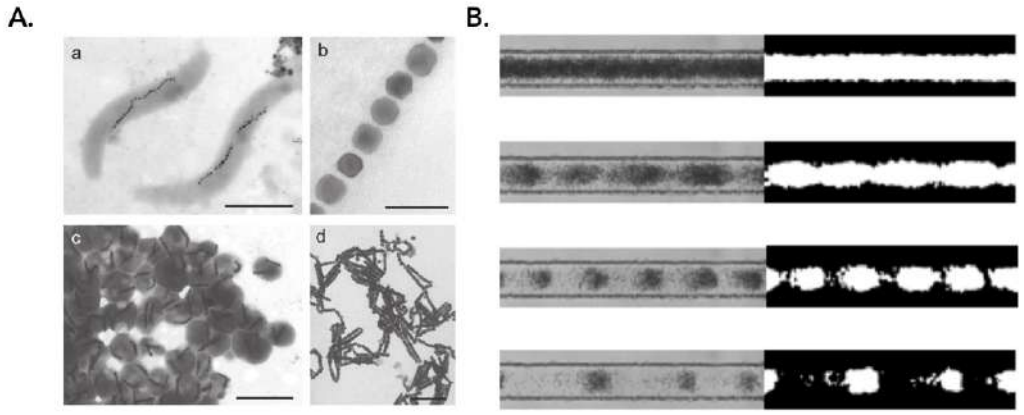

Fig. 1.3 **Collective motion on agar surfaces. A.** Vortices exhibit by*Paenibacillus vortex*. Each plate is inoculated with bacteria that grew on different zones of the mother plate [84].**B.** Instantaneous configurations at two densities of *Bacillus subtilis*.The velocity vectors are overlayered on the raw imagesof bacteria. **C.** Two dimensional velocity fields superimposed on color plots of n-vectors, with wero magnitud vector are represented by a dot, which describes bacterial dynamics both within and near the boundary of the colony [105].

The aforementioned mechanisms of confinement provide great insight in the emergence of collective motion and "bio-turbulence" of bacterial suspensions. In most cases, no matter the type of confinement, when a dense suspension of cells is used, the presence of instantaneous phase separation is often encountered; as well as the presence of wall-attached microorganisms that lead to the formation of dense clusters [3, 157, 186, 185]. In microbiological literature, these dense clusters are known as aggregates, and are frequently provoked by a down-regulation of the swimming activity of the cells, i.e. a decrease in their self-propulsion activity. This intrinsic mechanism of bacteria is of great importance in biofilm formation, where bacteria not only decreases their swimming velocity but also lose their flagella after a

period of time [22].

From this, we can conclude that most of these confinement techniques are suitable to study biofilm development, at least the initial stages, as the density dependent swim speed could be characterized and also the emergence of the phase-separation over time.
Nevertheless, these techniques have some technical shortcomings. In microchips, the formation of the dense cluster could be performed fast (in hours) only if the suspensions are super-dense, such that the imaging of the wall-attached cells could be difficult. On the other hand, agar plates can be easily scanned but a tedious and time taking protocol has to be done, as the plates should be inoculated and should incubate over-night to obtain a mature colony or aggregate [123].

Magnetic confinement only could be used if the bacteria cells are responsive to magnetic fields thus limiting the model microorganisms that could be used. In addition, unfortunately, the microorganisms that are of interest in the study of biofilm-associated diseases cannot be handled with magnetic fields.

A technique that could provide confinement and has proven to be robust enough to overcome this challenges is acoustic trapping. Acoustic trapping is the immobilization of particles and cells in the node (or antinode) of an ultrasonic standing wave field. It is a gentle way of performing non-contact immobilization of cells and particles.

Acoustic trapping works by creating ultrasonic standing waves in microfluidic channels, cavities, or other small, confined spaces creating pressure nodes that attract and hold particles and cells [71]. Commonly, structures in the range of a couple of 100 μm are used, corresponding to acoustic frequencies in the MHz-range. The manipulation of the cells relies on its acoustic properties such as density or compressibility, providing a robust technique that could manipulate basically any particle or cell [169, 21].

Moreover, several studies have shown that ultrasonic levitation does not seem to have any negative effects on live cells. Hultström et al. cultured cells that had been levitated for over an hour and studied the doubling times of the cells [165]. No direct or delayed damage could be detected on the cells. Also, Bazou et al. performed a study on mouse embryonic stem cells and confirmed that they could see no changes in gene expression after ultrasonic treatments up to one hour, and the cells maintained their pluripotency [9].

Taking the above mention into account, it appears that the technique could improve the confinement of cells, as it provides a control confinement that does not damage cells. On top of that, the trapping at the nodes of standing waves provides the possibility to confine cells without surface interactions. For this reasons the aim of this work is to implement this technique to confine *Escherichia coli* cell at the nodal plane to study the impact of confinement on biofilm formation. Accordingly, this work is structured in the following themes: 1) the study of collective motion of bacteria and 2) the study of bacteria social behaviour related to biofilm development — both under acoustic confinement.

Chapter 2

Acoustic confinement in levitation

Acoustic waves can exert forces on small particles, a fact that was discovered by August Kundt and presented as a way to measure the speed of sound in gaseous medium [99]. More than one hundred years later, in 1971, this effect was observed for biological particles in a liquid media. Dyson et al. [52] and later Baker et al. [7] reported red blood cells bands that appeared after their exposure to ultrasound. Today, this phenomenon is utilized primarily for air-levitators, where small droplets or particles can be held in air without contact[107], separation of bioparticles in a flow via acoustophoresis, as well as the capture and retention of cells or microparticles in fluids through acoustic trapping.
Acoustic trapping is based on the use of mechanical waves to manipulate particles, the parameters that allow their manipulation are density and compressibility -from the particles and the fluid. It is clear that the long wavelength, in the millimeter rage, is an advantage as it allows capturing large groups of particles and also provides the capture and retention of particles without surface contact.[21]

At this moment, there are several micro-systems used for acoustic trapping with a plethora of biological and non-biological applications. Nevertheless, the fact that these systems are complex and functional labs-on-a-chip does not imply that they are the only or most robust acoustic trapping systems. Therein, an emblematic acoustic trapping system is the multilayered or planar-resonator. The resonator is a vertical structure with three wavelength-matched layers, i.e. the layers should have an acoustic impedance and thickness that depends on the used wavelength[56] (see Figure), each of which, are typically stacked on a piezoceramic transducer: a coupling layer for efficient transmission into the structure, a fluid layer where the capture takes place, and a reflecting layer for retaining the acoustic energy in the device. By using operational frequencies on the order of MHz and single or multiple nodes, the fluid layer can be scaled down sufficiently to allow laminar flow conditions inside the cavity of a

macro-system, as in the design pioneered by Bazou et al[9].

One of the key goals of this thesis is to design and develop a trapping system based on acoustic resonances. In this Chapter, an introduction to the theory behind these systems is presented, followed by the specifics of the design, fabrication and characterization.

2.1 Acoustofluidics

Acoustofluidics is the linkage of ultrasonic waves with microfluidic systems to manipulate fluids and particles in the microscale. In the 1930s a key study of incompressible particles in acoustic fields was published[94] and twenty years later, the forces on compressible particles in plane acoustic waves were calculated by Yosioka and Kawasima[190]. Later, these works were admirably summarized and generalized in a short paper by Gorkov[65].
At the beginning of the 1980s, a lot of work had appeared discussing the usability of acoustic waves to trap and transport passive systems. Unfortunately, as so often happens in science, the idea was left behind to experience a revival in the early 2000s, with what is known as *acoustofluidics*. After the new term was coined[21], seminal works from Coakley[75, 30, 74, 31], Laurell [122, 106] and Bruus[19, 8] appeared, providing a detailed mathematical and experimental verification of how ultrasonic waves are applicable in microfluidics.

The main idea is that the wavelength (λ) generated by the coupling of the ultrasonic frequencies (f), in the low MHz-range, and the speed of sound in water c is typically less than 1 mm. For that reason, it may fit submillimetric cavities and result in the formation of resonance modes. Accordingly, it has been proved that it is advantageous to operate an acoustofluidic device in its acoustic resonances[69], as they are stable, reproducible, and the spatial patterns are controlled by the geometry of the device. Moreover, the maximum acoustic power released by the piezoceramic transducer to the system arises in resonant systems, where it results in the apparition of acoustic radiation forces and acoustic streaming[69, 106].

2.1.1 Acoustic waves

Acoustic waves are mechanical and longitudinal waves, i.e. same direction of vibration as the direction of propagation, that result from an oscillation of pressure that travels through a solid, liquid or gas in a wave pattern. They can be characterized by their wavelength $\lambda = v/f$ that

depends on the media in which the wave is propagating, their frequency f, period $T = 1/f$ and amplitude.
The acoustic wave is defined using a field that describes either the displacement itself ξ, the velocity of the displacement $\mathbf{v}$, the scalar velocity potential Φ such that $\vec{v} = \vec{\nabla}\Phi$, or the pressure changes $\mathbf{p}$ associated with displacing the matter. Regardless of which aspect is used to describe the acoustic wave, it will obey the wave equation, that for velocity is:

$$\frac{\partial^2 \mathbf{v}}{\partial^2 t} = c_0^2 \nabla \mathbf{v} \tag{2.1}$$

Here, c is the speed of sound as it couples the change in position to the change in time. The speed of sound is a material-dependent parameter and can be found from the compressibility κ and the density ρ of the media using the following relation:

$$c_0 = \frac{1}{\sqrt{\kappa \rho}} \tag{2.2}$$

2.1.2 Acoustic waves interaction with suspensions

The linear wave equation for the acoustic field in a fluid can be derived using a first order perturbation theory. We recall here the derivation of Bruus[20] where the acoustic field is derived based on an equation of state describing pressure p in terms of density ρ (equation 2.3), the kinematic continuity equation for the density (equation 2.4), and the dynamic Navier-Stokes equation for the velocity $\mathbf{v}$ (equation 2.5):

$$p = p(\rho), \tag{2.3}$$

$$\partial_t \rho = -\nabla \cdot (\rho \mathbf{v}), \tag{2.4}$$

$$\rho \partial_t \mathbf{v} = -\nabla p - \rho (\mathbf{v} \cdot \nabla)\mathbf{v} + \eta \nabla^2 \mathbf{v} + \beta \eta \nabla (\nabla \cdot \mathbf{v}). \tag{2.5}$$

In the first order perturbation theory, a quiescent liquid with constant density ρ_0 and pressure p_0 is considered. At a given time, the fluid is disturbed by an acoustic wavefront and the small perturbations in the density, velocity and pressure fields are described respectively by:

$$\rho = \rho_0 + \rho_1, \quad p = p_0 + c_0^2 \rho_1 \quad \text{and} \quad \mathbf{v} = v_1. \tag{2.6}$$

Later, when the equation of state is derived, it has the dimension of a squared velocity c_0^2 where c_0 is considered as the speed of sound in the fluid. Using the previous equations, and neglecting products of first-order terms, the first-order continuity and Navier-Stokes equations are:

$$\partial_t \rho_1 = -\rho_0 \nabla \cdot v_1, \tag{2.7}$$

$$\rho_0 \partial_t v_1 = -c_0^2 \nabla \rho_1 + \eta \nabla^2 v_1 + \beta \eta \nabla (\nabla \cdot v_1) \tag{2.8}$$

Following Bruus[20] we assume that there is a harmonic dependence in all fields, such that:

$$\rho_1(r,t) = \rho_1(r) e^{-i\omega t}, \quad p_1(r,t) = c_0^2 \rho_1(r) e^{-i\omega t} \quad \text{and} \quad v_1(r,t) = v_1(r) e^{-i\omega t}, \tag{2.9}$$

with $\omega = 2\pi f$ as the angular frequency and, as stated before, f the frequency of the acoustic field. Inserting equation 2.9 into equation 2.7-2.8 the equation of pressure is:

$$\nabla^2 p_1 = -k^2 p_1, \tag{2.10}$$

with k the complex the wave-number

$$k = (1 + i\gamma) k_0 = (1 + i\gamma) \frac{\omega}{c_0}. \tag{2.11}$$

In this manner, equation 2.10 is the Helmholtz equation for a damped wave with wave-number k and angular frequency ω. Since the damping factor $\gamma \ll 1$ the viscosity on the bulk part of the acoustic wave is neglected, hence, the wave equation is:

$$\nabla^2 p_1 = \frac{1}{c_0^2} \partial_t^2 p_1. \tag{2.12}$$

This equation shows that a pressure perturbation propagates a distance $\pm c_0 t$ in time t, therefore c_0 is indeed the speed of sound.

To assess the slowly evolving phenomena that arise due to acoustic waves it is necessary to use the second-order perturbation theory. On this theory, the processes are governed by time-averaged fields, where the temporal averages of the first order fields are zero and an expansion in equations is needed.

$$\rho_0 \nabla \cdot \langle v_2 \rangle = -\nabla \cdot \langle \rho_1 v_1 \rangle, \tag{2.13}$$

$$\eta\nabla^2\langle v_2\rangle + \beta\eta\nabla(\nabla\cdot\langle v_2\rangle) - \nabla\langle p_2\rangle = \langle\rho_1\partial_t v_1\rangle + \rho_0\langle(v_1\cdot\nabla)v_1\rangle. \tag{2.14}$$

The time-averaged second-order fields will, in general, be non-zero because of the time-averaged products of first-order terms acting as source terms on the right-side of the governing equations. It is important to emphasize that, physically, the non-zero velocity $\langle v_2\rangle$ is the so-called acoustic streaming and that from the non-zero pressure $\langle p_2\rangle$ arises the acoustic radiation force coming from the scattering of acoustic waves on the particles causing acoustophoretic motion of the particles[20].

2.1.3 Resonance modes

In a geometry confined by boundary conditions, the wave equation has Eigen-modes, corresponding to the pattern in the acoustic field that repeats over time, and Eigen-values, that are associated with the repetition frequency. If the system is supplied with a matched frequency, to the repeating patterns in the acoustic field, more energy can be added to the system –thereby creating a resonating system.

In other words, acoustic resonances occur for certain specific frequencies ω_j, j=1,2,3,(...) An acoustic resonance at given ω_j is a state where the average acoustic energy density ($< E_{ac} >$) inside the cavity is several orders of magnitude larger than at other frequencies. By tuning the applied frequency to one of these resonance frequencies, the acoustic forces become strong enough to enable particle manipulation. The values of the frequencies depend on the geometry of the acoustic cavity and on the material and liquid parameters. The most relevant parameters are the speed of sound in the media c, the density of the media ρ_0 and, in the same manner, of the material composing the cavity.
The amplitude of a resonance field, at a given actuation, is determined by the amount of energy that can be stored in the mode and transferred to the system. This is determined by the attenuation of the system and the coupling of the source of actuation.

In idealized systems, i.e. simulation, it is feasible to calculate possible modes for a given geometry and the usage of experimental data make predictions more accurate. Also, there are *in silico* techniques to measure the acoustic field or experimental, such as the use of hydrophones, but on closed systems not suitable method has yet been invented to measure these properties directly. However, the acoustic field can be measured indirectly using the movement of particles coupling particle tracking velocimetry in combination with mathematical models as in Figure 2.1.

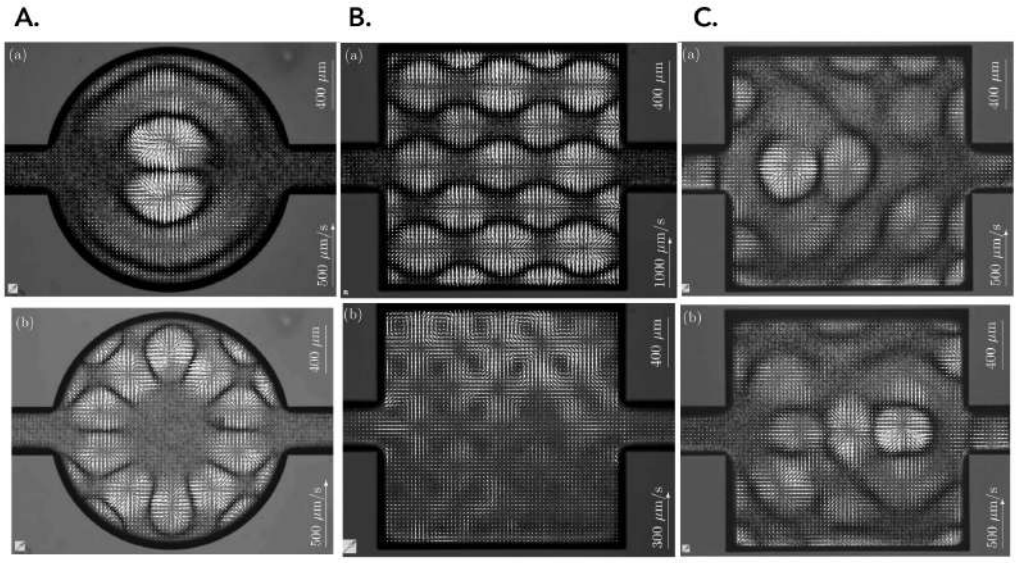

Fig. 2.1 **Acoustic resonances in microfluidic chips.** Three sets of experiments performed by Hagsater *et al.*[**?**] (A.) Experiments with $5\mu m$ beads at 1.936MHz acoustic resonance. The white vectors indicate the initial bead velocities pointing away from pressure anti-nodes immediately after the piezo-actuation is applied. On the bottom, the distribution of the beads on a different acoustic resonance is depicted. (B.) The acoustic and radiation forces at a 2.7 MHZ resonance show that with 5 μm particles (top) acoustic streaming can be neglected, whereas for $1\mu m$ (bottom) it overcomes acoustic forces and the particles act as tracers of the flow. (C.) Experiments with 5 μm beads show that the geometry asymmetries on the micro-devices can change completely the energy distribution for different acoustic resonances.

2.1.4 Acoustic radiation force on small particles

A spherical micron-sized particle with radius $a \ll \lambda$, density ρ_p and compressibility κ_p suspended in an inviscid fluid with density ρ_0 and compressibility κ_0 under the influence of an ultrasonic field of wavelength λ, will act as a weak point-scatterer of acoustic waves. The incoming wave described by a velocity potential ϕ_{in} will result in a scattered wave ϕ_{sc} propagating away from the particle as depicted in 2.2. As a result, the total first order acoustic field ϕ_1 is the sum of the two and it is valid for weak incoming and scattered waves.

Then, we have mathematically:

$$\phi_1 = \phi_{in} + \phi_{sc}, \tag{2.15}$$

$$v_1 = \nabla\phi_1 = \nabla\phi_{in} + \nabla\phi_{sc}, \tag{2.16}$$

$$p_1 = i\rho_0\omega\phi_1 = i\rho_0\omega\phi_{in} + i\rho_0\omega\phi_{sc}. \tag{2.17}$$

Once the first-order scattered field is calculated, by a given incoming field, the acoustic radiation force F^{rad} on the particle is calculated as the surface integral of the time-averaged second-order pressure p_2 and a momentum flux tensor $\rho\langle v_1 v_1\rangle$ at a fixed surface outside the oscillating sphere, represented by the yellow arrows in Figure 2.2.
The expression for the radiation force becomes[20]:

$$F^{rad} = -\int_{\delta\Omega} da\,\{\langle p_2\rangle\mathbf{n} + \rho_0\langle(\mathbf{n}\cdot v_1)v_1\rangle\} \tag{2.18}$$

$$= -\int_{\delta\Omega} da\left\{\left[\frac{1}{2}\kappa_0\langle p_1^2\rangle - \frac{1}{2}\rho_0\langle v_1^2\rangle\right]\mathbf{n} + \rho_0\langle(\mathbf{n}\cdot v_1)\,v_1\rangle\right\}, \tag{2.19}$$

where $\mathbf{n}$ is a unit vector pointing outwards perpendicular to the element of an area da. In this problem there are no body forces, thus, any fixed surface $\partial\Omega$ encompassing the spherical particle experiences the same force. To derive the rest of the equations, scattering theory is used; for a detailed description of this,see [**?**]. The scattered field ϕ_{sc} from a point scatterer at the centre of the system is represented by a time-retarded multi-pole expansion. In the far field region, the monopole (ϕ_{mp}) and dipole (ϕ_{dp}) components dominate and according to the first-order scattering theory ϕ_{sc} must be proportional to the incoming field ϕ_{in}.
The implementation of the scattering theory allows the radiation force to be expressed in terms of the incoming acoustic wave evaluated at the particle position and can be used to derive two complex scattering coefficients f_1 and f_2 that represent,respectively, a monopolar

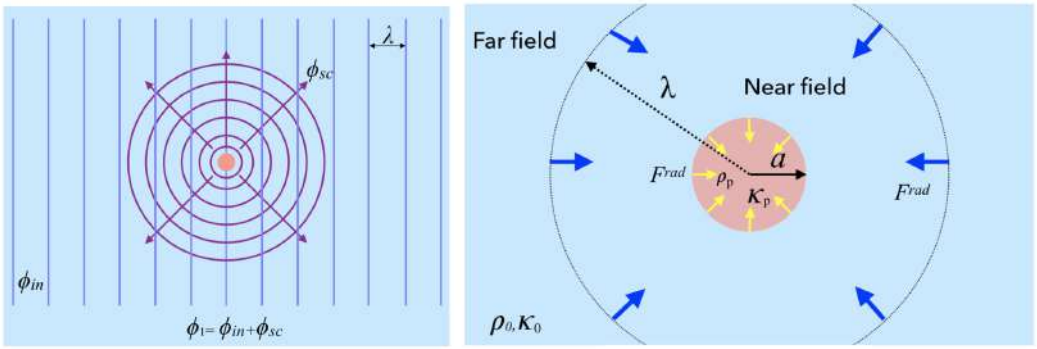

Fig. 2.2 **Acoustic radiation force.** On the left, a sketch of the far-field region $r \ll \lambda$ of an incoming acoustic wave ϕ_{in} (vertical purple line) of wavelength λ scattering off a small particle (pink dot) with radius $a \ll \lambda$, prompting the outgoing scattered wave ϕ_{sc} (red circles and arrows). The resulting first-order wave is $\phi_1 = \phi_{in} + \phi_{sc}$. On the right it is shown a compressible spherical particle (pink) of radius a, compressibility κ_p, and density ρ_p, surrounded by the compressible invscid bulk fluid of compressibility κ_0 and density ρ_0. The fluid is divided into the near-field region for $r \ll \lambda$, with the instantaneous field $\phi_{sc}(t)$, and the far-field region with the time-retarded field $\phi_{sc}(t - \frac{r}{c_0})$. The radiation force, F^{rad} (blue arrows), evaluated at any surface in the far-field region (dashed circle), equals that evaluated at the surface of the sphere (yellow arrows). [20]

scattering due to the presence of a compressible particle, and a dipolar scattering related to the translation of the particle. f_2 depends thus on the viscosity of the fluid. Therefore, the equation for the radiation force acting on a small particle ($a \gg \lambda$) is:

$$F^{rad} = -\frac{4\pi}{3} a^3 \nabla \left[\frac{1}{2} \mathrm{Re}[f_1] \kappa_0 \left\langle p_{in}^2 \right\rangle - \frac{3}{4} \mathrm{Re}[f_2] \rho_0 \left\langle v_{in}^2 \right\rangle \right], \tag{2.20}$$

with:

$$f_1(\tilde{\kappa}) = 1 - \frac{\kappa_p}{\kappa_0} \tag{2.21}$$

$$f_2(\tilde{\rho}) = \frac{2(\rho - 1)}{\rho + 1}. \tag{2.22}$$

In summary, the resulting radiation force F^{rad} on a small, spherical particle in an inviscid fluid is the gradient of an acoustic potential:

$$F^{rad} = -\nabla U^{rad}. \tag{2.23}$$

In the case of a 1D planar standing $\lambda/2$-wave with, $p_1(z) = p_a \cos(kz)$ where $k = 2\pi/\lambda = \omega/c_0$ and $w = \lambda/2$ being w the channel width, the radiation force from such field is given by:

$$F_z^{rad} = 4\pi\Phi(\kappa,\rho)ka^3E_{ac}\sin(2kz), \tag{2.24}$$

where the acoustic energy density is:

$$E_{ac} = \frac{P_a^2}{4\rho_0 c_0^2} \tag{2.25}$$

and the so-called acoustophoretic contrast factor

$$\Phi(\tilde{\kappa},\tilde{\rho}) = \frac{1}{3}\left[\frac{5\tilde{\rho}-2}{2\tilde{\rho}+1} - \tilde{\kappa}\right] \tag{2.26}$$

2.1.5 Energy density in a piezo-transducer application

A linear relation exists between the applied peak-to-peak voltage U_{pp} of the piezo-transducer that produces the ultrasonic resonances and induce acoustic pressure amplitude p_a:

$$E_{ac} \propto p_a^2 \propto U_{pp}^2 \tag{2.27}$$

By tracking the y-position over time of polystyrene micro-beads Barnkob *et al.*[8] showed that at a fixed driving frequency ($f = 1.99MHz$) the acoustic energy density (E_{ac}) as a function of the peak-to-peak value U_{pp} (0.5-1.9 V) scales as a power law of the form $E_{ac} \propto (U_{pp}^{2.07})$ as depicted in Figure 2.3. This is close to the power law of 2, which is expected since the acoustic pressure delivered by the piezo-transducer is proportional to the applied voltage and, the acoustic energy density proportional to the square of the pressure see equations (1.29 and 1.31)[**?** 69].

2.1.6 Secondary radiation force

The secondary radiation force –also known as Bjerkness force when acting between gas bubbles or Köning forces between solid particles–is an inter-particle force[44]. It can be attractive or repulsive and depends on the distance between particles. In addition, its amplitude is two orders of magnitude smaller than the primary radiation force (F^{rad}). Here each particle acts as a scattering point, hence, the acoustic waves coming from the emitter will scatter in each one of them.

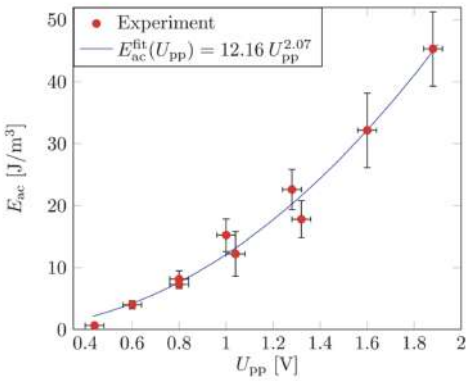

Fig. 2.3 Measured acoustic energy density E_{ac} versus applied peak-to-peak voltage U_{pp} on the piezo -transducer (points) for $\alpha = 1$. A power law fit (full line) to the data is close to the expected square law, $E_{ac} \propto U_{pp}^2$. From this figure, Barnkob *et al.*[8] were able to extract reliable values for E_{ac} which in this case was found to be 6.69 J/m^3

The secondary force in the case of a plane wave incident field in a suspension is given by[153]:

$$F_{sec} = 4\pi a^6 \left[\frac{(\rho_p - \rho)^2 (3\cos^2\theta - 1)}{6\rho d^4} v^2(x) - \frac{\omega^2 \rho (\kappa_p - \kappa)^2}{9d^2} p^2(x) \right]. \tag{2.28}$$

Here ω is the angular frequency,d is the distance between particles (centre-centre) and θ is the angle between the axis of the incident wave and the centre-line connecting the two particles.

The definition of the force is such that a negative sign should be interpreted as an attractive force between the particles. The secondary radiation force scales heavily with the distance between the particles as the magnitude drops off so rapidly with particle spacing, the effects of the secondary radiation force can be ignored in many cases. Nevertheless, when particles are trapped in a tight cluster it implies that the force has a significant contribution.

Interestingly, the secondary radiation force has two terms; one that is always attractive, and one that is angle-dependent. As the angle-dependent term diminishes faster with the distance between the particles there will be an equilibrium-distance to which a particle is drawn. The equilibrium distance will be angle dependent, such that at some angles the particles will tend to be as close as possible, whereas at other angles a small separation will be preferential. While the formula for the force is given for two identical particles, in reality, there will, of course, be secondary forces between particles with different sizes and properties.

2.1.7 Acoustic streaming

The acoustic field imposed on a suspension will not only create forces on the particles, it will also create forces on the media itself. This phenomenon is called acoustic streaming, and it is defined as the generation of fluid flows by sound. Here, the sound plays the leading role and the flow is a by-product. Furthermore, acoustic flow generation shows features symmetrical with those of aerodynamic sound generation, *i.e.* not only can a jet generate sound, but also sound can generate a jet[108].

The first theoretical model to thoroughly describe acoustic streaming flows was derived by Rayleigh in 1884[142]. In his work, Rayleigh treats the cases of streaming that were observed experimentally by Faraday[55] and Dvorak[17]. The first two cases, observed by Faraday, are related to the observations on the patterns assumed by sand and fine powders on Chladni's vibrating plates[28] and the third, observed by Dvorak, on the circulation of air currents in a Kundt's tube[142, 55].

Streaming flows vary greatly depending on the mechanism behind the attenuation of the acoustic wave. The variations include the velocity of the flow, the length scale of the flow and the geometry of the same. The velocity varies from being on the order of mm as in the case of slow streaming, up to velocities on the order of cm or more in the case of fast streaming. The length scale varies from being on the order of mm in the case of microstreaming up to the order of cm in bulk-streaming.[182]The flow geometry may take the form of a jet or of vortices. Boundary-layer driven acoustic streaming is formed by the viscous dissipation of acoustic energy into the boundary layer of a fluid along any solid boundary that is comparable or greater in length (in the direction of acoustic propagation) than a quarter of the acoustic wavelength.[124] Furthermore, the streaming flow is typically observed in fluid cavities where at least one dimension perpendicular to the direction of acoustic propagation is comparable in size to the acoustic wavelength.

The main types of streaming flows that have been described in the literature can be classified as:

i. Schlichting streaming. Described as the viscous dissipation that results in steady momentum flux that arises in a system, which has a standing wave parallel to the surface typically oriented from the pressure anti-nodes to the pressure nodes close to the solid boundary, see Figure 2.4A.[149]

ii. Rayleigh streaming This type of streaming,depicted in 2.4A, appears once Schlichting streaming is established. The powerful inner boundary layer streaming flow generates counter rotating streaming vortices within the bulk of the fluid.[142]

iii. Eckart streaming. Formerly called "quartz wind" is the flow formed by the dissipation of acoustic energy into the bulk of a fluid, as seen in figure 2.4B. As an acoustic wave propagates through a fluid, a part of the acoustic energy is absorbed by the fluid at a rate proportional to the square of its frequency. The amplitude of the acoustic wave becomes attenuated causing the acoustic pressure amplitude to decrease with distance from the acoustic source. The loss of acoustic energy results in a steady momentum flux, forming a jet of fluid inside the acoustic beam in the direction of the acoustic propagation. When a fluid jet is formed within the confinement of a microchamber vorticity ensue, resulting in a fluid circulation either part of or within the entire chamber[182]. Matsuda, Kamakura and Maezawa showed that the Eckart streaming will only take place in microfluidic devices when high-frequency ultrasound is propagated along a dimension on the order of a millimetre long.[191]

iv. Cavitation microstreaming. This particular form of boundary-layer-induced streaming arises by the viscous dissipation of acoustic energy in the boundary layer of a stable oscillating microbubble[109]. The forced oscillation of microbubbles, sonicated at or near their resonance frequencies, results in the local amplification of the first order velocity[124]. It is an altogether different concept from that of a fluid jet formed by the destructive cavitation of a bubble, which despite being an acoustically induced flow is not a form of acoustic streaming, see Figure 2.4C.[124, 182]

As we can see acoustic streaming is a well-known phenomenon, nevertheless, due to its many forms, it is often considered a nuisance since it is present inside many acoustically driven microfluidic devices where it could be counterproductive. While in some cases it is indeed a problematic phenomenon[192, 135, 178], when used correctly it can be very useful and could help in overcoming some of the challenges presented by low Reynolds number flows in microfluidics[182, 125].

Rayleigh streaming plays an important role on half-wavelength chambers setting a principle lower limit on the particle size that can be manipulated by the primary radiation force in a standing wave. This is particularly relevant when the streaming direction is opposite to the direction of the radiation force. For example, Spengler *et al.*[159] observed that whilst

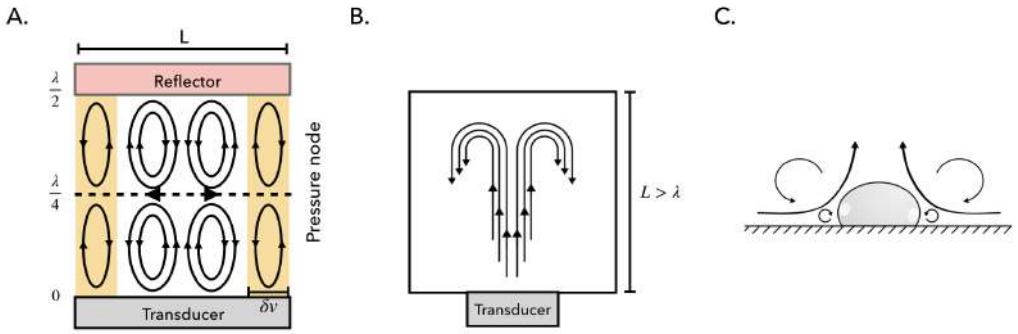

Fig. 2.4 A. A $\frac{\lambda}{2}$ resonator with inner Schlichting boundary layer streaming within the viscous boundary layer (yellow regions) with thickness δv and outer (Rayleigh) boundary layer streaming within the bulk of the fluid (white region). In the plane of the pressure node, the outer boundary layer streaming is directed outwards counteracting the lateral component of F^{rad} B. Eckart streaming in a resonator much larger than the wavelength ($L > \lambda$). The forward streaming jet induces backflow typical for Eckart streaming[125].C.Cavitation microstreaming due to spherical volume oscillations of a gas bubble resting on a solid boundary. Here the cross-section through the center of the bubble is shown. Due to the hemi-spherical shape of the bubble only half of the typical streaming pattern is formed[53].

larger (10 μm) particles became agglomerated in the centre of the pressure nodal plane, smaller particles of the order of one micrometre did not because the drag from the streaming flow overcame the lateral radiation force. Later, it was shown that beads of intermediate size are able to overcome the drag from Rayleigh streaming only after they have formed mini-aggregates off-axis at the edges of the acoustic fields, implying that the depletion of beads in that plane is caused by the increase of the effective volume of the mini-aggregates relative to single beads. Therefore, the increase in volume has a stronger effect on the volume-dependent radiation force than on the radius-dependent viscous drag from acoustic streaming[160, 159, 100].

In addition, Martin and Minor found that increasing either the frequency or pressure amplitude resulted in an increase of the streaming velocity, whereas halving the chamber thickness (to obtain a $\frac{1}{4}\lambda$ resonance) had as a consequence a reduced streaming velocity[59]. Posterior to this, a more detailed analysis of the size-dependent cross-over from radiation force dominance to streaming dominance was carried out by Barnkob *et al.*[8] see figure 2.5 and they concluded that the theoretical threshold,based on experimental data, defined as the particle size for which the two forces were equal in magnitude, corresponding to a particle with diameter of 2.6 μm at a driving frequency of 2 MHz, and that the threshold particle

size is proportional to $\frac{1}{\sqrt{f}}$, where f is the driving frequency[4]. As discussed before Eckart streaming is not the dominant form of acoustic streaming observed in microfluidic devices, however, if the dimensions of the channel or chamber parallel to the propagation direction of the acoustic wave are of scale $>$ 1 mm it may occur. When it comes to cavitation micro-streaming, typical applications are the generation of whole scale flows and the generation of highly targeted flows used in micromixing and cell membrane sonoporation.

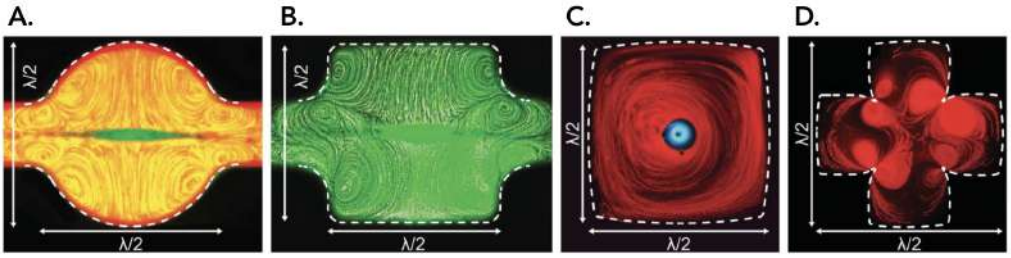

Fig. 2.5 Acoustic streaming patterns in different geometries of the acoustic resonant cavity, visualized by making an overlay of a series of frames from a video clip. The width is between 300 and 350 μm in all cavities, and the driving frequency is between 2.1 and 2.6 MHz. The streaming is tracked by 1 μm fluorescent beads and the trapped cluster in the centre of each cavity contains 5 μm beads in (a) and (b), and 10 μm cells in (c). There are only 1 mm beads present in (d). These experiments correspond to Rayleigh streaming [182, 183]

2.2 Acoustic confinement

To confine living or non-living matter in microgravity like conditions, acoustic trapping systems work under the basis of the acoustic radiation forces that arise when a standing wave is set up in a microchannel or in the cavity where a suspension is placed. To create a standing wave inside a cavity or micro-channel, the driving frequency must meet a resonance criterion as follows:

$$w = n\frac{c_0}{2f} = n\frac{\lambda}{2}. \tag{2.29}$$

Where w is the width of the channel or cavity, n is the number of pressure nodes in the standing wave, c_0 is the speed of sound in the fluid, f is the acoustic frequency and λ the wavelength of the acoustic input. The acoustic radiation forces will promote the displacement of objects either to the point of maximum or minimal acoustic potential in the standing wave (figure 2.6 depending on the acoustic properties of the species being handled. On a 1D

planar standing wave, the acoustic radiation force, as expressed in Equation 2.22, shows that the radiation force can be expressed as the gradient of the acoustic potential U^{rad} is given by:

$$U^{rad} = \frac{4\pi}{3}a^3\left[f_1\frac{1}{2}\kappa_0\langle P_{in}^2\rangle - f_2\frac{3}{4}\rho_0\langle v_{in}^2\rangle\right], \tag{2.30}$$

where $\langle P_{in}^2\rangle$ and $\langle v_{in}^2\rangle$ are the time averages of the incoming pressure and velocity fields squared, and the scattering coefficient f_1 and f_2 relate compressibility and density, of the particles and the medium, respectively. These characteristics determine the position of the entities to be handled in the potential. Most cells and microparticles with density and compressibility lower than the surrounding medium will move to the point of minimal acoustic potential i.e. the pressure node of the standing wave.

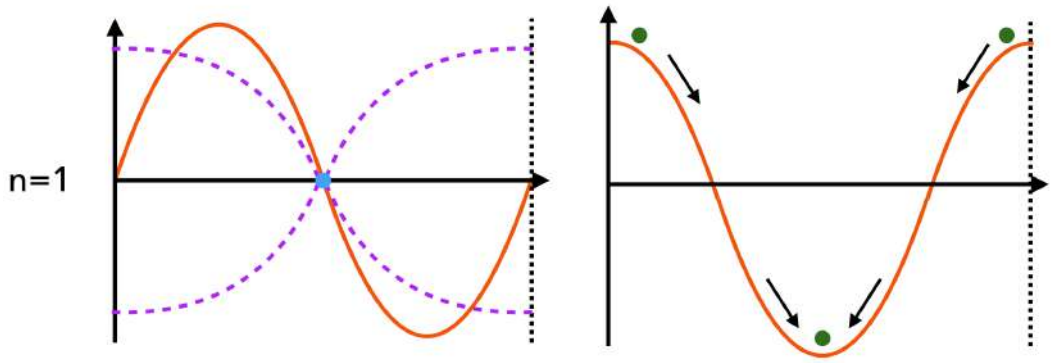

Fig. 2.6 Left: Distribution of the force(solid) and pressure (dotted-line) in a standing wave when the distance between the emitter and the reflector is such that a node can be created n=1. Right: the corresponding acoustic potential.

An effective trapping requires a local acoustic potential with high gradient this will provide trapping even against a background flow. The secondary forces (short distance forces) attract the particles to each other and help to stabilize particle clusters[153].

2.3 Design and fabrication of the acoustic resonator

An important part of this work has been device design, which is a key engineering challenge in order to accomplish efficient acoustic devices for ultrasonic cell manipulation. There are several considerations that need to be taken into account when designing an ultrasonic manipulation device, especially for half-wavelength layered resonators like the one used throughout this thesis, see also the ones used by Ohlin([125] or Bazou [9]). The first

consideration to bear in mind is the size range of the cells to be manipulated, as smaller particles (or cells) require higher operating frequencies to attain the same acoustic radiation forces than larger particles.
Bacteria size is around 3 μm long and 1 μm in width. Generally 1-10 MHz ultrasound is suitable for manipulation of 1-20 μm entities, that is the reason why the resonator was designed to work in a 2-5 MHz frequency interval. This implies that the nominal frequency of the transducer needs to be between this range. Also, it is important to heed whether to work in a single-pressure-node or a multi-node configuration. This is given by the distance (w) between the emitter (matching layer) and the reflector (top layer) and it is also related to the frequency at which the resonator is driven, as the wavelength of the emitted wave is given by:

$$\lambda = \frac{c}{f}, \tag{2.31}$$

and the distance between emitter and reflector layers relates the number of nodes n with the wavelength as in Equation 1.38.

The layered resonator is structured by different layers as seen in Figure **??** (B), the transducer generates the sound and is followed by the coupling layer, which is needed in order to get the good acoustic transmission into the system. Next follows the matching layer, sometimes called transmission layer, which forms the bottom of the resonator chamber and thus also acts as a reflector surface of the standing wave. The fluid layer contains the liquid and cells or beads. At the other end of the system is the reflector layer that is responsible for reflecting the incoming wave back into the fluid layer, giving rise to the standing wave.
It has been shown in simulations that a good resonator should have a matching layer of a quarter wavelength, a fluid layer of half a wavelength and a reflector layer of a quarter wavelength thickness. This configuration maximizes the Q-value of the system and results in a pressure minimum in the centre of the cavity and a pressure maximum at the channel wall.

To summarize, for our design we kept in mind the latter conditions as we want to work with a single pressure node since this makes imaging less complicated and prevents the interaction between bacteria clusters in different nodal planes. Additionally, since the choice of material plays an important role as well, we used a well-balanced combination of materials to achieve a system with high-quality value (Q-value).
The configurations of our layered resonators are (see Figure 2.7):

Fixed distance

The resonator is composed by three main layers: the reflection layer is a 3D-printed lid that wraps half ot the resonator and holds in place a circular Quartz-slide 250μm thick. The emission layer, which includes a circular Wrap-around Feedback Piezo-ceramic transducer (Pz-26) with a nominal frequency of 4.6 MHz (Meggit) that is glued with a conductive adhesive gel (Tensive) to a 3 cm ^{2} circular silicon (Si) wafer with 250 μm thickness. The wafer is attached, with Epoxy, to a hollow cylindrical shape made of stainless-steel with $h = 161\mu m$ and $r = 1.3$ cm dimensions. Note that the bottom of the pool (cavity) is the Si wafer and the wall is the saintless-steel cylinder. The support layer,at the bottom, is a hat-like stainless-steel structure with a slot for the wires and cables that connect the transducer. This part of the resonator keeps the system level and eases the manipulation on the microscope.

Adjustable distance

The resonator has five components: the emission plate, where another Wrap-around transducer (Pz-26) but with a nominal resonance of 3 MHz is glued in the same manner as before to a circular Si wafer with a 5 cm^2 area and 200 μm thickness. This wafer is firmly fixed into a stainless-steel structure. On top of the structure, the spacer, a Mylar ring whose thickness has to be half the wavelength of sound in water at the resonant frequency, which for 3 MHz is 250 μm. Over the Mylar spacer, a stainless steel ring is placed, the ring and the spacer create a pool between the emission and reflection plates. The reflection layer is a 500μm thick Quartz-slide permanently attached to an acrylic lid. As on the previous design, at the bottom the hat-like structure it is placed. Note that the Mylar spacer can be thicker or thinner depending on the driving frequency of transducer attached to the emission plate, this can change also the resonator from working in a multi-nodal manner to a single nodal one.

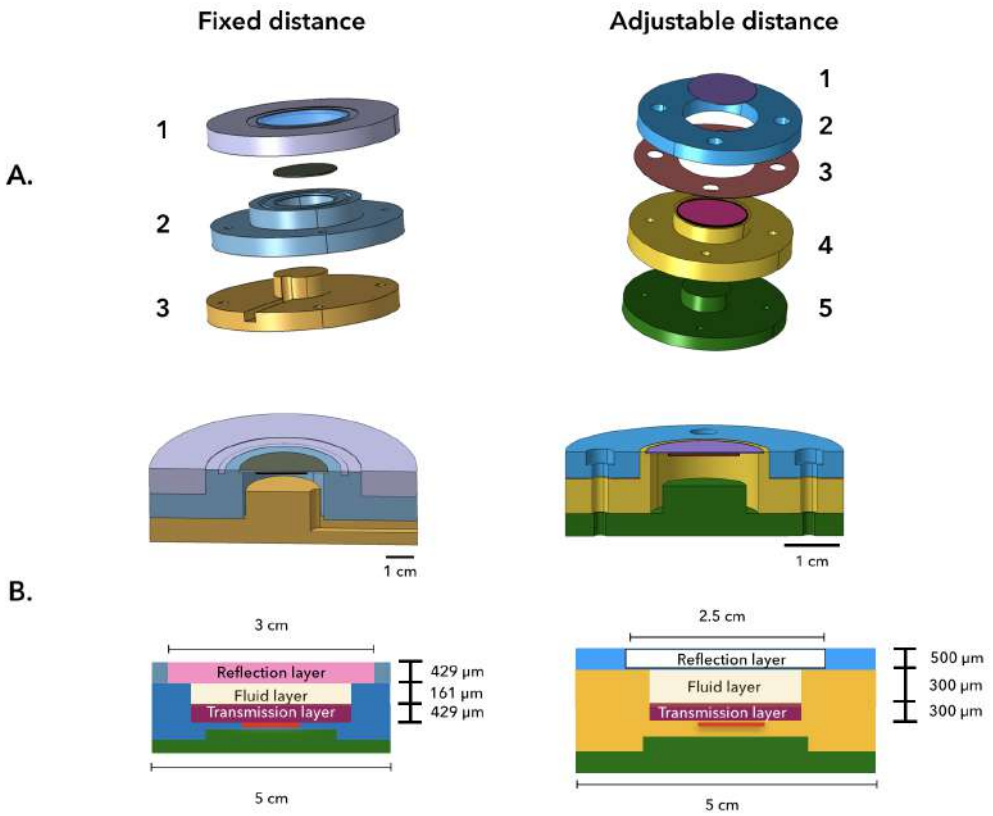

Fig. 2.7 **Components of the acoustic resonator.** **A.** 3D drawings of the two types of layered resonators designed for this work: a fixed distance one and another with modifiable transmission-reflector layer distance (w). The fixed distance configuration comprises three main layers. 1. The reflector layer, that corresponds to a 3-D printed lid that has a permanently fixed Quartz-slide. The Quartz-slide permits optical access for microscopic visualization. 2. Next, the transmission layer that comprises the Si wafer holding the transducer, the wafer is fixed to a hollow cylinder with $h = 161\mu m$ and $r = 1.3$ cm. 3. At the bottom a hat-like stainless steel supporting structure that holds the system and makes the manipulation on the microscope easier. On the right, the second configuration shows the adjustable distance resonator. The resonator is formed by five layers: 1. The reflection layer is a quartz-slide permanently attached to an acrylic lid. 2. A stainless steel ring is placed on top of the Mylar spacer (3.) that is placed on top of the steel framework holding the emission plate. 4. The emission plate comprises a transducer with a 3MHz nominal resonance glued to a circular Si wafer with a 5 cm^2 area and 200 μm thickness. The wafer is firmly fixed into a stainless-steel structure.5. Finally, at the bottom, the same hat-like structure as on the other design. Note that in both resonators there is a cavity (or pool) where the suspension is poured. **B.**Schematic diagram showing the real thickness of the three main layers for the resonators that we made. Not always they match the theoretical ones, nevertheless, because stainless steel and quartz have high-quality values the systems works and can trap beads in levitation.

2.4 Characterization of the acoustic trap

The first part of this section was performed in concert with Ludovic Bellebon as part of his master thesis[111] developed during the summer of 2017. The main goal was to measure the acoustic energy density of our acoustic resonator. The approach that was used is based on the z-position temporal tracking of latex and silica micro-beads in the cavity of the resonator. To get to know the acoustic energy density it is necessary to know the velocity of the particle during its z-displacement towards the nodal plane. For that reason, a well known optical phenomenon was used, Airy patterns. Airy disks are a bright region in the centre of the diffraction pattern resulting from a uniformly-illuminated circular aperture, which together with the series of concentric bright rings around it, is called Airy pattern [2].

When we observe an object in the microscope and it is completely sharp it implies that it is localized on the observation plane, whereas, when it is not, the object appears out of focus and blurry. From this, we can get that the further an object is from the observation plane the blurriest it gets. This phenomenon of optical aberration was used to characterized the acoustic trap that has a transducer working at a nominal frequency of 3 MHz ($\lambda = 500\mu m$). Since, as stated before, the resonator has a configuration that gives a single-pressure node standing wave. In theory the distance that should exist between the plates of the resonator is $w = (\lambda/2)$=250μm. Nevertheless, due to fabrication constraints the distance between plates is 300 μm. The best driving frequency, found experimentally, is 2.7 MHz, that matches with a 277 μm inter-plates distance. Even with these slight changes in the configuration, we can be sure that the pressure node is near the cavity centre.

Remembering equations 2.24 - 2.26 we can see that the acoustic contrast factor Φ characterizes the compressibility and density of the particles to handle therefore its value determines the position of the particles in the potential well (2.6); if $\Phi > 0$ particles will migrate toward the nodes whereas if it is $\Phi < 0$ they will migrate to the anti-nodes. For all these reasons, the properties playing a central role in the characterization of the resonator are the density ρ of the particles and the fluid and the compressibility κ.
A particle subjected to an acoustic field is affected by the Buoyancy force, the Stokes force F_S and the acoustic radiation forceF^{rad}. Following the description made by Dron *et al.*[50] the Buoyancy force can be neglected and $F^{rad} = F_S$ and from these he gets that the focusing speed for a particle in the cavity of and acoustic trap is:

$$u_F(z) = \frac{E_{ac} d_p^2 FYk}{12\mu} sin(2kz). \tag{2.32}$$

To determine $U_F(z)$ the optical aberration approach (Airy disks) was used. The diameter of the ring was followed from the bottom of the cavity (out of focus ring) towards the nodal plane (focus ring) see Figure 2.8 and later the focusing speed was deduced. Since the focusing speed was found experimentally, following the particle displacement versus time, equation, 2.32 was used to know the acoustic energy density E_{ac} of the system at a given position.

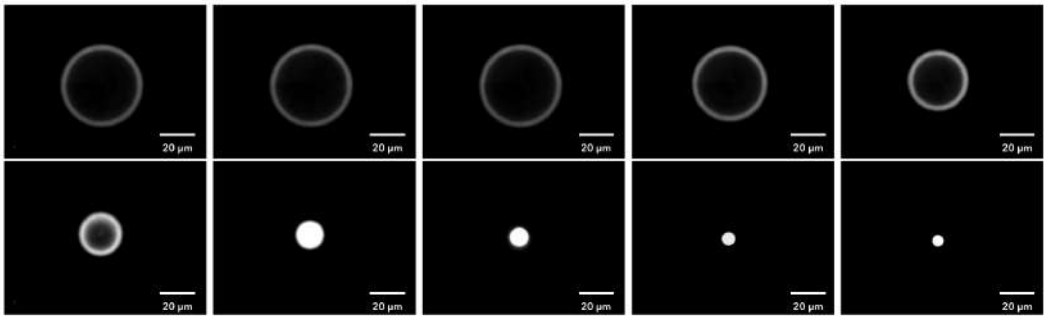

Fig. 2.8 Airy disk evolution during the migration of a latex bead towards the levitation-plane (nodal plane). Just one latex bead was selected for the z-migration, each image was taken 1 second apart, the Voltage applied during this experiment was 10 Vpp.

Our layered resonator, with an adjustable distance configuration, had a nodal plane at 80 μm and that the focusing speed depends on the voltage that is applied to the transducer, at higher voltages higher the maximum focusing speed. As expected, the acoustic energy density in the resonator also varies linearly with respect to the applied voltage as we depicted in indent B on Figure 2.9.

The difference in E_{ac} between latex and silica beads shown in Figure 2.9 can be explained because the energy distribution on the surface of the resonator is not homogeneous. The pressure field on the surface of the transducer is characterized by the fluctuations that are present as previously described by Bruus et al. Even when the Airy disk approach permits to have an idea of the magnitude of the acoustic energy it is just in one point of the total surface of the resonator, it is clear that a better approach should be made to have an idea of the spatial energy distribution in our cavities.

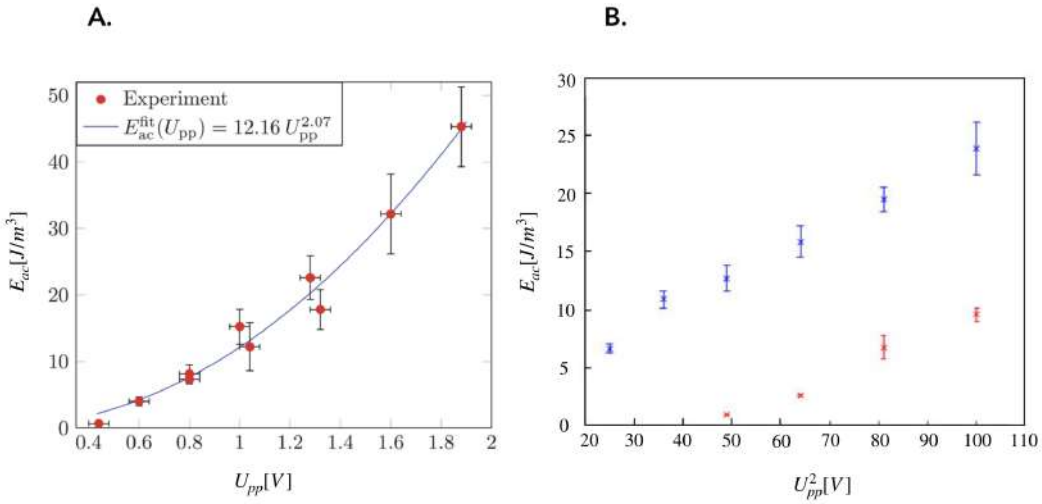

Fig. 2.9 **Acoustic energy density versus applied square peak-to-peak voltage. A.** Measured acoustic energy density E_{ac} versus U_{pp} on the piezo transducer (each point) for a $\frac{1}{4}\lambda$ resonator. Measured on the micro-resonator used by the Barkob et al. The full line is a power law fit to the experimental data.**B**. E_{ac} vs U_{pp}^2 measured on our self-made resonator with adjustable inter-plane distance. The blue dots represent the measurement obtained with latex particles and the red ones with silica beads. Each point is the average of five measurements. The points without error bars correspond to single measurements[111].

2.5 Discussion

We have fabricated two types of half-wavelength parallel-plates resonator that are functional. On one hand we have one whose thickness its fixed which facilitates the handling but if broken it is more difficult to fix as it needs transducer with a specific driving frequency. On the other hand, a resonator whose thickness can be modify enabling having mono or multi nodal configuration.

Both types, present an heterogeneous distribution of the acoustic energy on their surface. For this reason the presence of multiple cluster of particles is inevitable. However, we have developed a protocol that establish a specific working are we the energetic hot-spots are fixed.

Considering the literature on half-wavelength resonators our working frequencies do no damage cells, therefore it can be used to our main aim; the trapping of self-propelled bacteria.

Chapter 3

Escherichia coli under acoustic confinement

3.1 Generalities on *Escherichia coli*

Escherichia coli has lurked within our ancestors for millions of years, before they were even human [193]. The story of *Escherichia coli* begins with a German pediatrician, Theodor Escherich, who while isolating bacteria from the diapers of healthy babies noticed a rod-shaped microbe that could produce a "massive, luxurious growth" and called it *Bacterium coli commune* [68]. *Escherichia coli* lives in our gut. Its breed has been studied intensively for a century and they belong to the better understood species on the planet. It is versatile and quite sophisticated. Through *E. coli* a shared ancient history can be seen. A history that includes the origin of complex features in the common ancestor of all living things, cells. *Escherichia coli* can take us back in time and hint us about the evolutionary pressures that shape important cues for our present existence [193].

The shape of this microorganism is considerably simple when compared to the those of higher eukaryotes. Its morphogenesis; a cylindrical tube with hemispherical caps 2.5 μm long by about 0.8 μm in diameter [119]—as Howard Berg said: "it resembles a microscopic cocktail sausage" [11].

The silhouette of many microorganisms can be understood in terms of the general surface stress hypothesis, based on the theory of soap bubbles [97]. For a rod-shaped gram-negative bacteria like *Escherichia coli* the comparison to cylindrical soap bubbles has been very helpful; it is well known that cylindrical bubbles are created by two fixed rings and as

anticipated, the physical properties of the rings and the membrane of the bubbles should somehow resemble those of bacteria polar caps and lateral walls respectively. A spontaneous burst in the centre of a cylindrical bubble when the length reaches twice the radius multiplied by π mimics cell division [83, 119].

The Gram-negative bacteria cell division comprises three major steps: the first step involves the replication of DNA, followed by an elongation where the cell becomes twice as long. The last step comprehends a constriction of the elongated cell in the middle and the separation of the two daughter cells. The detailed process is complex and involves several proteins and interactions among them that are not yet fully understood [45, 147, 177].

3.2 Motility of *Escherichia coli*

The organelle of motility in *E. coli* is the bacteria flagellum, consisting of a rotary motor, a helical filament, connect to the bacteria flagellar filaments by a flexible hook [12, 76]. The nanomachine that drives the motion of the flagella is called Bacterial Flagellar Motor (BFM), whose basal body spans the cellular envelope and is comprised of several trans-membrane rings. These rings are approximately 45 nm in diameter, containing around 25 different types of proteins [123].
The rotation of the motor takes place via an interaction between one or more membrane-embedded torque-generating stator units and spore-like proteins along the periphery of the rotor rings. The interaction is powered by the ion-motive force arising from the transit of protons [12, 117].

This bacterial nanomotor is extraordinarily efficient, it can convert the free energy stored in the transmembranal electrochemical gradient into mechanical work. Typically it rotates at approximately 30 Hz, and it can propel the bacteria at speeds up to 100 $\frac{\mu m}{s}$, that is 100 body lengths per second [12, 26, 76, 113].

The dynamics of a single bacterium, considered in the area of active matter as a run-and-tumble particle (RTP), consists of periods of persisting swimming motion called runs, punctuated by sudden changes of direction known as tumbles [92]. During a run, all the flagella —relatively stiff helix that is rotated by a motor embedded in the cell wall— are rotating counter-clockwise wrapping into a bundle that pushes the cell along at speeds of 20-35 μ m/s [12, 13]. Due to the chirality of the flagella their clockwise motion an their counter-clockwise do not produce the same displacement. If one or more of the motors

reverse, the corresponding flagella will leave the bundle and undergo a polymorphic transformation in which the handedness of the helix changes modifying the swimming direction of the cell, that is, the bacteria experiences a tumble [12].

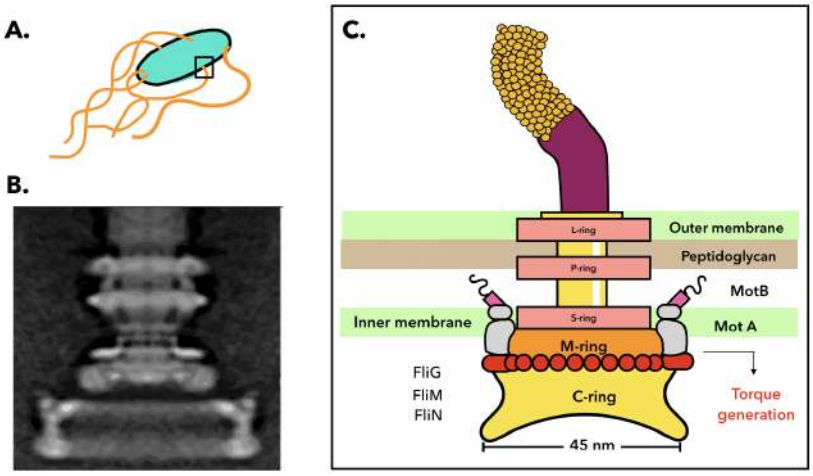

Fig. 3.1 **Bacterial Flagellar Motor A.** *Escherichia coli*, as any other member of the *Enterobacteriaceae* family, is motile via peritrichous flagella, this implies the presence of multiple randomly distributed flagella over the entire bacteria cell. *E. coli* self-propulsion depends on the direction of rotation of its flagella. During a run all the filaments rotate in the same counter-clockwise direction and in a tumble not only the direction of the rotation, of one or more flagellar filaments, changes but also the handedness and pitch. The rotary nanomachine driving the self-propulsion–swimming–is known as bacterial flagellar motor, in the micrography (**B**) a part of the motor that is attached to the hook is shown. The image depicts what would be seen in this part of the motor as it rotates [60]. **C.** Structures outside the cell wall include the filament, which can be up to 10 μm long and circa 20 nm of diameter; the hook, a flexible coupling or universal joint. The elements embedded in the cell wall comprise the basal body and include several rings and a rod. The outer pair of rings (L-ring and P-ring) serve as a bushing that gets the rod through the outer membrane. The rod is a drive shaft. In the inner part the rings M-ring and S-ring as just a M-S ring since they are product of the same gene FliF Additionally, the C-ring comprises part of a motor switch complex (FliG, FliM, FliN) that controls the direction of flagellar rotations and has an impact in the torque generation [116, 171].

The displacement of *E.coli* consist thus of periods, of assumed, straight line swimming interrupted by brief burst of rotational motion (see figure 3.2). A typical run lasts about 1 s; to a reasonable approximation the duration of runs is Poisson-distributed, so that tumbles can be viewed as random events occurring with a fixed rate α each of which decorrelates the

swimming direction.
Tumbles are normally shorter, of duration $\tau \simeq 0.1s$, and often treated as instantaneous $(\tau \to 0)$ [23].

At time- and length-scales much larger than α^{-1} and $l \frac{v}{\alpha}$ this motion is a diffusive random walk. The diffusivity in d dimensions is given as [23]:

$$D = \frac{v^2}{\alpha d} \tag{3.1}$$

This diffusivity is hundreds of times larger than what would arise by the Brownian motion of colloidal particles of the same size-as can be experimentally checked using deflagellated mutants [23].

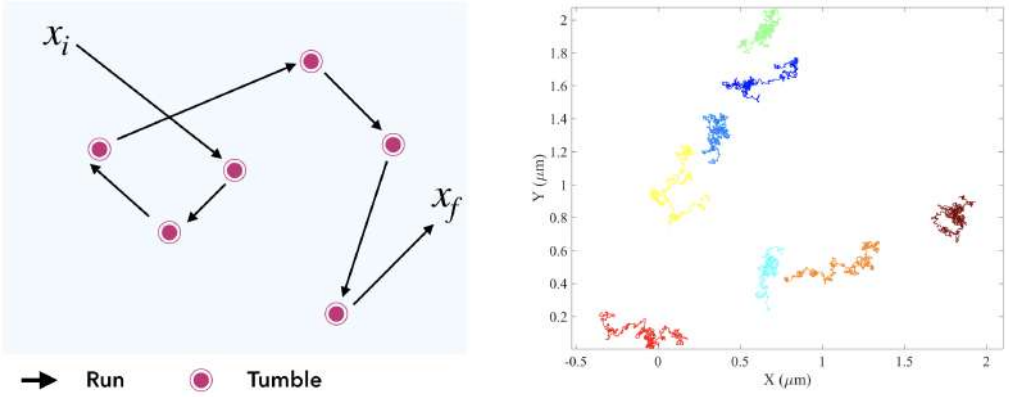

Fig. 3.2 **Schematics of run-and-tumble behaviour.** General description of run-and-tumble behaviour and reconstructions of the swimming trajectories for *Escherichia coli* MG1655-Jovanovic-GFP.motile+.

3.2.1 Chemotaxis

Another well known motility-related phenomenon exhibited by *E. coli* is chemotaxis. Chemotaxis is defined as the movement of an organism in response to a chemical stimulus. In particular motile bacteria responds either to chemo-attractants or repellents depending which one is present in the more effective concentration [1]. It was shown that in *E. coli* a processing mechanism that compares opposing signals from the chemoreceptors for positive and

negative taxis, sums these signals up, and then communicates the sum to the flagella [1].

As outlined previously, chemotactic bacteria can move themselves up a chemical gradient (∇_c), where c is the concentration of a chemoattractant, by modulating their tumbling activity. For a chemorepellant, the sign of the effect is reversed [23].
Several numerical and mathematical approaches have modeled this phenomenon [23, 54, 150] considering that a bacterium has an on-board biochemical circuit whose job is to modulate the tumble rate according to:

$$\alpha = \alpha_0 - \int_{-\infty}^{t} K(t-t')c(t')dt'. \tag{3.2}$$

Where α_0 is a value arising when $\nabla_c = 0$. This baseline value can depend on environmental factors, but is broadly independent of overall shifts in the concentration of c chemophore [23]. This implies that $K(t)dt = 0$. Moreover, $K(t)$ (a Kernell) is a bilobed function which essentially computes the change in local concentration c experienced by the bacterium over a certain time scale. If this change is positive, the next tumble is delayed proportionately. On the contrary a negative change conversely promotes tumbles, although experiments in fact suggest a delay-only, one-sided response [23].

3.2.2 Density-dependent motility

On systems in which run-and-tumble parameters (v,α) vary in response to the local density of bacteria a true many-body problem arises [23]. To address this case it is necessary to derive an equation for the collective density field [23]:

$$\rho(r) = \sum_i g(r - r_i), \tag{3.3}$$

where the sum over N particles and g is in principle a delta function in which a finite range of g is introduced. At this point it should be chosen whereas to define a probability density in the N-body configuration space and derive a Fokker-Planck equation or work with the Langevin equations for N particles.
The typical approach is to set the Langevin equations with spatially varying run-and-tumble parameters and then allow this variation to occur through a functional dependence on the density field [23]. Where after the functionals of density for the diffusivity $D[\rho], x$ and the

drift velocity $V([\rho],x)$ enter a many-body functional Langevin equation it reads in 1D:

$$\dot{\rho} = \left(-\rho V + D\rho\prime + (2D\rho)^{\frac{1}{2}}\Lambda\right)\prime, \tag{3.4}$$

with Λ as a unit for white noise. The last term goes by fixing $\rho = NP$. Through their numerical experiments [22] established that the interacting run-and-tumble system can be mapped at large scales onto a set of interacting Brownian particles and that when $v(\rho)$ and $\alpha(\rho)$ are the same for right and left-moving particles and depend on density in a purely local way the system is equivalent to a fluid whose free energy density with K_BT is:

$$f(\rho) = \rho\,(\ln\rho - 1) + \int_0^\rho \ln v(u)du \tag{3.5}$$

This implies that when $v(\rho)$ is a sufficiently rapidly decreasing function of ρ the local free energy density $f(\rho)$ has negative curvature in an intermediate range of densities. At which the system is predicted to show a spinodal instability, separating into domains of two coexisting binodal densities ρ_1 and ρ_2 corresponding to a common tangent construction f as shown in figure 3.3

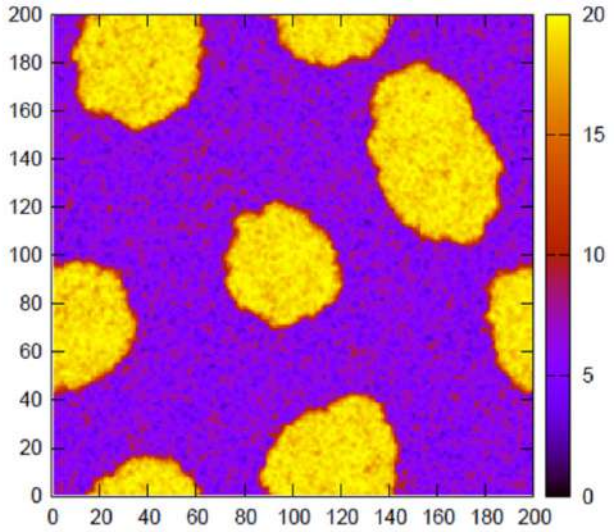

Fig. 3.3 **A 2D run-and-tumble system undergoing motility-induced phase separation.** Simulated via a lattice model (200 × 200 sites) as detailed in, with local density (particles per site) colour-coded on the scale to the right
[23, 170]

In these numerical experiments [22, 23, 134], domains also form by a different mechanism, such as nucleation and growth, in the density range that lies between the binodal and the spinodal. In this range the system is stable to local perturbations but unstable globally [23]. The physics behind such motility-driven phase separation established that run-and-tumble particles accumulate (i.e. increase in ρ) wherever they slow down reducing their v [22, 23, 134]. But if the velocity is a decreasing function of density, this implies that bacteria also slow down on encountering a region of higher than average density. This creates a positive feedback loop which, as long as $v(\rho)$ decreases fast enough, runs away to phase separation.

When this numerical approach is compared to normal microbiological phenomena, it matches the aggregation bacteria encounter when they form dense clusters from a uniform initial population. In microbiology this down-regulation of bacteria motility is related to the formation, from planktonic swimmers in dilute suspension, of a biofilm [70].

3.3 *Escherichia coli* under confinement

The presence of boundaries can influence the dynamics of swimming microorganisms, just as other nearby cells. Confinement highly impacts cell locomotion because the concentration of chemical species that affect the motility of the micron sized organisms changes. The same for the hydrodynamic stresses acting on the cells, which determines that the near-wall motility is different from the one exhibit on bulk [103, 102].

Four distinct types of wall-influence on the swimming kinematics in some microorganisms are [103]:

1. **Decrease of swimming speed near the wall**: since viscous drag increases as a body comes closer to a boundary, it might be expected that a cell would slow down. However, since the propulsion method is also drag-based this is not always the case [103].

2. **Changes in their swimming trajectories:** In an infinite fluid *E. coli*, on average, in a straight line. On the contrary, near a wall, the helical flagella rotate, creating a net force on the cell at a right angle with respect to the motion and parallel to the surface. There is an exact and opposite force acting on the cell body, which rotates in the opposite direction as the flagella and the net effect is a wall-induced torque. Since a swimming bacterium is in fact torque-free, the cell cannot swim straight but instead rotates at a

rate such that the viscous torque from that rotation exactly balances the wall-induced torque, and therefore swims along circles on the surface [103].

3. **Attraction and re-orientation:** a single cell swimming near a solid wall sets up a bipolar flow field [48], which does not satisfy the non-slip boundary condition on the wall and images of the cell arise. Due to these images, the cell is subject to the gradients of the image flow field and rotates in the direction parallel to the surface and perpendicular to the cell body [103]. In a confined environment, these cells are therefore always swimming toward a surface, a result which also leads to their accumulation [103].

4. **Potential reduction of cell-cell hydrodynamic interactions:** swimming cells typically behave as force dipoles in an infinite fluid, but when near a solid surface, configurations exist where the total flow field (dipole + images) ends up decaying as $\frac{1}{r^3}$ or $\frac{1}{r^4}$, and hydrodynamic interactions with other cells are weaker as a result [103].

3.4 Acoustic confinement of *E.coli* cells

As discussed before, the effects produced on bacterial cells by confinement or boundaries are well known and greatly discuss in the literature. Nevertheless, not all the clustering of bacteria arrives due to the presence of boundaries. For example, motility-induce phase separation also known as aggregation, takes place in dense communities [22].

Moreover, biological locomotion near boundaries includes surface-associated bacterial infections [35, 72] and biofilm formation [130, 10], but biofilms or bacteria not always attached to real surfaces. For example, biofilms on the air-water interface occur regularly on nature [37, 161, 181].

Our technique provides a confinement without surface interactions which is the reason we use it to evaluate the collective phenomena of bacteria. Also, we assessed the possibility of creating a synthetic floating-biofilm.

3.5 Model microorganisms

Escherichia coli has proven to be a good model to study motility and biofilm development. For this reason, the Gram-negative bacteria was selected as the model microorganism for the experiments performed in this thesis. Several considerations were made to select the *Escherichia coli* strains suitable for our experiments. First, motility is considered an important parameter in the analysis of phenomena arising under confinement of microorganisms; second, a highly motile strain was selected and thirdly, a motility mutant of the such strain was constructed.

Motile strains

Escherichia coli*-RP437-*pzA3R-YFP

Considered as a wild-type strain for motility and chemiotaxis assays, is a *E.coli-K12* derivative. It has an average swimming speed of 17±3 when supplemented with a motility buffer.$\mu m/s$ [152].

***Escherichia coli* MG1655-Jovanovic.Motility+**

This bacteria strain is considered as a wild-type, it is also a derivative of *E.coli-K12* with a MG1655 genetic background. The strain is highly motile due to an insertion in the genome that disrupts the gene *yeaJ* (dgcT encoding a diguanylate cyclase), the deletion of *yeaJ* determines the reduction in cyclic diguanosine monophosphate (c-di-GMP) production that results in increased swimming motility. The cells have an average swimming speed of 15±3 μm/s.

***Escherichia coli* MG1655-Jovanovic_IATT:Amp*GFPmut3*.Motility+**

This strain is the fluorescent version of the latter via a chromosomal integration of the green fluorescent protein (GFP) The integration vector, constructed by our collaborators at Pasteur Institute, allows the introduction of the *gfp* gene into the chromosomes of Gram-negative bacteria. The average speed is the same as its non-fluorescent counterpart.

Non-motile strains

***Escherichia coli*MG1655-Jovanovic-IAAT:Amp-GFPmut3 Δ fliE-R::Cm**

Non-flagellated version of the Jovanovic-GFP motility+ via a deletion of the gene fliE-R, that codifies the flagellar hook-basal body complex protein FliE, inhibiting the production of flagella.

Note: The wild-type Jovanovic strain and the fluorescent and deflagellated strains were kindly and constructed, respectively, by our collaborator Dr. Aimee Wessel at the Génétique des biofilms group at Institute Pasteur).

We re-named the strains to ease their reference throughout this manuscript:

***E.coli*-RP437**: *E.coli*-RP437-*pzA3R-YFP*

Jovanovic-motile+: *E.coli* MG1655-Jovanovic.Motility+

Jovanovic-GFP.motile+: *E.coli* MG1655-Jovanovic_IATT:Amp*GFPmut3*.Motility+

Jovanovic-GFP.non-motile:*E. coli*MG1655-Jovanovic-IAAT:Amp-GFPmut3ΔfliE-R::Cm

3.5.1 Bacteria cultures

Short-term stock of bacteria strains

Escherichia coli MG1655-Jovanovic.Motility+, *Escherichia coli* MG1655 Jovanovic-Motility+ and *Escherichia coli* MG1655 Jovanovic-Δ$fliER$ cells were streaked in Lysogeny broth (LB) agar plates. For the non-fluorescent motile strain the agar plates did not contained antibiotics, whereas for the fluorescent strains, both motile and non-motile, the agar plates were supplemented with 100 μ ml^{-1} of Ampicillin (AMP). Ampicillin was added because the bacteria is resistance to it, and it helps to make sure that the cells arising on the plate are indeed Jovanovic. The agar plates were incubated overnight at 30 °C and later placed inside the fridge at 4°C. The agar plates were made in duplicate for each strain and they served as ready-to-use weekly stocks.

Planktonic cultures

To avoid having bacteria cells in the so called adhesive-sedentary lifestyle, that is known to affect the phenomena that typically arise with a motile-planktonic phenotype, we started from over-night cultures and prepared fresh ones to work the same day.

1. *Escherichia coli*-RP437-pzA3R-YFP

E.coli-RP437 cells were cultured overnight from -80°C stock in M9 minimal media supplemented with casaminoacids at 30°C and aerated with orbital shaking (250 rpm) until mid-exponential phase. The overnight suspension was centrifugated for 5 minutes and a pellet was obtained. Next, the supernatant was discarded and the pellet resuspended in a motility buffer supplemented with DL-Serine that inhibits cellular division. Subsequently, a dilution of the sample is made and a working suspension with O.D=0.1 is obtained.

2. *Escherichia coli* Jovanovic MG1655

For each strain plated on the agar surfaces a single-colony isolate was used to inoculate 5 ml of LB medium. The suspension was incubated overnight at 30°C on a rotary shaker at 250 rpm. The typical optical density (O.D) reached by the suspensions after the overnight growth is higher than 1.5 which corresponds to the stationary phase in the growth curve of these microorganisms. From the overnight suspension, a fresh culture was re-started with an O.D.=0.05, it was incubated under the same conditions as before until it reached mid-exponential phase (O.D=0.5). The latter liquid culture was diluted five times, the diluted suspension is the working one and it is the one used to inoculate the cavity in all the experiments. According to the McFarland standard the number of colony forming units (CFU) at the working optical density is around 1.5 X10^8 [167]

3.6 Experimental set-up

The set-up used for all the experiments performed throughout this thesis is composed by three major sections around the acoustic trapping system (see figure 3.4).

Acoustic trapping system

As previously described (see Chapter 1), the major components of the acoustic resonator are an emission plate, where a piezo-ceramic transducer is glued to a circular Si wafer; a cavity

where the bacteria suspension is poured (fluid layer) and on top, a quartz reflector plate that is permanently attached to a plastic lid. The specifics of the components are described on figure 2.7

Acoustic input control

This part of the set-up supplies the sinusoidal voltage to the piezo-ceramic transducer. Composed by a function generator (LXI Keithley 3390 50 MHz) connected to an amplifier (E Tabor Electronics Dual/Differential wide-band 9250) to increase 10 times (10X) the amplitude of the signal. The output signal is sent to the acoustic resonator and also, to a LeCroy Oscilloscope (WaveAce 214). The oscilloscope allows the observation of the supplied wave form and eases the experimental localization of the resonance frequency of the transducer.

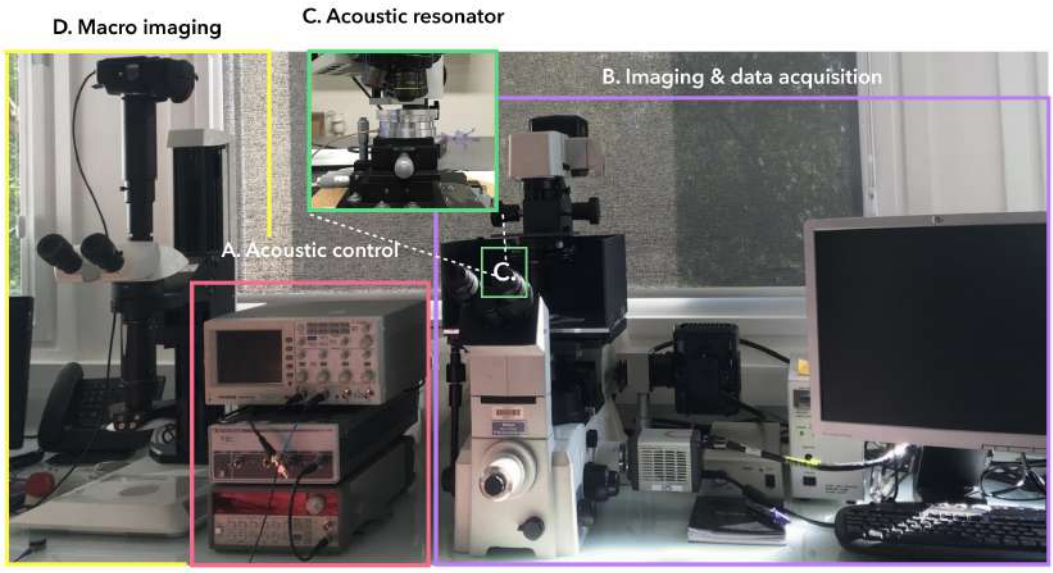

Fig. 3.4 **Experimental set-up.** Color-coded the four blocks of the set-up.**A.** The acoustic input control (pink) composed by a wave form generator, working in the continuous mode, a signal amplifier (10X) and a oscilloscope. **B.** As the imaging system (violet), a reflection optical microscope coupled with a Hamamatsu camera. The camera is controlled on the computer with the ImageHC software. **C.** On top of the microscope stage the acoustic trapping resonator (green) is placed. **D.** The macro imaging block composed by a digital camera connected to a stereo-microscope (yellow).

Imaging and data acquisition

The visualization of trapping was done with an Olympus reflected microscope to which an Hamamatsu Orca flash 4.0 camera is coupled; also, a XYZ-stage (Thorlabs) is used to place the acoustic resonator and control the imaging zones. The control of the microscope and the stage was done manually and the camera was controlled with the HCI-Image Live Software.

Macro imaging

A stereo-microscope (Leica) coupled with a D850 Nikon digital camera was used to acquire the macro view of the cluster on the resonator during and before the trapping process.

3.7 Material and Methods

3.7.1 Inoculation of the cavity

Two acoustic resonator with the same dimension and previously sterilized—via ultraviolet germicidal irradiation for 20 minutes—were inoculated with 500 μl of the working suspension and sealed with the reflector lid. The control resonator is placed on the bench and left there until; immediately the other resonator, used to perform experiments, is place on the microscope stage.

3.7.2 Clustering and spreading

The clustering process entails a competition between the pressure induced by the acoustic radiation force, described in Chapter 1, which confines cells into a quasi-2D levitation zone at the nodal plane, and the swim pressure of bacteria [67]. Once a cluster is formed when the trapping acoustic forces are removed, the cluster enter a spreading phase.

To evaluate this dynamics the inoculated acoustic resonator was placed on the microscope stage. The well-known self-propulsion of the motile bacteria or the Brownian motion of the non-motile cells were registered in a 30s video –with a frame rate of 50 Hz and an exposure time of 20 ms– which serves as a control of bacteria activity. The control video is useful, as it has been reported that some *E. coli* strains can experience a change in phenotype due to the over-expression of antigen 43, which is an outer-membrane protein that mediates auto-aggregation in liquid culture [41]. That is the case of all Jovanovic strains. A similar

case takes place on the RP437 strain, where non-motile variants arise in room temperature stab cultures [133].

Immediately afterwards—to avoid attachment of the cells to the cavity surface—the acoustic resonator was connected to the acoustic input control block. The standing wave is created inside the cavity and the acoustic forces arise (see Chapter 1), prompting the displacement of bacteria towards the node of the wave (i.e. levitation of bacteria) and once there the secondary forces will enhance the stabilization of the levitated cluster (see3.5).

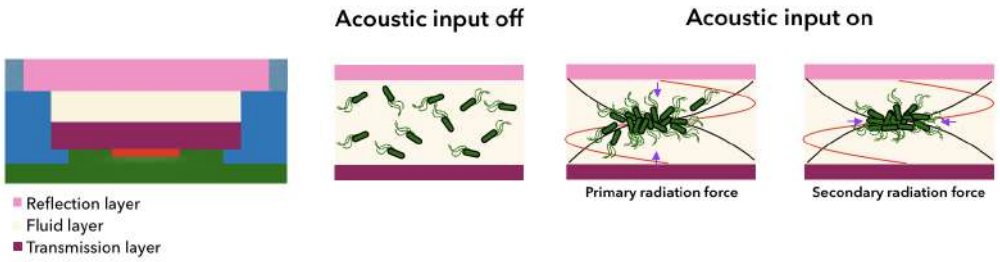

Fig. 3.5 **Schematics of the clustering process.** At the left a representation of a fixed distance resonator prior to inoculation, followed by a representation of the clustering process inside the cavity of the same. When no acoustic input is present (acoustic input off) the bacteria cells are distributed in the entire cavity. Immediately after the acoustic input is send the acoustic waves interact with the bacteria suspension and the F^{rad} arises, prompting the displacement of bacteria towards the nodal plane followed by the consolidation of a cluster in levitation via the secondary forces.

The clustering process was recorded using a 50 Hz frame rate, the length of the acquired video is 1 minute. It is important to emphasize the difficulties to record the complete evolution from the beginning. Firstly, the energy distribution in the trap is not uniform. Therefore, it is likely that several bacteria clusters form in zones where the local energy density is high. Moreover, the system is sensitive to the slightest modification in the parallel plates and this will have an impact in the acoustic energy distribution and therefore, in the position and numbers of clusters, see Figure 3.6.

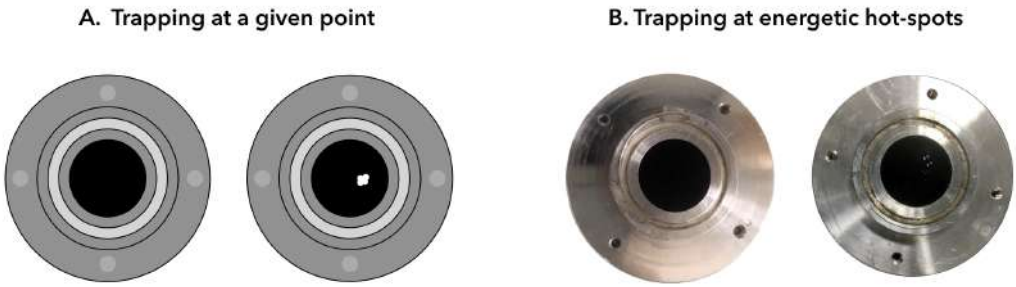

Fig. 3.6 **Schematics of the idealized clustering *versus* the achived cluster observed in our system. A.** Ideal acoustic trapping at an specif point. **B.** Due to the heterogeneous distribution of energy in our acoustic resonator, bacteria are trapped in the energetic hot-spots leading to formation of several cluster.

The zones that we picked to record from the heterogeneous distribution up to the clustering were selected based on the macro characterization of the resonator. Remember that the zone where the cluster appeared remained the same for all the strains. The cluster can change position but within a delimited zone, therefore this was the working area for all experiments unless is stated the contrary. Later, in order to characterize the clustering and spreading dynamics we use an approach similar to the one used to study the processes of aggregation and disintegration of clusters of non-Brownian paramagnetic beads [64]. The radial mass distribution was calculated–in our case the mass is considered as the number of bacteria-pixels–as follows:

$$g(r) = \frac{[M(r+\Delta) - M(r)]}{[\pi(r+\Delta^2) - r^2]}, \tag{3.6}$$

where M is the dimensionless mass (intensity of the pixels) normalised by the total area of the ring with radius r and thickness Δ. The temporal evolution of $g(r)$ was obtained from the videos acquired using the camera coupled to the microscope. For the acquisition the recording settings were Binning 1, image size as 1024×1024, 16 bits depth and a frame rate of 50 Hz.

Afterwards, using a custom-made Matlab code, the grey scale images were improved using a median filter that replaced each pixel with the median value in its 3×3 neighbourhood–the filter reduced the background noise. Later, we performed a background correction where the first frame of the video, corresponding to the nodal plane where no bacteria are in focus, was

considered as the background and it was subtracted from the rest of the frames. For each video frame, the intensity of the pixels contained in a annular mask, positioned at the centre, was measured and then divided by total area of the ring. The ring-shaped mask grows radially with a step Δ, corresponding to the average length of a bacteria, covering the entire video frame. On the case of the spreading dynamics, firstly, we selected a consolidated cluster based on the following aspects: the cluster should be dense, which implies that it was formed in a spot of maximum energy density; it should fit the working area of the microscope to be able to record the re-distribution of cells. Later, the acquisition and video treatment protocols were used.

3.7.3 Analysis of the flow dynamics within a levitating cluster

When bacteria displacement is constricted by walls, either physical as in the case of PDMS microchambers or Hela cells, or virtual, like magnetic, optical or acoustic traps, and the cell density is high bacteria suspension display a sudden collective or "bio-turbulent" behaviour [49]. In our case, when the cells are trapped at the nodal plane in a consolidated cluster, they exhibit such a turbulent state. In order to characterize the global dynamics within the cluster we use particle image velocimetry (PIV), a well known non-intrusive method normally used for flow visualization.

Particle image velocimetry (PIV) is an experimental flow measurement technique. The measurements are carried out through the addition of tracer particles (fluorescent beads) to gain insight into the surrounding fluid flow. The tracking of the particles is accomplished by their illumination, using a laser light source, and capturing their displacements using one or more cameras. The image sequence, capturing the particles displacement over a time, are processed using a correlation algorithm to determine the spatial displacement of the particle. The spatial displacement and the time interval between illumination, vector maps representing the particle movement and the corresponding flow, can be generated.
There are different types of PIV measurements classified by the needed equipment and resolution of the measurements. We are particular interested in using Micro PIV, as the velocity resolutions are on the scale of micrometer, which is the range of the mean speed of bacteria.

Taking into account the dimensions of our acoustic resonator and the physical phenomenon arising in the cavity (acoustic forces and streaming) we realized it is not possible to use particles as tracers, due to the fact they respond to the acoustic field and instead of providing

a visualization of the flow they tend to accumulate at the centre of the cluster. Since our aim is to visualize the flow of the bacteria suspension and not the flow generated by ultrasound in the surrounding fluid we decided to use a mixture of fluorescent and non fluorescent bacteria. The non-fluorescent bacteria will act as the flow to trace and the fluorescent one are the tracers.

Inoculum

Planktonic liquid cultures were prepared in the same manner described above. In accordance with the latter, both working suspensions–for non-fluorescent and fluorescent bacteria–have an OD_{600nm}: 0.1. The final inoculum is a mixture (7:3) of the working suspensions corresponding to Jovanovic motility+ and Jovanovic-GFP motility+. The mixture was swirled and the cavity was inoculated as stated in previous sections. Note that the final concentration of the inoculum is again OD_{600nm}: 0.1

Evaluation of Kinetic energy (E_{xy}) vs Acoustic energy (E_{ac})

In Chapter 1 we established there is a linear relationship between the applied peak-to-peak voltage U_{pp} on the transducer and the acoustic energy density E_{ac}. This implies that the modification of the applied voltage changes the magnitude of the acoustic forces interacting with the particles and hence the confinement strength. This situation is analogous to the study of how the inter-wall distance, on microfluidic channels, modifies the emergence of collective behaviours on bacterial suspensions.

To evaluate the effect of the confinement strength on the emergence of the turbulent flow within a cluster in levitation, the cavity was inoculated using the already established protocol. The transducer driving frequency at 20 U_{pp} was found experimentally and the clustering process took place; then we waited for 20 minutes until the consolidation of a cluster. Afterwards, 90 minutes video,with the same conditions as always, was recorded. A second video was the acquired. The first 20 s correspond to confinement at $20U_{pp}$ and the remaining 70 s with a 18 U_{pp} input. The same was repeated until 10 U_{pp} was reached, see figure 3.7.

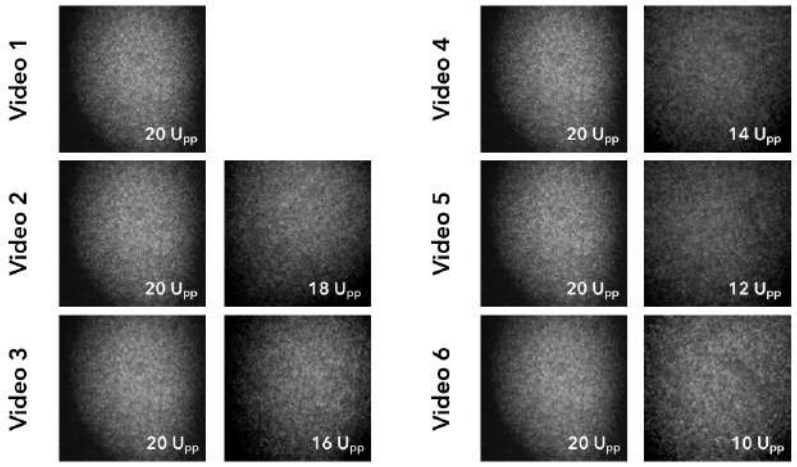

Fig. 3.7 **Images sequence acquisicion to evaluate E_{xy} vs E_{ac}.** A cluster in levitation was picked to evaluate the turbulent within itself. The driving frequency was conserved throughout the experiment. The first video corresponds to the dynamics of a cluster with a strong confinement ($20U_{pp}$). The first 20 second of the second video registered the dynamics of the cluster at $20U_{pp}$, immediately the voltage was reduce to 18 U_{pp} while recording the remaining 70 seconds of the video. Next, the voltage was increased again to 20 U_{pp}. The voltage was modified in the same manner, with a rate of 2 Volts per step, until $10U_{pp}$

Quantification of bacterial flows

The images were analyzed considering that the the acoustic confinement yields quasi-2 dimensional clusters and also that, from the acquired in-plane images, 2D projected velocities of 3D suspension motion can be analyzed. A Matlab code, inspired on the PIVLAB Matlab toolbox, made in collaboration with Dr.Alexandre Vilquin was used to determine the bacteria flow velocity (v_x,v_y) from the fluorescence micrographs. In the aforementioned code, a temporal filtering, which permits to avoid non-physical velocity gaps between two frames, is applied to all the frames. Later, we can manually validate the vectors assigned followed by interpolation for the missing data. A median filter to reduce noise is applied. The velocity of the flow and its rotational is calculated, obtaining the velocity and the vorticity fields, see figure 3.8.

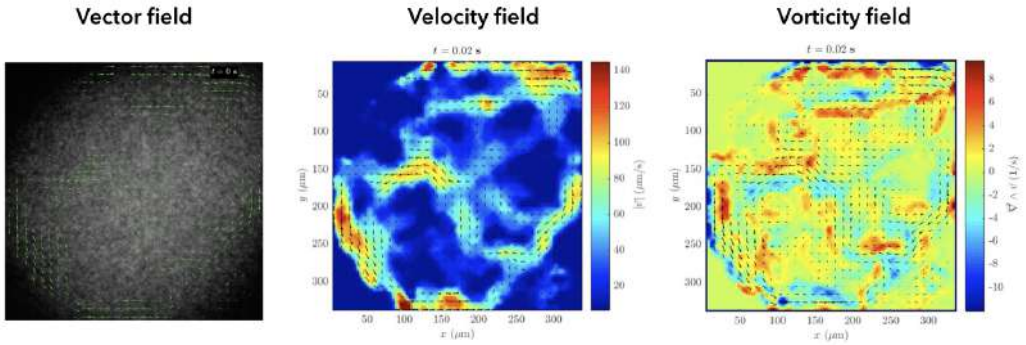

Fig. 3.8 **PIV characterization of the global flow for a given experiment.** The vector field provides a representation of the flow, where a vector is associated to a point in space providing the position coordinates U_x and Uy; the green arrows indicate the direction and magnitude of the bacterial flow. From the temporal evolution of these coordinates, given by the time between frames, the velocity field was calculated and the distribution of the velocity in the cluster is shown, from fast movement (red) to slow movement (blue). As we can see on the periphery of the cluster the displacement is higher and a pump-like motion is present. Next, then rotational of the velocity vector is calculated to obtained the vorticity field. Form the later we can get a description of the local spinning motion at some point in the flow of bacteria.

Next, the global bacterial flows were quantified by the in-plane kinetic energy $E_{xy}(t)$ and enstrophy $\Omega_z(t)$ defined as [51]:

$$E_{xy}(t) = \langle \frac{v_x^2 + v_y^2}{2} \rangle, \tag{3.7}$$

$$\Omega_z(t) = \langle \frac{\omega_z^2}{2} \rangle, \tag{3.8}$$

where $\omega_z = \partial_x v_y - \partial_y v_x$ y the vertical component of vorticity and $\langle \cdot \rangle$ is spatial average.

3.7.4 Viability essays

There are different methods to determine the number of micro-organisms that are present in a given population. This can be accomplished by using the spectrophotometer to measure the optical density of the population [167], by directly counting the microorganisms using a haemocytometer [61], or by serial diluting the bacteria and plating on media that supports the

growth of the microorganisms [61]. The latter method is somewhat more time consuming, but provides statistically accurate and repeatable results. This method is also the ideal method for enumerating microorganisms in a given population because it only identifies the living organisms in that population.

After the confinement of bacteria cells we used serial dilutions, plating and counting the number of colony forming units (CFU's) to determine the number of bacteria present in our cavity and their viability. In other words, we checked if the interaction with acoustic waves damages the cell, either by disrupting its membrane or producing a side effect due to the environmental stress.

To this end, the treated cells were recollected and saved in an 1 ml Eppendorf tube, this suspension contains an unknown number of bacteria. The same was done for the control resonator which contains cells that were not exposed to the acoustic wave. The collected volume contains n_0 colony forming units (CFU). Before we started diluting, we prepared k_1^i dilution blanks, which are Eppendorf tubes containing α ml of the diluting liquid. The first step is to gently shake or swirl the tube containing the recollected cells. This will ensure that the cells are evenly distributed because if the cells settle to the bottom, the number of cells that we get via pipetting is not enough invalidating the final count. Once swirled 100 μl of the collected inoculum were added to 900μl of diluting liquid in the next tube k_2. This is a 1 in 10 dilution, this step is repeated up to k_i where i is the total number of dilutions.

Later, after swirling all the Eppendorf tubes, we took a fraction $\beta = 100\mu$l of the total volume (1 ml) and spread it on agar plates– this means that only 10% of the volume is plated. Triplicates of each plate were made and they were incubated at 30° overnight. Finally, the UFC's were counted as shown in figure3.9.

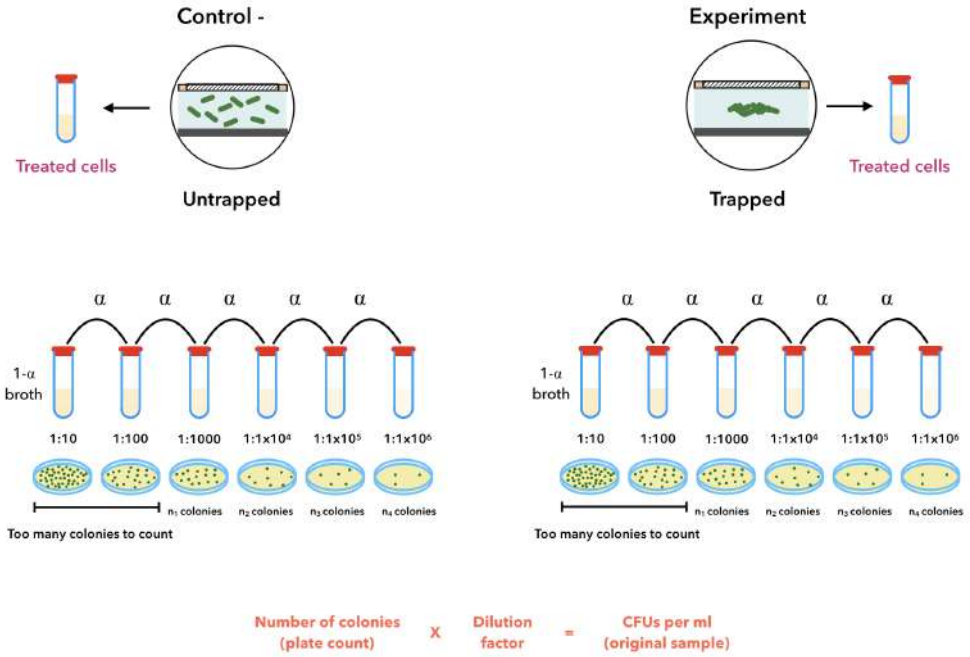

Fig. 3.9 The serial dilution method is employed to estimate the concentration of bacteria by counting the number of colonies cultured from the dilutions of the inoculum and then back tracked the measured counts to the initial concentration. In this work, for every experiment we use an inoculated resonator-same geometry and inoculated protocol- that is not exposed to ultrasonic waves as a negative control and a resonator where the cells are exposed to acoustic waves as the experiment. In the experiment resonator the bacterial cells are trapped, following the protocol described earlier, and after the acoustic input is turned off, the incoculum is pipetted from the cavity and placed in an Eppendorf tube (Treated cells tube in the figure). The collected volume contains n_0 colony forming units (CFU), later a series of k dilutions are made sequentially each with a dilution factor α. From each of the k dilutions a fraction β is taken and spread on agar plates where colonies are counted. Let's consider the first tube in the figure (either the control - or the experiment) where the first dilution $\alpha = 10$ indicates a 10-fold dilutions i.e. by diluting 100 μm of the collected inoculum into 900μm of media; and $\beta = 100$ means that only 10% of the volume is plated. In our case we make plating triplicates for each dilution.

3.8 Results

3.8.1 Clustering and spreading

The first set of experiments were performed using *E.coli*RP437-YFP as a model microorganisms.

To study the acoustic trapping of bacteria at the nodal plane the resonators were inoculated. At the beginning of the experiment, before the acoustic input was applied, the bacteria cells were distributed in the entire volume of the cavity, as we can see in the first image of Figure 3.10. At this point bacteria perform their typical reorientation displacement (run and tumble), constantly modifying their swimming trajectories. Afterwards, when the sample was exposed to the acoustic field, that is, the emission plate was excited with a continuous sinusoidal signal at 2 MHZ and 20 U_{pp}, the field promotes the bacteria displacement towards the nodal plane followed by a focusing and confinement of the sample.

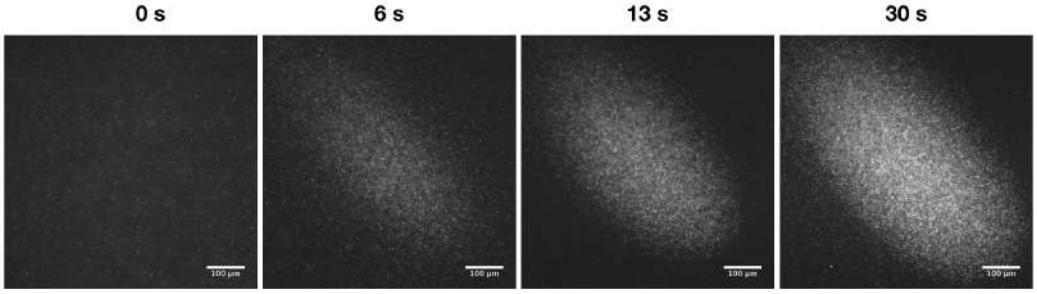

Fig. 3.10 **Bacterial clustering in the acoustic trap.** Photographs of the induced clustering in the acoustic levitation trap. The pictures were taken at different times; the first one corresponding to the free suspension and the following after the acoustic field interacts with the bacterial cells inside the acoustic trap.

As stated before, the bacteria were driven by the radiation force towards the levitation plane, at 185 μm above the surface of the emission plate, in the first seconds after the acoustic input is applied at $t = 30s$. During this process, the fluid is dragged and a back flow is immediately established in the cavity, triggering an advective flow that enables the competition between the bacteria activity and the transversal and axial components of the acoustic radiation force as portrayed in Supplementary Movie 1 [67]. This generated a perturbation in the initial concentration profile similar to the perturbation observed in a system of highly active colloids [169]. Thereafter, bacteria got close to each other prompting cell to cell interactions inside spherical or spheroidal clusters that take approximately two and a half minutes to consolidate

(see figure 3.11).

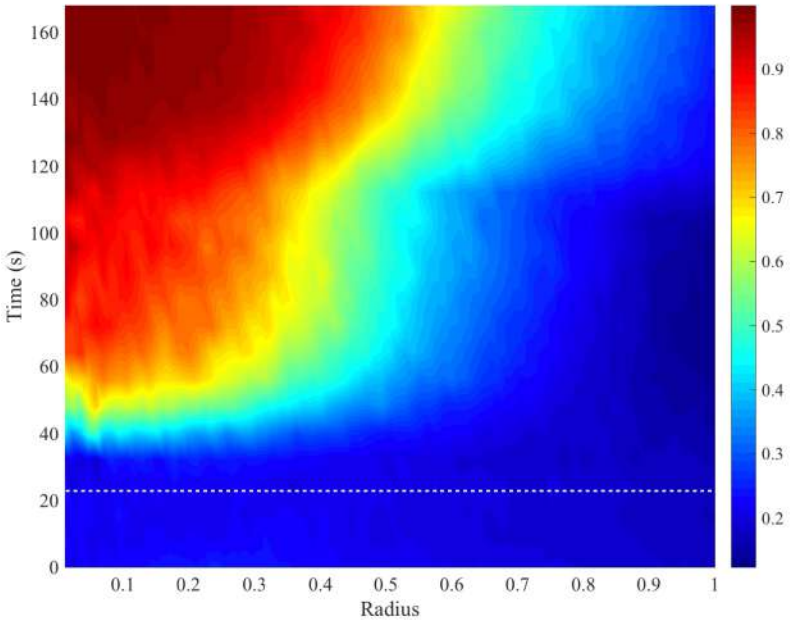

Fig. 3.11 **Spatiotemporal distribution of the area fraction in the clustering process.** The bacterial concentration increases in the centre of the region once the acoustic trapping begins (indicated by the white dotted line). It takes 20 s to form a highly dense aggregate from an initial homogeneous distribution. When the cluster is stable, in other words, when there is no input of bacteria towards the center, we can distinguish three regions. As we can see in the image: the red region with the highest concentration, the yellow-blue part with an intermediate concentration, and the dark blue with a gas-like phase, where bacteria cells are still free to move in their run and tumble fashion. The color bar (from blue to red) depicts the increasing values of area fraction.

As soon as the acoustic forces were removed, the bacteria were free to escape. In other words, the withdrawing of the acoustic forces liberated bacteria and spreading occurred. In Supplementary Movie 2 [67], we showed how the highly concentrated cluster expands after a swarming-like motion is taking place in the cluster interior and a dilution of the cluster took place, leaving bacteria in and out of focus. This means that the levitating bacteria community diffused either horizontally or out of plane towards the walls of the resonator.

The quantification of spreading dynamics as a function of time is portrayed in figure 3.12. The division of the entire cluster in thin rings, as described in the methods sections, allowed us to follow the dynamics at different radii of the spreading process, clearly observing a

transient marked by the inflow and outflow ring by ring. This behaviour persists for all the cluster we analyzed, although the transient reduces when the cluster are more circular.

To describe the spreading kinetics of the bacteria cluster in each ring we denoted C as the concentration within a given area and time. The initial value C_0 corresponds to the bacteria being acoustically trapped at a time $t_0 = 0$ and a final concentration C_f when bacteria are fully dispersed in the complete area at $t_f = \infty$. The spreading is assumed to be a first order process with a rate proportional to $C - C_f$:

$$\frac{dC}{dt} = -k(C - C_f), \tag{3.9}$$

and its solution:

$$C = (C_0 - C_f)e^{-kt} + C_f. \tag{3.10}$$

The solution shows that C reduces exponentially with time. Firstly, we noticed that all curves converged at C_f, indicating that bacteria spread homogeneously. Secondly, for the last five rings $C_0 - C_f$ is negative, meaning that the rings have empty segments due to the elliptical shape of the cluster. We can also see that it takes less than 5 s for these rings to be replenished by bacteria from the inside. Thereafter, the decay is exponential.

The values of k, which are plotted in the inset of Figure 3.12, clearly revealed three decaying behaviours: constant with a fast decaying rate **(F)**, concavely decreasing with a medium rate **(M)** and convexly decreasing with a slower rate **(S)**. The average values for these regions are 0.3, 0.2, and 0.1 s^{-1}, respectively, we estimated the characteristic spreading speeds, $s = qk$ (the product of the ring thickness and decaying rates) to be 1.2, 0.78 and 0.39 μm/s.

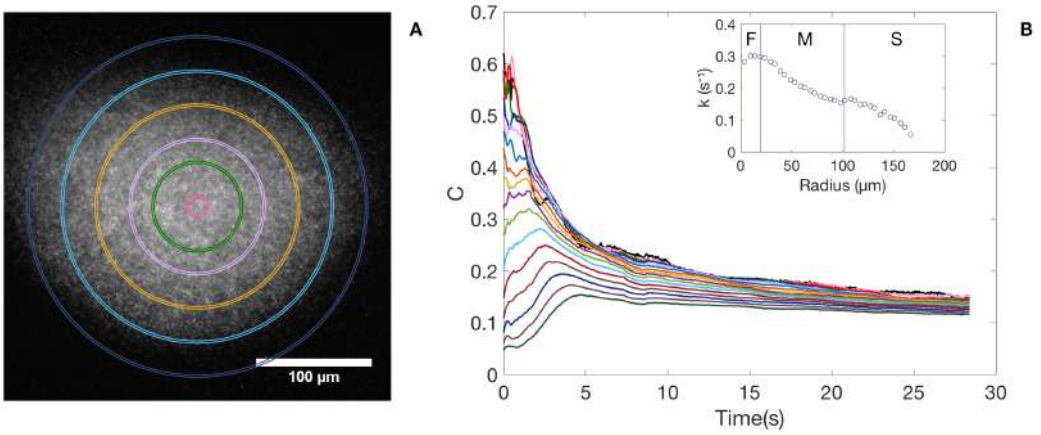

Fig. 3.12 **Bacteria concentration decays as a function of r. A.**The bacterial cluster is divided in 16 concentric rings of thickness q (for clarity, only 5 are shown). In each one of them we estimated the bacteria concentration in terms of the intensity in grey scale normalised by the area of the ring. **B.** The concentration as a function of time. Top-to-bottom curves correspond to inner-to-outer rings. Note that the decays are exponential, where in the inner rings the decaying is faster. Indeed, the decays at the external zones of the bacteria cluster are almost constant. In the inset the decay constant for each ring as a function of the ring radius. We see three different behaviours with fast, medium and slow decaying rates.

After we analysed the experiments performed with this *E.coli* strain we realised that there are some biological shortcoming that we did not considerate previously. For example, our microbiological protocol was not robust enough to provide motile cells all the time so a lot of experiments needed to be discharged. Later we found that the reason for this is that non-motile variants arise if the cells are not culture on soft agar. The improved protocol, to keep working with this cells, was more tedious and also, there was not a standardization or enough background information of the cell construct.

In order to save time and facilitate the handling of microorganisms we decided to change the model strain. From now on, all the experiments were performed using the Jovanovic strains, all the results henceforth presented are the ones obtained for this bacteria.

The inoculation of the resonator was performed following the established protocol. The resonator was placed on the microscope stage, the best driving frequency at 20 U_{pp} was found, normally 4.6 MHz. These actions were done for resonators inoculated with motile or non-motile cells, the clustering and spreading processes were recorded and analyzed. Let's remember that due to the energy distribution we might encounter cluster with diverse sizes

and shapes, of course this has an impact in the clustering and spreading dynamics. In Figure we can see the contrasting examples of the clusters obtained for both Jovanovic-GFP motile+ and Jovanovic-GFP non-motile.

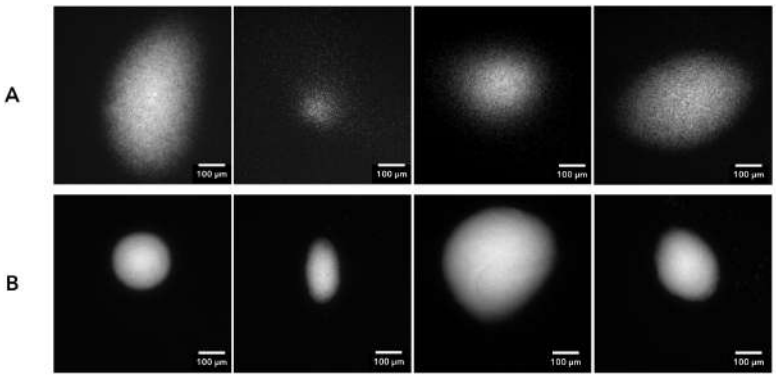

Fig. 3.13 **Contrasting examples of the cluster size A.** Clusters obtained in one experiment using Jovanovic-GFP.motile+ cells with a driving frequency of 4.6 MHz and 20 U_{pp}.**B.** Selected cluster of the 14 obtained cluster obtained from trapping Jovanovic-GFP.Δ$fliER$ cells with a 4.6 MHz driving frequency and 20 U_{pp}.

The analysis of the clustering process yielded similar results for the Jovanovic-GFP motile+ and Jovanovic-GFP Δ$fliER$ strains to the ones obtained with *E.coli*-RP437 (data not shown).

On the other hand, the spreading process was different between both strains. As we can see, from the three representative experiments in figure 3.14, the spreading of non-motile bacteria shows that once the acoustic input is withdrawn (white line) the cells conforming the cluster did not disperse. The size of the aggregate, determined by the region occupied by the cells (x-axis) and the intensity distribution on the heat-map, did not increase significantly rather the size was maintained throughout the spreading time. The spreading time is consider as the times it takes the cells to totally disperse on the cavity or the out-of focusing of the cluster; the latter implies that the consolidated cluster sedimented due to gravity.

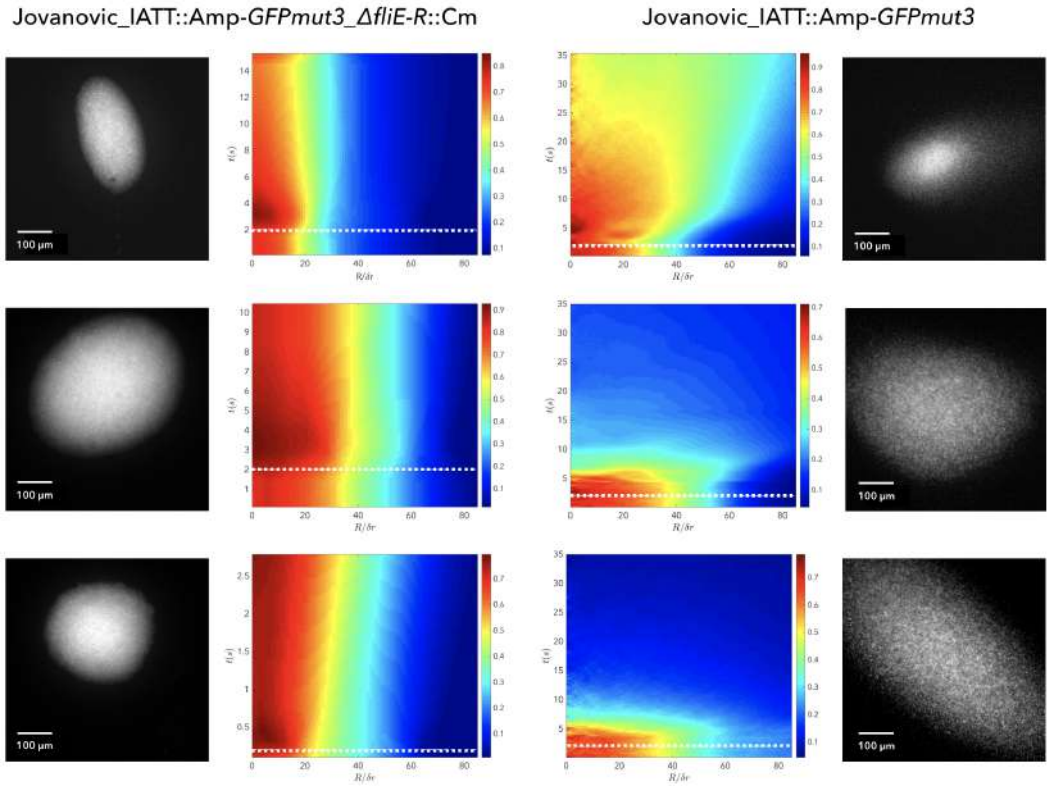

Fig. 3.14 **Spreading processes of non-motile and motile strains** On the first two columns (left) images and heat-maps of 3 cluster of Jovanovic-GFP.non-motile. As seen here, the cluster do not spread but rather maintains it size, whereas the spreading of cluster formed with Jovanovic-GFP.motile cells disperse after the acoustic input is remove (dotted white line.). This phenomenon is conserved for all the cluster no matter the size.

3.8.2 Self-sustained turbulent structure of levitating cluster

After we performed the trapping experiments, with motile and later with non-motile bacteria, we realized that within the clusters a swarm-like or turbulent flow emerged. At the beginning we took it as control of the consolidation of clusters in a high energetic spot; since we realized that the phenomenon only emerged when the cluster was well-packed and this only occurs when the acoustic pressure is high enough to counter-act the swimming pressure. More importantly, we realized that the chaotic flows only emerged within the cluster of motile bacteria, in the cluster of non-motile bacteria no displacement of the cells took place.

From this we can get that the emergent dynamics is not due to acoustic streaming that is present in our cavity, due to the interaction of the acoustic waves and the fluid, but rather, is mediated by bacteria self-propulsion. We decided to focused on characterizing the flow dynamics within motile bacteria cluster.

As discussed before, PIV is the classical technique with well-standardized protocols to characterize flows dynamics. On the methods section we already discuss the specific of this technique and explained why we decided to use a suspension composed of fluorescent (30%) and non-fluorescent (70%) motile bacteria.

The selected acoustic (the fixed distance model) resonator was inoculated. Later, following the established protocol to study the effect of confinement strength variations on the mean kinetic energy of the global flow videos showing the temporal evolution were acquired.

For each experiment, the video images, obtained from the videos, were processed to enhance their contrast by a 0.3 % (see Figure 3.15). Later, a time-resolved analysis of the series of image pairs were analyzed in a $1-2, 2-3, 3-4$... manner. To do so, the cross-correlation we used was the direct Fourier transform correlation (FFT), as it delivers the more accurate results because the data is analysed in several steps. For the first analysis, the interrogation window was 64 pixels with a 32 pixels step and for the second pass 32 pixels and 16 pixels.

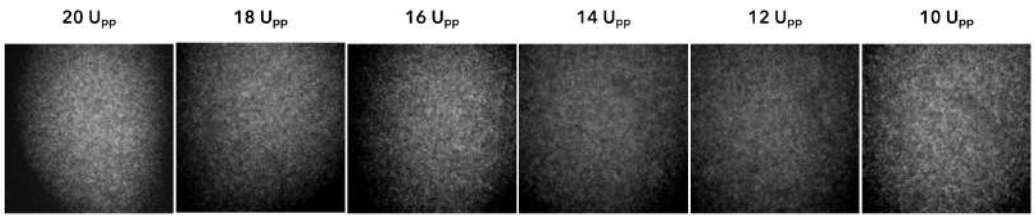

Fig. 3.15 **Decrease of the strength of confinement modifies the distribution of cells.** The sequence of images correspond to one experiment that shows how the cells within the cluster re-distribute once the strength of E_{ac} related to the applied voltage U_{pp} reduces.

The PIV analysis gave us the vector map of the bacteria flow with the U_x and U_y vector position. From the vector position and the time between frames the velocity and vorticity fields were derived for all the experiments as shown in Figure 3.8.

Later, adopting standard statistical measures from classical turbulence analysis, global bacterial flow properties were quantified by the in-plane kinetic energy $\langle E_{xy} \rangle$ using equation 2.6 and the in-plane enstrophy Ω_z using equation 2.7.

Figure 3.16 depicts an example of the data derived for the global flow from a cluster formed using strong confinement (20 U_{pp}). While the global kinetic energy and the global enstrophy fluctuate, their time averages $\langle E_{xy} \rangle$ and Ω_z are approximately constant during the 50 s time used in the data analysis. Figure 3.16 only shows the first 7 seconds of the acquired data. Finally a fast Fourier transform (fft) is applied to access more information from the signal.

To analyze the changes in the global bacteria flow properties as a function of the strength of confinement; a cluster confined with the strongest trap, which in our configuration is an input of 20 Upp, was later release in a control manner. The magnitude of the acoustic constrains was reduced with a 2 U_{pp} step from 20 U_{pp} to 10 U_{pp}.

A one minute and a half video was acquired for each magnitude. The videos were characterized as described on the previous paragraphs. The mean kinetic energy $\langle E_{xy} \rangle$ was plotted versus the confinement strength that is related to the applied voltage and the acoustic energy E_{ac}. We found out that for all our experiments, no matter the initial size of the cluster, $\langle E_{xy} \rangle$ does not change significantly when the strength of the trapping decreases and the same behaviour was found for the in-plane enstrophy Ω_z .
Once the experiment was finished we performed a viability assays to study if the cell were still alive or if somehow the ultrasonic waves had an impact on them.

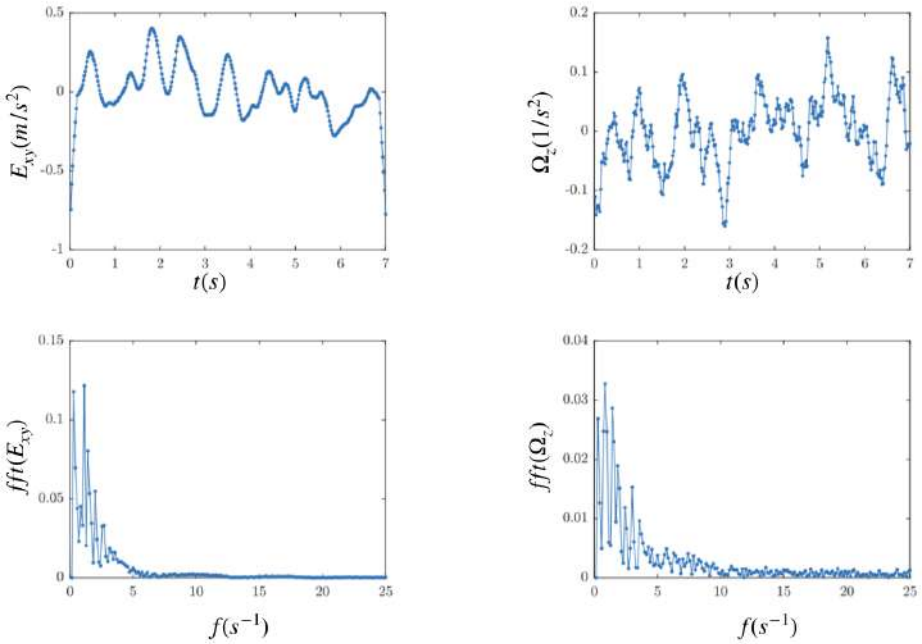

Fig. 3.16 **Kinetic energy and enstrophy for strong confinement** U_{pp} Mean kinetic energy and enstrophy of the in-plane bacterial flow components show moderate fluctuations during the data acquisition period. On the bottom the FFT for each signal.

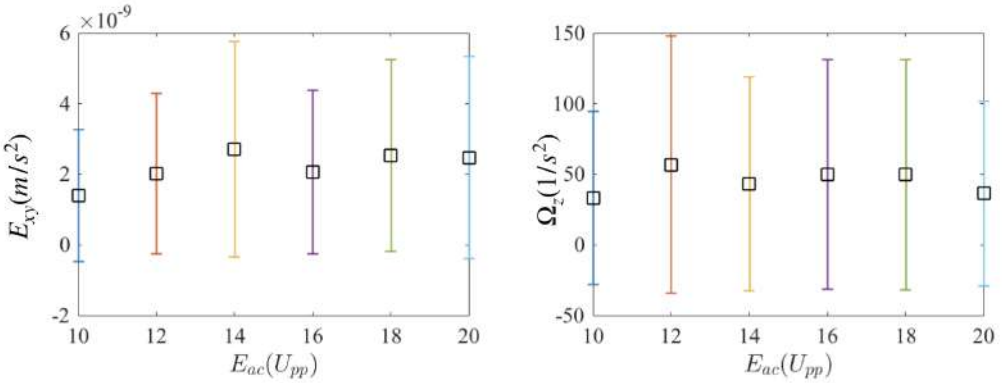

Fig. 3.17 $\langle E_{xy} \rangle$ **and** Ω_z**(t) as a function of** E_{ac}**.**

3.8.3 Viability assays

The cells form the control resonator and the resonator where the cells were trapped were recollected and their viability assessed.

3.8.4 Discussion

The use of the acoustic trapping technique provided acoustic forces with magnitudes in the order of piconewtons (pN). The forces enable the redistribution of the cells in the cavity of the resonator. The motile and non-motile cells can be manipulated in a contac-less manner, when the acoustic field is activated, the local density suddenly increases at energetic hot spots in the nodal plane, triggering the emergence of thin disk-shaped clusters, restricting their degrees of freedom.

We observed that within the levitating cluster, bacterial turbulence arose. The dynamics of the levitating bacteria resembles a self-assembled pump-like structure, comparable to the structure predicted by Nash et al. [120] in their simulations using a lattice Boltzmann in harmonic traps, where they associate the origin of the instabilities to a symmetry-breaking swarm of swimmers.

The analysis of the global kinetic energy as a function of the applied voltage shows us that E_{xy} does not change significantly. This might be due to the fact that bacteria can still divide under acoustic trapping. Therefore even when the confinement is less strong the density of the of the cluster is the same at the same spot and the mean kinetic energy remains unchanged.
The viability assays reinforce this theory as they proved that trapped and untrapped plate counts are within close range of each other. Implying that cells do not die in measurable amounts, due to acoustic trapping for 20 min.

Chapter 4

On the feasibility of enhancing biofilm development using acoustic forces

The discovery of biofilms dates back to the late 1600s [156], and since then, a myriad of research has been done to tackle the conundrum biofilm development is. It is widely acknowledged that the planktonic mode of growth does not provide a sufficient picture of bacteria in natural settings but rather an incomplete one [80]. Bacteria, as the social microorganisms they are, tend to live in complex multicellular communities known as biofilms.
A biofilm is an assemblage of irreversibly surface-associated microbial cells enclosed in an extracellular polymeric substance matrix [80, 39, 57]. Biofilm-associated microorganisms differ from their planktonic counterparts; for example, the genes that are transcribed are different [46, 80, 39].

Biofilms are eclectic communities, their composition depends on the environment they inhabit; water systems biofilms may contain corrosion products, clay material and freshwater diatoms [145], unlike medical devices-biofilms that normally contain coccoid organisms and EPS [46, 39, 42], or aquatic biofilms (air-water interface) [118] that also differ greatly.
The accepted model of *in-vitro* biofilm development addresses the attachment of single planktonic bacteria cells to surfaces and the subsequent maturation into a multi-cellular three-dimensional structure [46, 130]. In real-life scenarios, such as ecological niches and infections, cells clump as multicellular aggregates and later can be attracted to surfaces. These aggregates can also be found when they slough off from a surface-attached biofilm, drift away and re-colonize a new surface [189, 98].

An excellent example of aggregates that arise from a surface-attached biofilm, and that is also considered a new kind, are biofilm streamers, also known as "free floating biofilms". Biofilm

streamers can appear in environments where a flow is present, like rivers or tubing. Under these conditions, the flow-induced shedding of extracellular matrix from the surface-attached biofilm generates a sieve-like network that captures cells and other biomass. It has been demonstrated that they affect the flow through porous materials [49]. In addition, free-floating aggregates have a profound effect on surface-attached biofilm development, out-competing the biofilm population arising from single cells attachment [98].

In the previous examples, a seeding process takes place in the surface prior to streamers formation or the dispersion of biofilm-chunks; in the open sea, or any other air-water interface system, the seeding begins around a dust particle where bacteria cells nucleate leading to another kind of free-floating biofilm.

In general, most systems that are utilized to study biofilms are either based on the surface attached growth of microbes under shear stress, the embedded growth of bacteria in a microfluidic agarose channel [88] or the recollection of biofilms produced in the air-water interface [78] of a flask in a rotary shaker. While these standard assays have enabled the identification of several genes involved in biofilm development, the importance of the geometry and topology of the surface [25] and the long-distance electrostatic communication between bacteria [140, 110]; sometimes, biofilms form under very different conditions than the ones provided by these traditional techniques. A way to better understand this natural phenomenon is to develop a new model where neither shear-stress nor physical seeding points are needed.

In this chapter, we discuss the possibility of using acoustic radiation forces to promote the development of free-floating biofilms without a surface-attached biofilm or a dust particle as precursors. Instead, as shown in the previous chapters, the primary and secondary radiation forces increase the local density of bacteria cells at the energy hot-spots distributed on the acoustic resonator surface and a new-brand free floating aggregate arise. Under this configuration, acoustic forces counter-act the effect of gravity and the energy hot-spots determine the virtual nucleation points.

4.1 *Escherichia coli* biofilms

In biofilm research the most studied microorganism is probably the opportunistic pathogen *Pseudomona aeruginosa* [10]. Nevertheless, most of the genetic analysis in biofilms has been performed with *Escherichia coli* as the model microorganism, due to the fact that it can be handled in the laboratory with relative ease and its genetic background is well characterized. In addition to the harmless *E.coli* serotypes, many pathogenic strains can cause severe infections related to biofilm formation and antibiotic resistance. Therefore, its study and understanding is important to prevent biofilm-related casualties and to find new strategies to combat infections.

Biofilm formation of *Escherichia coli*, and other self-propelled bacteria, on a surface involves several stages (see Figure 3.1):

Primary adhesion to surfaces: reversible attachment

The bacteria adhesion to abiotic surfaces is highly dependent on physicochemical and electrostatic interactions between the bacteria envelope and the substrate, usually conditioned by the fluids to which the surface is exposed [14]. The repulsive or attractive forces lead to reversible attachment of bacteria to the surface, with most of them leaving the surface to join the planktonic-phase community, either due to the shear stress or their own propulsion. Ionic forces of the media and temperature also play an important role in this first step towards biofilm development. Recently, it has been shown that the topology and wettability of the surface also impacts the first attachment, where rugosity increases surface adhesion and hydrophobic surfaces are more likely to be colonized than hydrophilic ones [46, 25].

Irreversible attachment

The main developmental step in biofilm formation is the transition from a planktonic, often motile, to a sessile phenotype. Planktonic cells attach to the surface, where the adhesive organelles of the fimbriae family contribute highly to its irreversible attachment [10]İn particular, three have a role in strengthening the bacteria-to-surface interaction: type 1 fimbriae, curli, and conjugative pili.

i. Type 1 fimbriae or pili

Pili is a filamentous proteinaceous adhesin with tubular structure (5 nm x 2 μm) that can adhere to a variety of receptors molecules on eukaryotic cell surfaces. The presence of pilis is critical for biofilm formation in *E. coli* as it impacts the initial attachment to the surfaces and also can modify the composition of the outer membrane [10].

ii. Curli fimbriae or aggregative fimbriae

Curli aggregates at the proteins of the cell surface such as fibronectin, laminin and plasminogen, to form 6 nm diameter structures with 1μm lengths promoting the adhesion of bacteria to different cells. In addition, curli facilitates initial cell-surface interactions and subsequently cell-cell interactions impacting deeply in biofilm development. [175, 34, 10]

iii. Conjugative pili

The conjugative pili promote both initial adhesion and biofilm maturation stabilizing the structure of the latter [10].

Microcolonies proliferation

Later, attached cells aggregate into microcolonies, that are held together by a matrix which includes proteinaceous curli fibres and exopolysaccharides (EPS) like PGA and colanic acid. At this moment, inter-bacterial adhesion rather than direct contact with the surface leads to progressive build up of the mature biofilm.

Mature biofilm

Biofilm maturation corresponds to the three-dimensional growth of the biofilm that occurs after initial attachment to the surface. Mostly due to bacterium-bacterium interactions, this process leads to the formation of a heterogeneous physicochemical environment in which biofilm bacteria display characteristic physiological traits that distinguish them from their planktonic counterparts [10]. A general feature of mature biofilms is their highly heterogeneous architecture that partitions the microbial city into sectors with specific microenvironments.

Dispersal

After maturation, the dispersion step is very important for the biofilm life cycle. Individual cells or small aggregates disperse because of myriads of factors, such as the lack of nutrients, intense competition, outgrown population, among others. These biofilms chunks will detach, drift away to colonize a new surface.

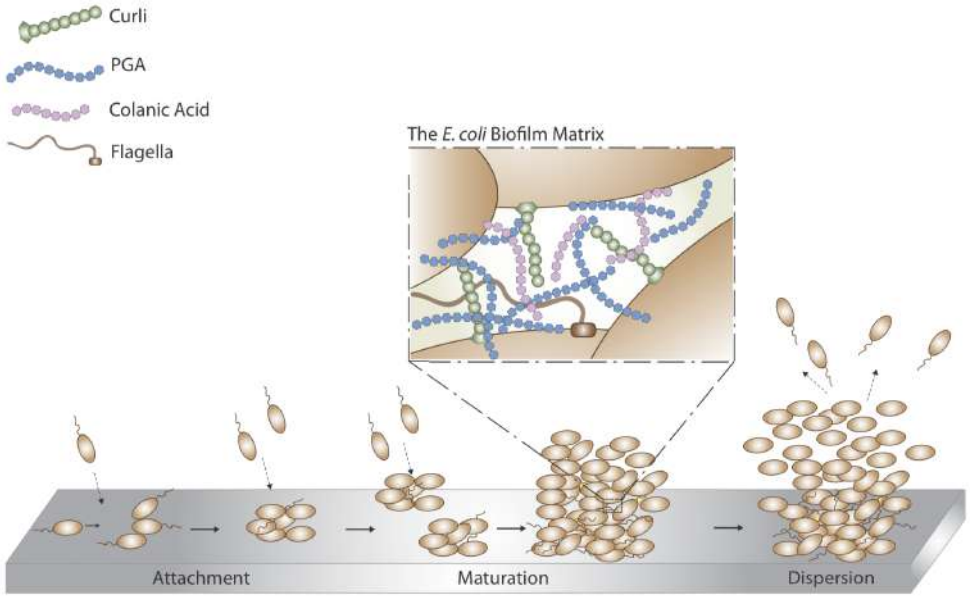

Fig. 4.1 **The phases of biofilm formation in *Escherichia coli***. Biofilm formation involves the attachment of planktonic cells at the surface (irreversible attachment phase), where cells aggregate and bacteria-surface interaction is strengthened by diverse adhesive organelles of the fimbriae family. Inter-bacterial adhesion leads to a progressive built of microcolonies and the excretion of extracellular polymeric substances (EPS) begins. Microcolonies mature into a biofilm where cells form multi-layered clusters. Three-dimensional growth and further maturation of the biofilm provides protection against host defence mechanisms and antibiotics. Later, the biofilm reaches a critical mass and planktonic bacteria living on its surface disperse to the surrounding areas ready to colonize other surfaces [164].

4.1.1 Motility and its impact on biofilm development

Biofilms are usually considered as the immobile state of bacterial growth. Typically, biofilm-forming cells transition from a motile state to a non-motile one regulating their motility. *Escherichia coli* motility is mediated by flagella that propel the cells forward in aqueous environments where cells swim [85] and on surfaces where they swarm [89]. The key player

in motility's regulation is the second-messenger c-di-GMP, which controls negatively flagellar motility via motor curbing. Furthermore, it is a positive regulator of biofilm matrix production required for biofilm maturation, this means that reduces flagellar motility and increases the production of EPS [114, 138, 86, 77, 146].

There is evidence that shows that interfering with motility and its regulation results in changes in biofilm formation in several bacteria species [131, 139, 95, 187, 121]. Indeed, some *E.coli* strains with impaired motility exhibit reduced surface attachment and fail to develop biofilms, but even when this proves the importance of motility on biofilm development in multiple ways some non-motile strains are able to develop biofilms [164, 187, 121]. Biofilm development is a phenotype and strain-dependent phenomenon that is not yet completely understood.

4.1.2 Models for exploring bacteria microenviroments

The development of simplified models to study how bacteria, including pathogens, can form biofilms started right after the demonstration of a link between sessile communities and human infections. This was proven by the pioneer studies by A.T. Henrici [79] in the early 20th century and later by J. W. Costerton [38, 62] both works pointed to the existence of microorganism populations living on surfaces. Multiple in vitro models have emerged from scientists' creativity, each of them especially adapted to observe biofilm formation of specific bacteria and within specific environments [104].

In vitro biofilm models

A complete and comprehensive list of in vitro biofilms models is provided in the very detail by Lebeaux [104]. In a few words, in vitro biofilm models can be classified in three distinct groups:

1. Closed or static models

These type of model corresponds to the one in which there are limited nutrients and aeration. This includes some of the most popular and successful models, such as the colony biofilm model and microtiter plates. In addition, these models enable direct rapid quantification of biofilm mass (see Figure 4.2A) [32, 115].

2. Open models.

The principle of these models is similar to continuous cultures, in which spent culture consisting of wastes, metabolic byproducts, dispersed and dead cells are constantly replaced by fresh medium. These methods generally allow the control of environmental parameters such as shear forces, and have been therefore extensively used to study the physical and chemical resistance of biofilms as in Figure 4.2B [115].

3. Microcosms

Microcosms are the most sophisticated models, which aim to closely mimic in situ conditions. They often include several bacterial species and use material from the studied environment, for instance, addition of hydroxyapatite and saliva to model dental biofilms [148], or covering abiotic surfaces with human cells in order to mimic an in vivo situation [15].

***Ex vivo* biofilm models.**

Midway between *in vitro* and *in vivo* lie ex vivo models, in which tissues or organs are extracted from an organism (typically porcine or murine) and placed in an artificial environment for further analysis and experimentation. They can be particularly useful to image or analyze the progression of bacterial colonization of a given organ or tissue, such as tracheal epithelium, vaginal mucosa, kidneys or teeth [104].

***In vivo* biofilm models.**

Infection and pathogenesis result from a continuous interplay between the host and microbes and between microbes themselves influencing and determining the fate of infection. The complex dynamics makes difficult the use of *in vitro* models. To overcome this, non-mammalian models like the fruit fly, *Drosophila melanogaster*, or the zebrafish *Danio rerio*, have been adapted to study host-microbe interactions and immune system responses. There are also, models where tissue can be present to make the model more realistic [104].

All the methodologies described earlier to study bacteria microenviroments, such as biofilms, have been proven to be quite effective to evaluate physical, chemical and genetic properties of biofilms. Also, they provide a robust technique to evaluate new drugs against persistent and resistant bacteria associated with biofilms and therefore related to some major diseases.

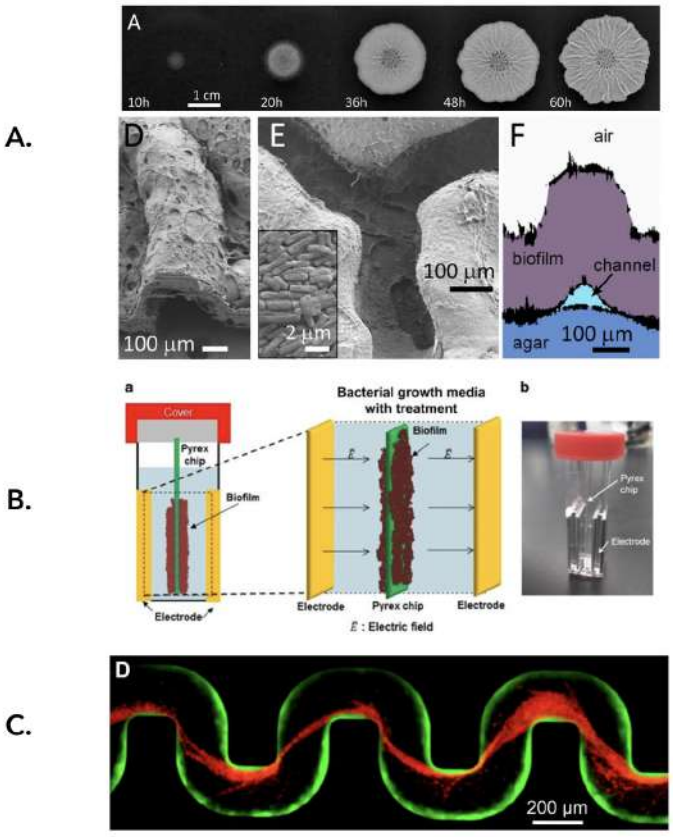

Fig. 4.2 ***In vitro*** **microenviroments to study biofilm development**. **A.** Closed model; agar plates are the most popular technique to evaluate biofilm development. The picture shows a *Bacillus subtilis* biofilm growing on the surface of an agar gel containing water and nutrients. The biofilm increases in height to hundreds of micrometers, spreads to reach a diameter of several centimeters, and forms macroscopic wrinkles.This techniques allowed the characterization of channels within the biofilm [184]. **B.**Schematic of a static model. Glass chips/coupons placed inside electroporation cuvettes were *E.coli* biofilms develop. This technique was used to evaluate the electrical energy to treat biofilms using a bio-electric effect [93]. **C.** A clear example of an open model is a microfluidic channel used to evaluate the formation of free-floating biofilms of *P. aureoginosa* [49].

Unfortunately, the production of a mature biofilm using these models takes from some hours to days. Hence, an improvement that can be made to these systems is to reduce the time needed to produce ready-to-evaluate biofilms. Moreover, to have the possibility to asses biofilm development in a efficient and rapid manner.

4.2 Shaping free-floating biofilms using acoustic forces

4.2.1 Model microorganisms

It is well-documented that the self-propulsion of bacteria and the adhesive organelles of the fimbriae family strengthen the attachment and development of biofilm on surfaces [114, 138, 86, 77, 146]. To study the likelihood of enhancing free-floating biofilm development using acoustic forces. Moreover, two motile *Escherichia coli* K-12 MG1655, with constitutive curli production strain were kindly provided by our collaborator from the Génétique des biofilms group at Pasteur Institute.

***Escherichia coli*MG1655_IATT*gfp_ompR234_malA*::Km**

Escherichia coli K-12 strain carrying the mutant ompR234 allele. The mutant OmpR protein activates expression of CsgD, a transcriptional activator of the *csgA* gene,resulting in an increase in CsgA protein levels and promotion of biofilm formation.
This strain typically clumps due to the overexpression of the curli gene.

***Escherichia coli*MG1655_IATTamp*gfp_ompR234_malA*::Km_csgA::aadA7**

Escherichia coli K-12 strain carrying the mutant ompR234 allele with a knockout of *csgA* gene resulting in a phenotype with loss of adherence.
This strain do not clump as it is a *csgA* mutant.
To avoid writing the complete name of the strains we re-name theme as:

***E. coli*(csgA +)**: *E. coli*MG1655_IATT*gfp_ompR234_malA*::Km.

***E. coli*(csgA -)**: *E. coli*MG1655_IATTamp*gfp_ompR234_malA*::Km_csgA::aadA7.

4.2.2 Experimental protocol

Planktonic cultures

E.coli(csgA+) and *E.coli*(csgA-) cells were streaked in LB agar plates with Ampicillin (AMP) and incubated overnight at 30° C. The following day a single isolated colony, of a given strain, was picked from the plate and re-suspended in 5 ml of liquid LB and incubated overnight at 30°C on a rotary shaker at 250 rmp. Fourteen hours later, a fresh culture ($A_{600}0.05$) was re-started and incubated under the same conditions until mid-exponential phase ($A_{600}0.5$). Later the liquid culture was diluted five times ($A_{600}0.1$) –to have the inoculum suspension see figure 4.3A.

Inoculation of the cavity

The acoustic resonator –previously sterilized via ultraviolet germicidal irradiation for 20 minutes–was inoculated with 500 μl of the suspension and sealed with the reflector lid. In parallel, another acoustic resonator, with the same dimensions and also sterile, was inoculated with the same volume, sealed with the lid and placed on the bench, as depicted in figure 4.3B. The second resonator (R_C) is the control to validate the experiments.

Acoustic trapping protocol

Forthwith, the first resonator (R_{Exp}) was placed in the microscope stage and a 30 s video was recorded, as a control of the motility of cells and to measure the velocity distribution of the bacteria cells. Right away, the sample is exposed to a continuous sinusoidal signal, that matches the driving frequency of the transducer at 20 Vpp, and a video of the clustering process was acquired–when possible. Bacteria cells were acoustically confined for 20 minutes –which is the typical time to get a stable aggregate with the Jovanovic strains.

Immediately afterwards, based on the same conditions stated in Chapter 2, a cluster is chosen, and a video to evaluate the dynamics within the cluster is captured. Next, the total area of the cavity is scanned to have a record of all the aggregates that are formed at the nodal plane.The chosen cluster is later freed from the acoustic trap and the release, up to the sedimentation in the surface, is followed up. Once in the surface, its temporal evolution is evaluated for up to one hour. Finally, the distribution of bacteria in the total cavity surface is assessed to be compared to the surface of the control resonator (R_C) (Figure 4.3C).

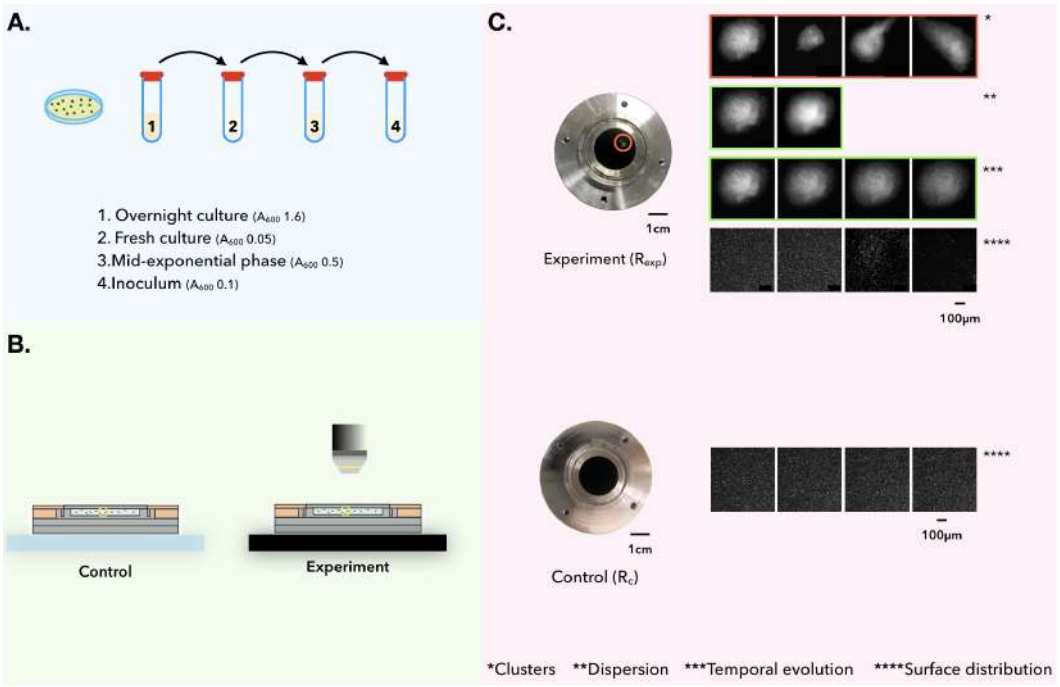

Fig. 4.3 **Experimental protocol to study biofilm formation in levitation. A.** To prepare the inoculum the chosen bacteria strain is streaked in LB agar plates and incubated overnight at 30° C. Afterwards, a single isolated colony is picked and re-suspended in 5ml of liquid LB and incubated overnight in a rotary shaker (30°C and 250 rpm). The following day, a fresh culture is re-started and incubated under the same conditions until it reaches mid-exponential phase. The latter is diluted five times to prepare the suspension to inoculate the cavity of the resonator. **B.** Two resonators are inoculated with 500 μl of the suspension and sealed with the lid holding the reflector. The control is placed on the bench and the other resonator is placed immediately on the stage of the reflected light microscope. **C.** Forthwith, the typical run-and-tumble behaviour of *Escherichia coli* is recorded–this video allows the quantification of the velocity distribution of the cells in the sample. Right away, the sample is exposed to a continuous sinusoidal signal, that matches the best driving frequency of the transducer at 20 Vpp, and a video of the clustering process is acquired–when possible. Bacteria are acoustically confined for 20 minutes and, based on the same conditions stated in Chapter 2, a cluster is chosen and a video to evaluate the dynamics within itself is captured. Next, the total area of the cavity is examined and all the clusters at the nodal plane registered in video. The acoustic input is withdrawn, the sedimentation of the elected cluster is followed up and the temporal evolution of the cluster in the surface as well . To conclude, the distribution of bacteria on the surface of the cavity is compared to the one of the control resonator.

4.3 Methods

4.3.1 Clustering and dispersion

As previously established, bacteria cells inside the inoculated cavity are distributed homogeneously and swim with their standard motion (run-and-tumble), when motile. They move in this manner until the acoustic radiation pressure, from sound waves at ultrasonic frequencies, drags them towards the pressure node of the standing wave created by the interference of the emitted and reflected waves. The cells at the pressure node are also subject to the secondary force (a short-range force) and to the transverse component of the acoustic radiation force –the last two promote the consolidation of the cluster.
It is important to remark that at this point bacteria are not interacting with any surface, rather, they gather in a virtual one. Also, the nucleation points where the clustering takes place are given by the energy hot-zones of the resonator. For these reasons, a free-floating biofilm-like structure, without the necessity of surface attached cells or dust particles to nucleate, is formed at the pressure node.

Once the bacteria cluster is consolidated, typically after 20 minutes unless stated the contrary, the acoustic signal is removed and the bacteria are free to disperse in all the surface or maintained attached if they have a strong bond due to adhesive forces.
To characterize and quantify the dynamics of these phenomenon the radial distribution of mass was calculated following the same protocol as on Chapter 2. We recall that this function is typically used to study the nucleation and aggregation on granular systems [64].

4.3.2 Temporal evolution on the surface

Once the biofilm-like structure settles on the surface of the acoustic cavity the evolution of its area is assessed over time. Time zero, of this temporal evaluation, is considered as the moment when the cluster reaches the surface and it is on focus. A first picture is taken and every five minutes another one, we repeated this process up to one hour. All the pictures are acquired with an Hamamatsu Orca Flash 4.0 camera, fixing both, the exposure time at 1 second and the focal plane. The latter implies that if some part of the cluster becomes out of focus: a vertical growth or a shrinking of the cluster is taking place which leads to a protrusion in the z-plane.

Afterwards, the obtained image sequence is processed using a in-house-made Matlab algorithm, based on the image analysis algorithm already existing in the software. The 8-bit gray

scale images are binarized using the Hung's fuzzy threshold method, as it has been proven robust in the analysis of bacteria isolates on agar plates [18]. The cut-off gray scale value was set at 33, that is, every pixel with and intensity value lower than 33 is considered as background, whilst the pixels with higher intensity are taken as foreground as depicted in Figure 4.4

The area of the binarized cluster was measured and its pixel value transformed into μm^2 using the proper scale. This methodology was used for all the experiments made using all the model strains in this section. Note that the cutoff value was the same for all, unless stated otherwise.

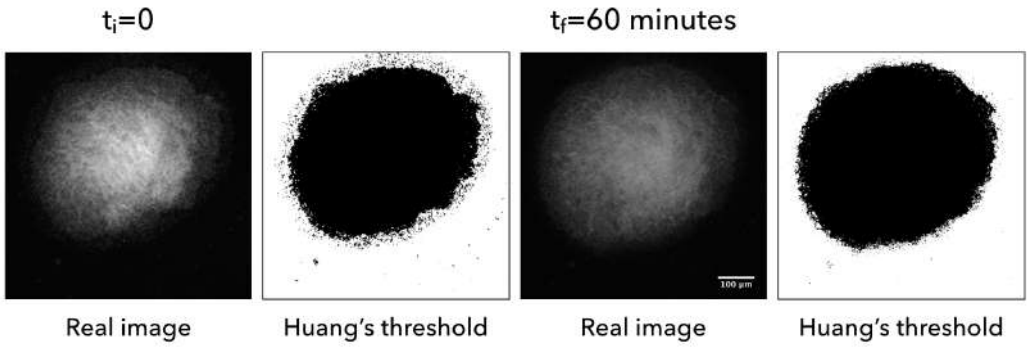

Fig. 4.4 **Estimation of the area temporal evolution using Huang's threshold method**. Every five minutes pictures of the cluster, settled on the surface of the acoustic resonator, were taken using the image acquisition component of the experimental set-up -with a fixed exposure time of 1s . The gray-scale images were binarized using Huang's fuzzy threshold method. The cutoff value is 33, such that every pixel less than 33 is considered as background, while the pixels with a greater intensity value are foreground. The area of the cluster is measured for all the images.

4.3.3 Density distribution on the cavity surface

The bacteria clusters have now settled on the surface of the cavity. In order to have a quantitative idea of the energetic hot-spots where the gathering of bacteria cells took place we analyzed the density distribution, as in intensity of pixels distribution, on the cavity. First, we divided in thirty-six regions the total surface area of the resonator (figure 4.5)–with an area of 3 cm^2 or 5cm^2 depending on the resonator that was used. In each of the regions a picture is taken, with the same camera and exposure time as before. Each image covers an area of $4.48x10^{-3}cm^2$, that is, after the thirty-three zones have been photographed the area that has been cover is approximately 6% of the total surface. This procedure is performed in

the control resonator as well, therefore, seventy-two images are acquired per experiment.

Later, all the images are processed using the Matlab image analysis algorithm. The 8-bit gray scale pictures are binarized using Huang's fuzzy threshold method, with and specific cutoff value depending on the experiment. After this the bacteria-pixels are transformed into white pixels and the background remains black. Afterwards, also with a Matlab algorithm, the number of white pixels, corresponding to bacteria cells, are assessed and the ratio occupied by them per picture is registered.

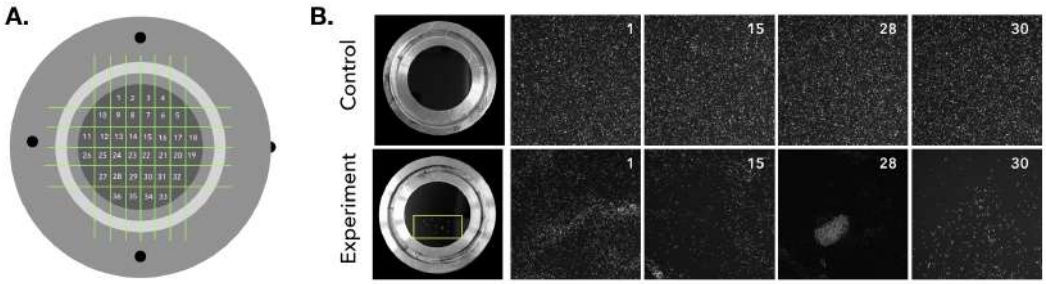

Fig. 4.5 **Density distribution on the cavity surface**. **A.** Schematics of a layered acoustic resonator. The surface-area of the cavity is 3 cm^2, which is divided into 36 regions to ease the mapping of the bacteria cells distribution after the cells are acoustically confined.**B.** For all the experiments two acoustic resonators are used; one as a control, and other to confine the cells. Once the cells are settled on the surface a picture is taken at each of the regions. The area cover per picture is $4.48x10^{-3}cm^2$ (1024 x 1024 px), hence, the mapped 36 regions covered a surface area corresponding to a 6% of the total. Later the distribution of both resonators is compared.

4.3.4 Minimum inhibitory concentration

The aim of the broth dilution method -minimal inhibitory concentration, MIC- is to determine the lowest concentration of the assayed antimicrobial agent that, under defined test conditions, inhibits the visible growth of the bacteria being investigated [180]. In this work, MIC values are used to determine both the susceptibility of *Escherichia coli* to gentamicin (gen) and whereas the clumped cells, due to acoustic forces, present a higher tolerance to the antibiotic.

It is known that one of the main characteristics of the cells in biofilms is the decrease of susceptibility to antibiotics [155], therefore, a difference in MIC values for cells trapped acoustically and not trapped could implicate the formation of free-floating biofilm mediated

via acoustic forces.

To determine the MIC, overnight liquid cultures in LB media were made for each of the strains in Table 1, at 30° and 250 rpm rotatory shaking. A fresh culture was re-started, under the same culture conditions, until mid-exponential phase ($OD_{600nm}0.05$) and later diluted 5000 times to have a suitable sample for inoculation. One 96-well plate was done per strain.

As always, the manipulation of microorganisms was performed in a sterile zone–either in a hood or in the bench using a Bunsen burner to create a sterile zone. Later, a 96-well U-Bottom plate was inoculated with $100\mu l$ from the second to the last column, the first column was inoculated with 180 μl. From the gentamicin stock solution (10X), that was prepared beforehand and stored in the proper temperature, 20 μl were added to the first column of the plate. Using a multichannel pipette, the antibiotic and the cells were mixed gingerly by sucking up-and-down six times.

Afterwards, 100 μl from the first column were transferred to the second one (this is a two-fold dilution for column one), the pipette tips were ejected and with new and sterile pipette tips the wells in column two were carefully mixed. The procedure was repeated down to the 11th column, the volume coming from this column was discarded, i.e. the 100 μl were not added to the 12th column as shown in Figure 4.6. Finally, the plate was incubated overnight at 30°.

Notice that in this protocol the first column is a positive control, where bacteria are treated with the highest dose of antibiotic, and the 12th column is the negative control as bacteria are not treated with antibiotics. This precise method of susceptibility testing allows for quantification of the exact concentration (in µg/mL) of the antibiotic (or client selected test article) needed to inhibit the bacterial growth.

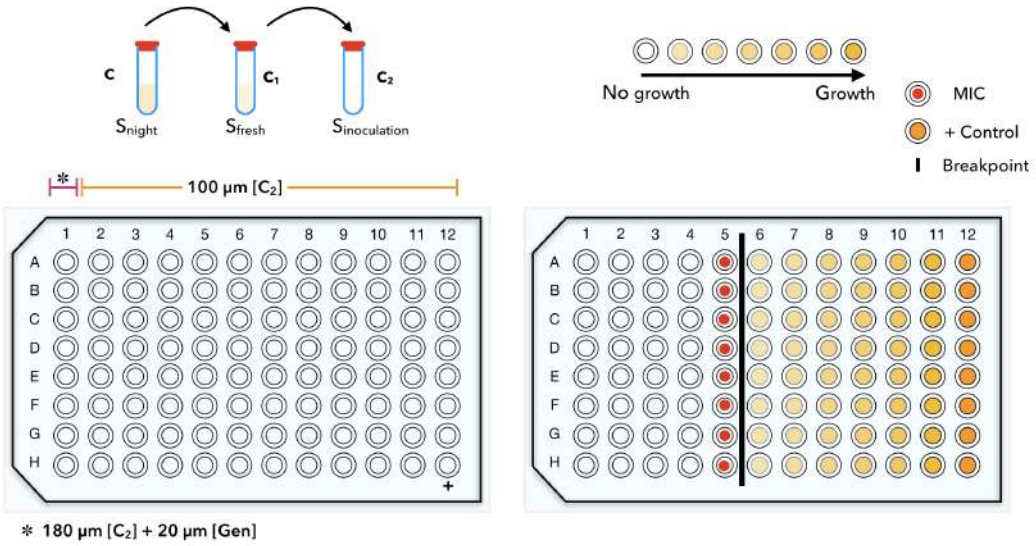

Fig. 4.6 **Minimal Inhibitory Concentration**. MIC testing allows for quantification of the exact antibiotic concentration, in $\mu g/ml$, needed to inhibit bacteria growth. The figure shows a typical 96-well plate, used for MIC assays, divided in twelve columns for micro-dilutions and eight rows normally used for replicates. To test the susceptibility to gentamicine of the strains we used throughout this work, wells 2 to 12 are inoculated with $100\mu l$, whereas the volume for the first well is 180 μl. Next, $20\mu l$ of gentamicine (gen) at 1 mg/ml is deposited in the first well and mixed gingerly. Later $100\mu l$ were transfered into the second well and mixed gently, the transfer procedure to one well to the following was done up to the 11th-the volume coming from this well is discarded. Column 12 serves as a positive control i.e. the cells are not treated with antibiotic. Finally the plate is incubated overnight at 30°. The figure on the right illustrates a plate after incubation, where the white circles represent no bacteria growth, meaning the antibiotic succeeded in inhibiting the bacteria growth for a given concentration. The yellow circles depict bacteria growth -the light shades indicate less growth and the darker shades more growth. The darkest one (column 12) is the positive control that is used to validate the test. The vertical black line represents the breakpoint-concentration at which the bacteria are no longer susceptible to the antimicrobial but become resistant. The red point indicates the MIC value i.e., the lowest concentration at which the bacteria are susceptible to gentamicine.

4.4 Results

4.4.1 Clustering and spreading

The clustering and spreading dynamics differ greatly when compared to the one observed for Jovanovic MG1655 motile bacteria. First, it is important to know that the two model strains used in this section, consider as motile by our collaborators, did not exhibit a run-and-tumble behaviour, rather, they acted as passive particles even when they have flagella. When their motility was analyzed, with a basic 2D-tracking method using Fiji and Matlab, we saw that they are non-motile, as their mean speed is zero. They do, however, exhibit Brownian motion. Their lack of self-propulsion can be explained taking into account that the adhesive organelle, curli, that is over-expressed in CsgA+–the OmpR protein mutant–and not expressed in the knock-out mutant CsgA-, contributes highly to cell-cell and cell-surface interactions [10]. Moreover, curli over-expression impacts on the motility of the cells as discussed in Section 3.1.1.

To better understand the situation, Figure 4.7 shows the cluster formed by the four model bacteria strains used on this thesis, from the stickiest to the least. The phenotype differences between strains also affect the number and size of the aggregates that are obtained after trapping the cells for 20 minutes using acoustic forces, see Figure 4.8.

The stickiest strain, CsgA+, produces on average 22 aggregates per experiment whereas the motile one (Jovanovic motile) only 3. Both CsgA- and Jovanovic$\Delta fliER$ formed 10 aggregates on average. The contrast between the number of aggregates for each strain can be explained by the amount of energy necessary to trap self-propelled cells versus passive, or non motile, cells [23]. It is known that run-and-tumble bacteria can exert an "active pressure" on the walls when in confinement [158]. In our case, the pressure could counteract the effects of the acoustic forces enabling bacteria to escape and no to be easily trapped. Also, as mention before, the acoustic forces can produce a stronger effect on a small cluster with higher surface than over single beads or cells. In the case of the non-motile and the CsgA+ and CsgA- phenotypes, the clumping of cells inevitable therefore producing cluster with bigger surface are than single cells, hence, facilitating their capture at the nodal plane.

The total area occupied by all the clusters, for each experiment, also depends on the phenotype, as the number and size of the cluster depends on the properties mentioned above. For our experiments the clusters of CsgA+ occupied the 0.6% of the total cavity, the clusters formed

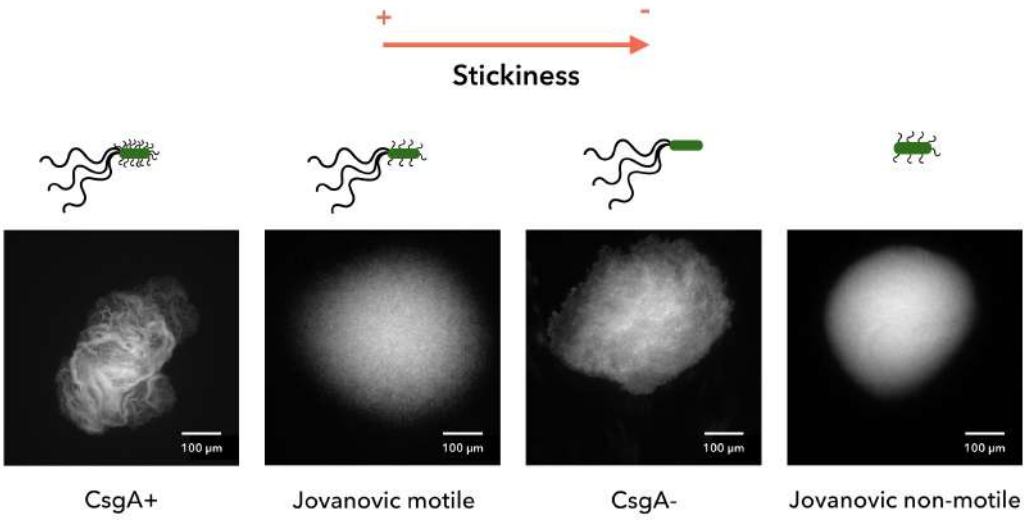

Fig. 4.7 **Cluster obtained with strains with different stickiness.** In-plane micrographs of typical clusters of different strains of bacteria after 20 minutes subject to acoustic confinement. The images are organized from the stickiest strain to the least. The stickiest, UGB 1236 MG1655 (CsgA+), is a motile strain with constitutive curli that over express the curli gene CsgA and as shown exhibits a rough surface. Next, MG1655 Jovanovic (Jovanovic motile) a motile bacteria with constitutive curli expression presents a smooth surface. The third image shows a motile CsgA mutant, UGB2071 MG1655 (CsgA-). This strains does not expresses the curli gene CsgA and shows a compact and not so rough surface when compared with the phenotype over-expressing the curli gene. Finally, the least sticky strain. Jovanovic_Δ*fliE-R* (Jovanovic non-motile) is a de-flagellated strain with curli expression that displays a dense and smoothen surface. Considering that the flagella and curli play a relevant role in surface colonization. In particular, curli, enhances cell-cell adhesion and also, an over-expression of them results in decrease the motility on the cells. The changes in the surfaces roughness can be explained by the presence or absence of curli and flagella in the surface membrane.

by the de-flagellated bacteria the 0.3%, CsgA- clusters 0.2% and the clusters of the motile strain only 0.1%.

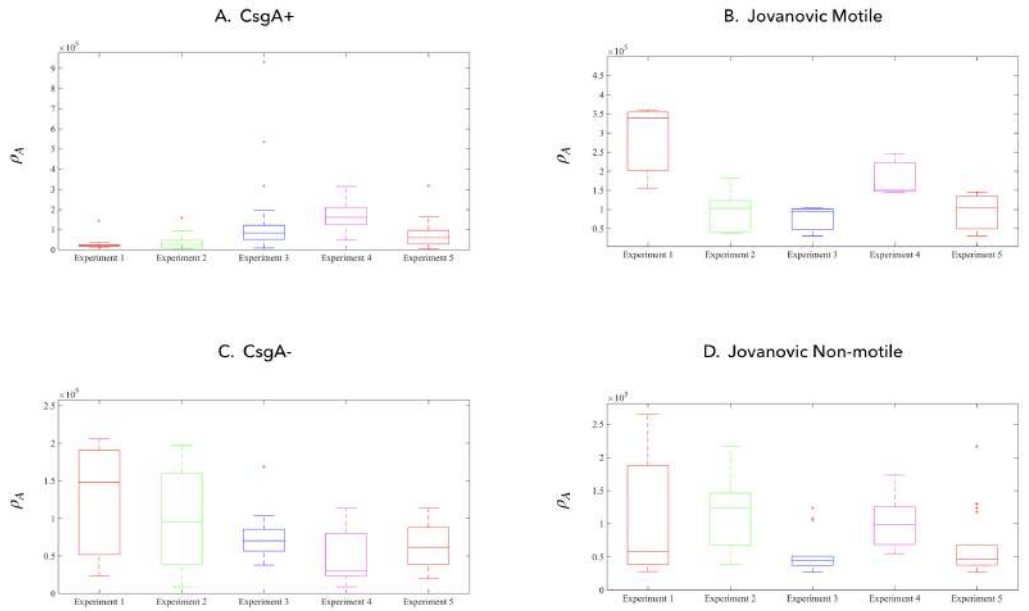

Fig. 4.8 **Measured surface area of the cluster.** Each box represents the distribution of the measured area of the clusters after 20 minutes of trapping. On each box, the central solid line indicates the median of the obtained values, the bottom and top whiskers indicate the 25th and 75th percentiles, respectively.2 **A.** The CsgA+ clusters present a wide size distribution. It is possible to find small clusters a size ranging from 0.5 X10^5 to 1.5 X 10^5 up to big clusters with 9 X 10^5 μm^2. **B.** The narrow size distribution of the clusters with motile cells. The cluster size do not surpass 3.5 X 10^5 μm^2.**C.** The size of the CsgA- clusters lies between 0.3 X10^5 to 2 X10^5 μm^2 as for the Jovanovic$\Delta fliER$ clusters (**D.**).

The recording of the clustering process always represents a challenge, for the reasons explained in Chapter 1, but the clustering for CsgA+ and Csg- was particularly difficult because the gathering of bacteria was carried out mostly by small aggregates instead of single cells. As a consequence, starting the recording from a homogeneous distribution of cells in the cavity was impossible, we always had small aggregates since time zero (see Figure 4.9A-B). Needless to say, this is also a consequence of the phenotype, such is the case of instantaneous clumping due to sticky factors.

On the other hand, the spreading process had a similar dynamics as the one exhibited by non-motile bacteria in Chapter 2, the cells did not diffuse back into the bulk. On the contrary,

they remained entangled and sedimented on the surface of the cavity, see Figure 4.9(C-D).

It is important to note that the bio-turbulence observed within the Jovonovic-motile clusters was not present in those of CsgA+ and CsgA, just as in the case of Jovanovic $\Delta fliER$. This is a reaffirmation of the significant role played by motility on the emergence of this phenomenon.

4.4.2 Temporal evolution on the surface

So far we have shown that CsgA+ and CsgA- strains, even though they have flagella, are not motile as expected. Probably, because the second-messenger c-di-GMP is controlling negatively flagellar motility. Surprisingly, after only 20 minutes of acoustic confinement a cluster that does disperse once released from the acoustic trap, is formed in acoustic levitation. At first sight, it appears to be similar to the one formed by the non-motile strain (Jovanovic $\Delta fliER$). Because the cluster does not disperse we could be dealing with a new type of free-floating biofilm.
Due to the similarity in the apparent behaviour between these three strains (CsgA+, CsgA- and Jovanovic $\Delta fliER$), we evaluated their the temporal evolution on the surface of the cavity.

Five experiments per strain were performed and, as discussed before, the cells were trapped twenty minutes and released afterwards. It took less than a minute for the free-floating biofilms to sediment on the surface. Through the temporal evaluation of the cluster we found out that the clusters did not disperse into the bulk, see Figure 4.10, on the contrary, the cells remained entangled maintaining the initial shape, only some cells were able to swim away leaving in some cases a less dense cluster, see the images on Figure 4.10.

Even when is hard to determined if the biofilm is growing by just analyzing just the temporal evolution of area density ρ_A in Figure 4.10 we see that ρ_A grows with time for all the biofilms. The cluster of CsgA+ form we found a minimal growth of 3% of its original size at time zero(t_i), considering the initial size the one that the cluster has when it sediments on the surface, and a maximum growth ,after 60 minutes, of 22%. On the other hand, CsgA+ had the same minimal growth (3%) and a 27% maximum.Clusters formed with non-motile cells exhibited a minimum of 2% and a maximum of 20%.

These minimal variations of growth for the different phenotypes do not tell much about the impact of the presence of flagella or the over-expression or knockout of curli has on the dispersion or growth once the aggregate hits the surface. In order to have a clearer result a

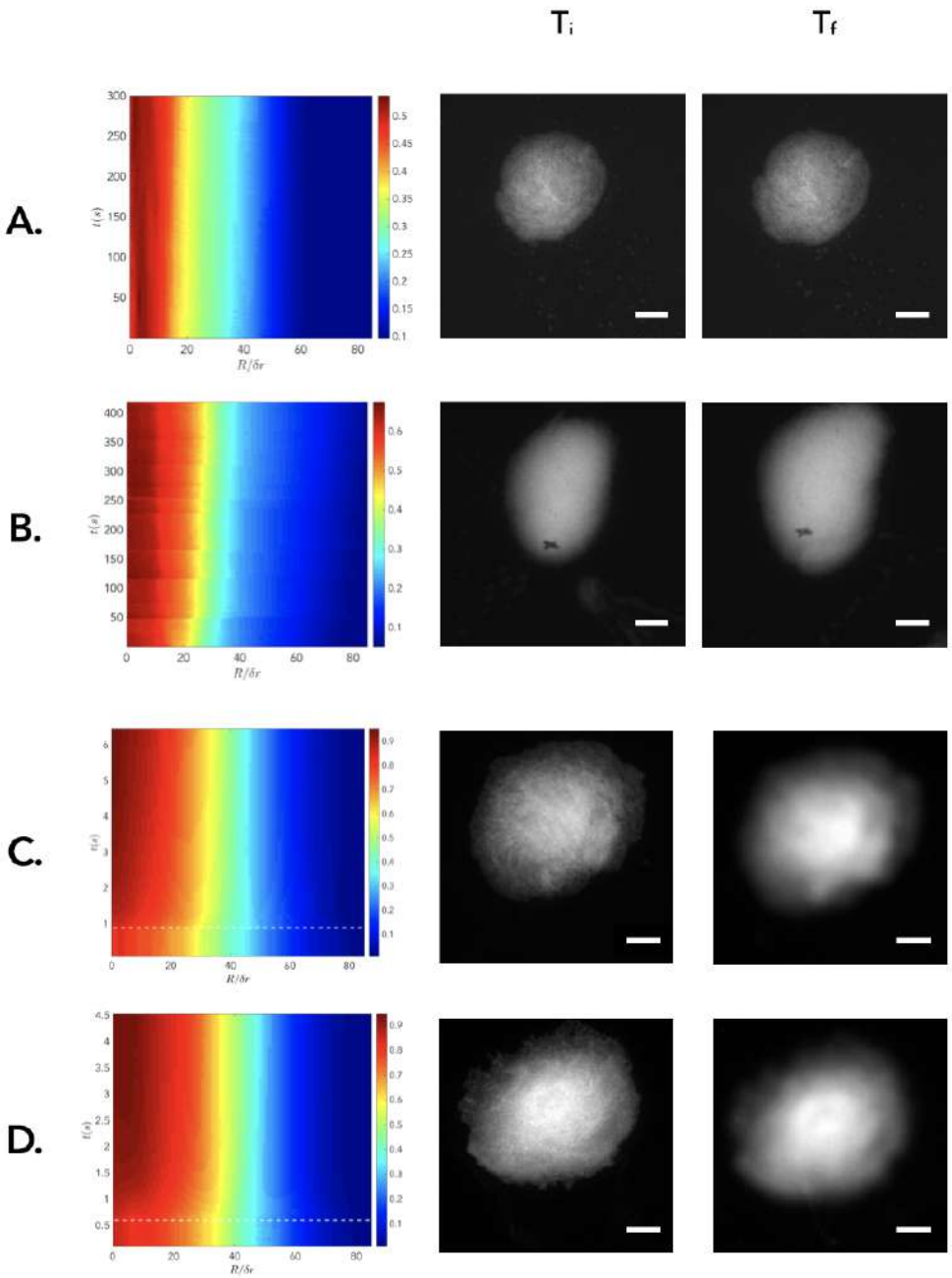

Fig. 4.9 **Clustering and spreading processes for CsgA+ and CsgA-**. The clustering dynamics for CsgA+ and CsgA- cells,**A** and **B** respectively. The images next to each heat map correspond to the starting small cluster of bacteria as a starting point (T_i) and the stable cluster after a given time (T_f). **C** and **D** shows the spreading dynamics for both strains. Both, the CsgA+ cluster **(C)** and the CsgA- one **(D)** is similar to the one exhibit by non-motile cells, i.e. the cluster remains consolidated until its sedimentation.

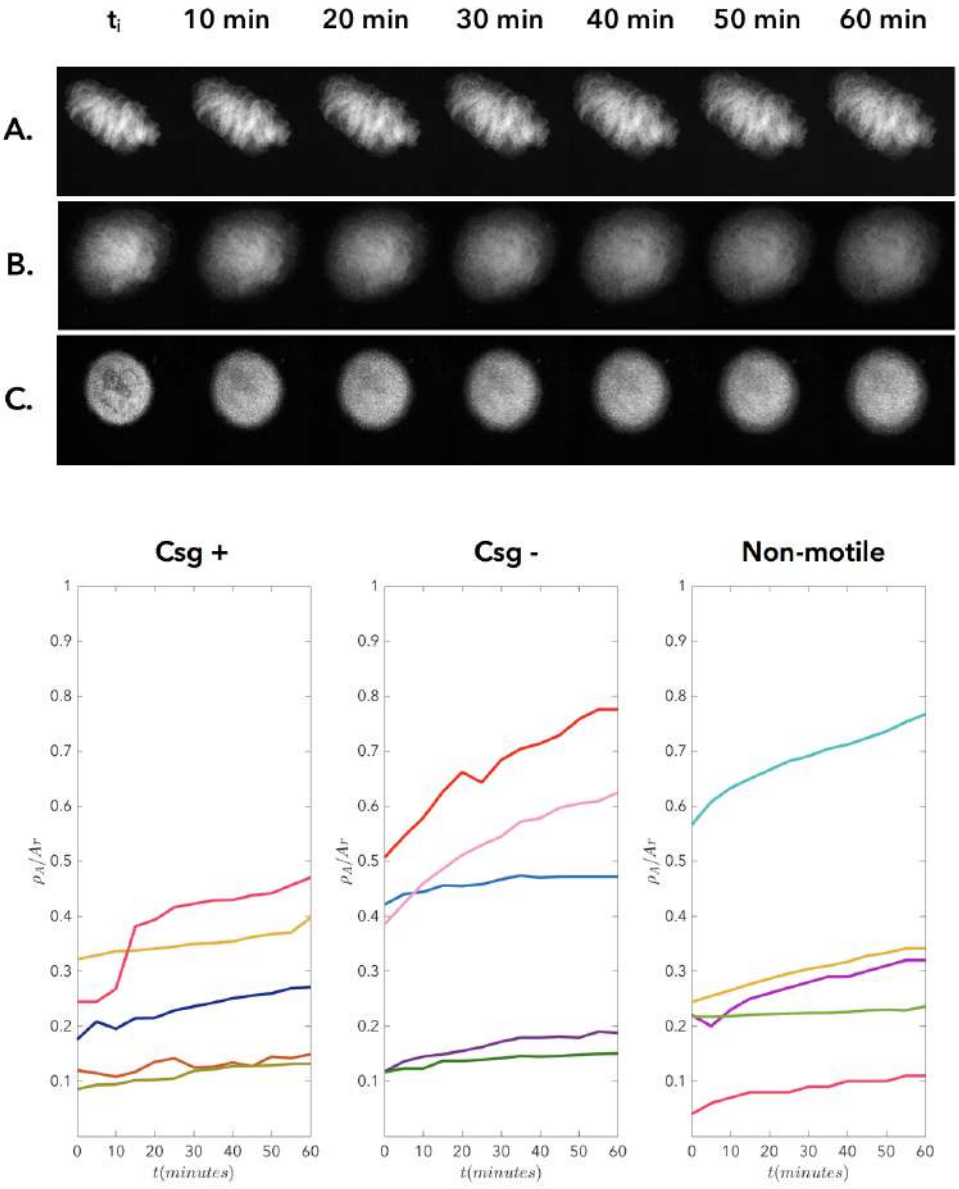

Fig. 4.10 **Temporal evolution of aggregates on the surface. Top panel.** Images showing the evolution of the sedimented cluster on the surface of the cavity at t_i up to one hour.(A) A typical wrinkled cluster of CsgA+ did not disaggregate and kept its shape after one one on the surface, as it also occurred with the representative cluster of CsgA-(B) and Jovanovic $\Delta fliER$ the non-motile strain (C). **Bottom panel.** The temporal evolution of the area density ρ_A, normalized with respect to the total area of the region (the area of the image in pixels (A_r), of the three strains shows that there is and increase of the aggregate size with time in all five replicates.

cellular arrest should be made, preventing the division of bacteria cells, so we could then conclude if the growth is due to dispersion or cellular division and maturation of the biofilm.

4.4.3 Density distribution on the cavity surface

The biofilm-like clusters are now settle on the surface of the cavity and their temporal evolution has been assessed. As reported on Chapter 1, the acoustic energy distribution in the cavity of our acoustic resonator is not homogeneous. In order to map where the energetic hot-spots were in each experiment we analyzed the density distribution, as in intensity of pixels distribution, on the cavity.

The density distribution in the 36 regions, in which our resonator is divided, shows a significant difference between the control resonator and the resonator for experiments. These implies that the distribution of the cells that were not exposed to acoustic fields differs from that of the trapped cells. Figure 4.11 shows that the density distribution of the control resonator of CsgA- cells was quasi-homogeneous, except on one experiment, whereas the density distribution of the resonator, where the confinement took place, has maximums at the regions where the cluster were formed. The minimums correspond to the regions where the cell concentration (the number of pixels corresponding to bacteria) decreased because they were dragged to more energetic hot-spots.

In the case of the experiments with CsgA+ cells (**??**), the density distribution on the surface of the control resonator is homogeneous and the quantity of cells in all regions is always greater than the surface where the trapped cells are. Also, the distribution of the treated cells is not-homogeneous. The fact that we do not have, in any region or experiments, peaks representing higher density on the treated cells than on the control tells us that the biofilm-like clusters are on zones that we could not map with our technique.

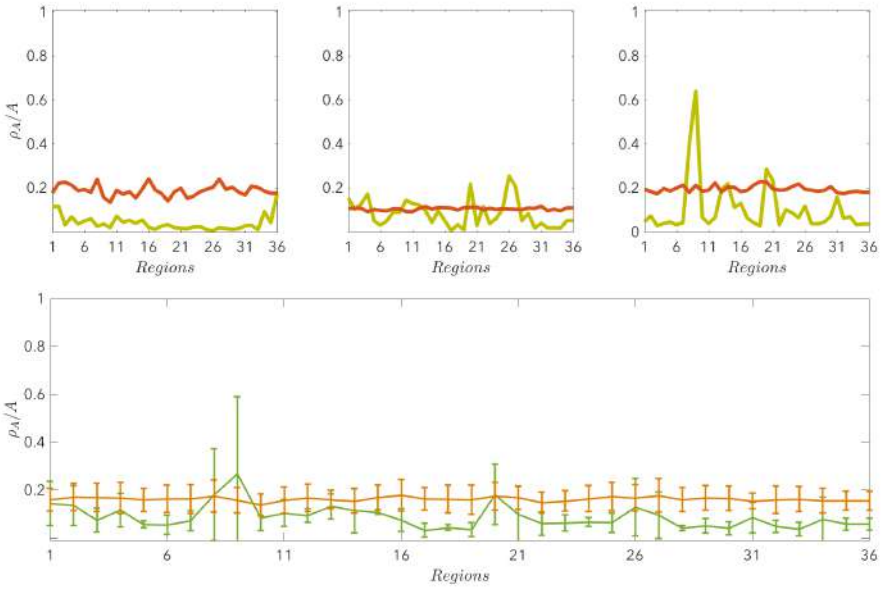

Fig. 4.11 **Density distribution of CsgA- cells on the surface of the cavity.** Three representative experiments of the density distribution in the control resonator (orange lines) and the resonator where cells were acoustically confined for 20 minutes and previously release (green lines). In the three cases the distribution on the control is quasi-homogeneous whereas the one containing the cells treated with acoustic present peaks depending on the region. These peaks and valleys shows either a increase in the density (peaks) or regions where the density of cells is almost zero in some case. The bottom panel represents the average distribution for the 3 experiments where the error bar is the standard deviation.

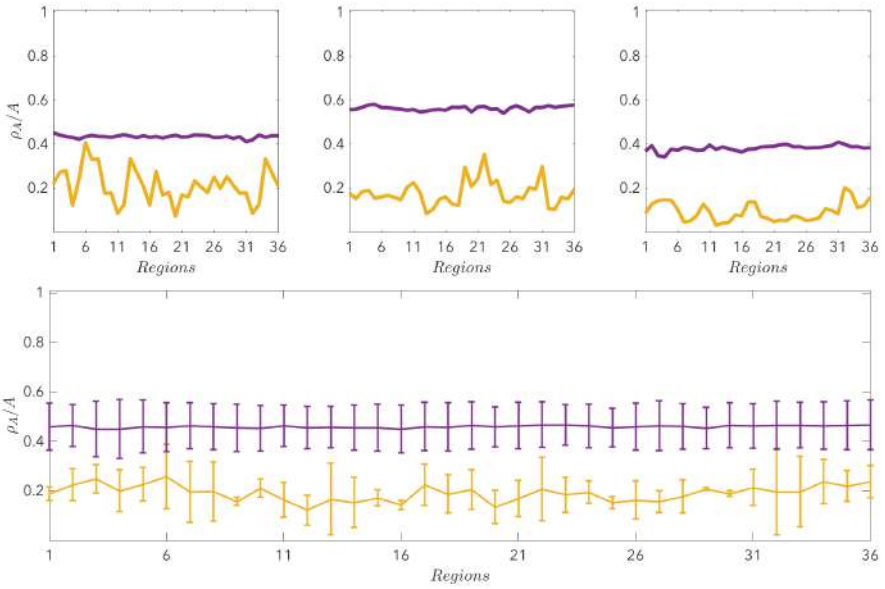

Fig. 4.12 Density distribution of CsgA+ cells on the surface of the cavity. Three representative experiments of the density distribution in the control resonator (purple lines) and the resonator where cells were acoustically confined for 20 minutes and previously release (yellow lines). The density distribution on the surface of the control resonator is homogeneous and the quantity of cells in all regions is always greater than that of the surface where the trapped cells are. Nevertheless the density on the resonator where the acoustic trapping took place fluctuates. The bottom panel represents the average distribution for the 3 experiments where the error bar is the standard deviation.

4.4.4 Minimum inhibitory concentration

Chapter 5

Discussion and perspectives

The magnitude of the vertical acoustic forces, measured experimentally in our trap, are in the order of piconewtons. Even though we do not measure its transversal component neither the Bjerknes forces, it is well known that they are two orders of magnitude smaller than the primary radiation forces [66].

The acoustic forces confine motile bacteria cells at the nodal plane in thin disk-shaped clusters, restricting their degrees of freedom. When the acoustic field is activated, the local density suddenly increases at the energetic hot spots distributed along the nodal plane, triggering the emergence of clusters and collective effects.

Within the levitating cluster of motile cells a collective dynamics emerged, but on cluster of non-motile bacteria there was no collective displacement of bacteria. The behaviour exhibited by motile bacteria resembles a self-assembled pump-like structure.

The turbulent bio-flow within the cluster was characterized measuring the mean kinetic energy and enstrophy as a function of the confinement strength. This analysis showed us that when the transversal trapping weakened the mean energy of the global change did not changed significantly. This is due to the fact that cell are viable and can replicate. In order words, we started the experiment with a cluster with a density ρ and a maximum confinement applying 20 $U_p p$, by reducing the applied voltage we reduce the confinement strength so the virtual transversal constrains loosen up. It is intuitive to think that as the trap grow bigger bacteria cells are able to displace freely and re-gain degrees of freedom, but under the experimental condition we worked the trap grew bigger but the density of bacteria increased. That is why the mean kinetic energy did not changed significantly.

We then showed that when the acoustic trap is suppressed after a few minutes, the floating confined cluster diffuses back into the bulk following an exponential decay, see Chapter 3. The cells are free to escape and they spread around the volume.

However the spreading dynamics was not the same for the cluster formed by non-motile cells. After the removal of the acoustic input the cluster remain consolidated until its sedimentation on the cavity surface. Therefore, it seems that bacteria suffer a strong entanglement with a concomitant aggregation. Similarly, when bacteria are attracted to surfaces[10, 103], they also concentrate and lose motility[130], eventually forming free-floating biofilms[49].

Later the analysis of three other strains corroborated the formation of free-floating biofilms under acoustic confinement. It also proved that depending on the bacteria phenotype the biofilms presented specific characteristics.

We still need to perform biochemical analysis of the clustered bacteria, looking for genetic signals, to make sure that indeed what we have is a biofilms. Nevertheless, from a physical point of view, the first condition to create a biofilm has been attained: bacteria become crowded at a specific place and complex interactions modify their collective behaviour. In our case, this process was enhanced by an acoustic field where the surface interaction can be neglected and where there is no need of surface-attached biofilms or aggregates as seeds. This will give us crucial knowledge of biofilm development without surface interaction, possibly to produce models to evaluate antibiotics in a rapid and cheaper way.

References

[1] Adler, J. and Tso, W.-W. (1974). " decision"-making in bacteria: Chemotactic response of escherichia coli to conflicting stimuli. *Science*, 184(4143):1292–1294.

[2] Airy, G. B. (1835). On the diffraction of an object-glass with circular aperture. *Transactions of the Cambridge Philosophical Society*, 5:283.

[3] Aranson, I. S., Sokolov, A., Kessler, J. O., and Goldstein, R. E. (2007). Model for dynamical coherence in thin films of self-propelled microorganisms. *Physical Review E*, 75(4):040901.

[4] Augustsson, P., Barnkob, R., Wereley, S. T., Bruus, H., and Laurell, T. (2011). Automated and temperature-controlled micro-piv measurements enabling long-term-stable microchannel acoustophoresis characterization. *Lab on a Chip*, 11(24):4152–4164.

[5] Azeredo, J., Azevedo, N. F., Briandet, R., Cerca, N., Coenye, T., Costa, A. R., Desvaux, M., Di Bonaventura, G., Hébraud, M., Jaglic, Z., et al. (2017). Critical review on biofilm methods. *Critical reviews in microbiology*, 43(3):313–351.

[6] Badel, S., Laroche, C., Gardarin, C., Bernardi, T., and Michaud, P. (2008). New method showing the influence of matrix components in leuconostoc mesenteroides biofilm formation. *Applied biochemistry and biotechnology*, 151(2-3):364–370.

[7] Baker, N. V. (1972). Segregation and sedimentation of red blood cells in ultrasonic standing waves. *Nature*, 239(5372):398.

[8] Barnkob, R., Augustsson, P., Laurell, T., and Bruus, H. (2010). Measuring the local pressure amplitude in microchannel acoustophoresis. *Lab on a chip*, 10 5:563–70.

[9] Bazou, D., Coakley, W. T., Hayes, A., and Jackson, S. K. (2008). Long-term viability and proliferation of alginate-encapsulated 3-d hepg2 aggregates formed in an ultrasound trap. *Toxicology in Vitro*, 22(5):1321–1331.

[10] Beloin, C., Roux, A., and Ghigo, J.-M. (2008). Escherichia coli biofilms. In *Bacterial biofilms*, pages 249–289. Springer.

[11] Berg, H. C. (1993). *Random walks in biology*. Princeton University Press.

[12] Berg, H. C. (2003). The rotary motor of bacterial flagella. *Annual review of biochemistry*, 72.

[13] Berg, H. C., Brown, D. A., et al. (1972). Chemotaxis in escherichia coli analysed by three-dimensional tracking. *Nature*, 239(5374):500–504.

[14] Berne, C., Ducret, A., Hardy, G. G., and Brun, Y. V. (2015). Adhesins involved in attachment to abiotic surfaces by gram-negative bacteria. *Microbiology spectrum*, 3(4).

[15] Berry, R. E., Klumpp, D. J., and Schaeffer, A. J. (2009). Urothelial cultures support intracellular bacterial community formation by uropathogenic escherichia coli. *Infection and immunity*, 77(7):2762–2772.

[16] Blakemore, R. P. (1982). Magnetotactic bacteria. *Annual Reviews in Microbiology*, 36(1):217–238.

[17] Boluriaan, S. and Morris, P. J. (2003). Acoustic streaming: from rayleigh to today. *International Journal of aeroacoustics*, 2(3):255–292.

[18] Brugger, S. D., Baumberger, C., Jost, M., Jenni, W., Brugger, U., and Mühlemann, K. (2012). Automated counting of bacterial colony forming units on agar plates. *PloS one*, 7(3):e33695.

[19] Bruus, H. (2012a). Acoustofluidics 2: Perturbation theory and ultrasound resonance modes. *Lab Chip*, 12:20–28.

[20] Bruus, H. (2012b). Acoustofluidics 7: The acoustic radiation force on small particles. *Lab Chip*, 12:1014–1021.

[21] Bruus, H., Dual, J., Hawkes, J., Hill, M., Laurell, T., Nilsson, J., Radel, S., Sadhal, S., and Wiklund, M. (2011). Forthcoming lab on a chip tutorial series on acoustofluidics: Acoustofluidics—exploiting ultrasonic standing wave forces and acoustic streaming in microfluidic systems for cell and particle manipulation. *Lab on a Chip*, 11(21):3579–3580.

[22] Cates, M. and Tailleur, J. (2013). When are active brownian particles and run-and-tumble particles equivalent? consequences for motility-induced phase separation. *EPL (Europhysics Letters)*, 101(2):20010.

[23] Cates, M. E. (2012). Diffusive transport without detailed balance in motile bacteria: does microbiology need statistical physics? *Reports on Progress in Physics*, 75(4):042601.

[24] Ceri, H., Olson, M., Stremick, C., Read, R., Morck, D., and Buret, A. (1999). The calgary biofilm device: new technology for rapid determination of antibiotic susceptibilities of bacterial biofilms. *Journal of clinical microbiology*, 37(6):1771–1776.

[25] Chang, Y.-W., Fragkopoulos, A. A., Marquez, S. M., Kim, H. D., Angelini, T. E., and Fernández-Nieves, A. (2015). Biofilm formation in geometries with different surface curvature and oxygen availability. *New Journal of Physics*, 17(3):033017.

[26] Chattopadhyay, S., Moldovan, R., Yeung, C., and Wu, X. (2006). Swimming efficiency of bacterium escherichiacoli. *Proceedings of the National Academy of Sciences*, 103(37):13712–13717.

[27] Chavant, P., Gaillard-Martinie, B., Talon, R., Hébraud, M., and Bernardi, T. (2007). A new device for rapid evaluation of biofilm formation potential by bacteria. *Journal of microbiological methods*, 68(3):605–612.

[28] Chladni, E. F. F. (1787). *Entdeckungen über die Theorie des Klanges*. Zentralantiquariat der DDR.

[29] Cisneros, L. H., Cortez, R., Dombrowski, C., Goldstein, R. E., and Kessler, J. O. (2010). Fluid dynamics of self-propelled microorganisms, from individuals to concentrated populations. In *Animal Locomotion*, pages 99–115. Springer.

[30] Coakley, W., Hawkes, J., Sobanski, M., Cousins, C., and Spengler, J. (2000). Analytical scale ultrasonic standing wave manipulation of cells and microparticles. *Ultrasonics*, 38(1-8):638–641.

[31] Coakley, W. T., Bardsley, D. W., Grundy, M. A., Zamani, F., and Clarke, D. J. (1989). Cell manipulation in ultrasonic standing wave fields. *Journal of Chemical Technology & Biotechnology*, 44(1):43–62.

[32] Coenye, T. and Nelis, H. J. (2010). In vitro and in vivo model systems to study microbial biofilm formation. *Journal of microbiological methods*, 83(2):89–105.

[33] Cohen, N. R., Lobritz, M. A., and Collins, J. J. (2013). Microbial persistence and the road to drug resistance. *Cell host & microbe*, 13(6):632–642.

[34] Cookson, A. L., Cooley, W. A., and Woodward, M. J. (2002). The role of type 1 and curli fimbriae of shiga toxin-producing escherichia coli in adherence in abiotic surfaces. *International Journal of Medical Microbiology*, 292(3/4):195.

[35] Cooper, G. L., Schiller, A., and Hopkins, C. C. (1988). Possible role of capillary action in pathogenesis of experimental catheter-associated dermal tunnel infections. *Journal of clinical microbiology*, 26(1):8–12.

[36] Costerton, J., Ingram, J., and Cheng, K. (1974). Structure and function of the cell envelope of gram-negative bacteria. *Bacteriological reviews*, 38(1):87.

[37] Costerton, J. W. (1999). Introduction to biofilm. *International journal of antimicrobial agents*, 11(3):217–221.

[38] Costerton, J. W., Geesey, G., and Cheng, K.-J. (1978). How bacteria stick. *Scientific American*, 238(1):86–95.

[39] Costerton, J. W., Stewart, P. S., and Greenberg, E. P. (1999). Bacterial biofilms: a common cause of persistent infections. *Science*, 284(5418):1318–1322.

[40] Couce, A. and Blázquez, J. (2009). Side effects of antibiotics on genetic variability. *FEMS microbiology reviews*, 33(3):531–538.

[41] Danese, P. N., Pratt, L. A., Dove, S. L., and Kolter, R. (2000). The outer membrane protein, antigen 43, mediates cell-to-cell interactions within escherichia coli biofilms. *Molecular microbiology*, 37(2):424–432.

[42] Dang, H. and Lovell, C. R. (2016). Microbial surface colonization and biofilm development in marine environments. *Microbiology and Molecular Biology Reviews*, 80(1):91–138.

[43] Davey, M. E. and O'toole, G. A. (2000). Microbial biofilms: from ecology to molecular genetics. *Microbiology and molecular biology reviews*, 64(4):847–867.

[44] Doinikov, A. (2003). Acoustic radiation forces: Classical theory and recent advances. 1:39–67.

[45] Donachie, W. D. (1993). The cell cycle of escherichia coli. *Annual Reviews in Microbiology*, 47(1):199–230.

[46] Donlan, R. M. (2002). Biofilms: microbial life on surfaces. *Emerging infectious diseases*, 8(9):881.

[47] Drescher, K., Dunkel, J., Cisneros, L. H., Ganguly, S., and Goldstein, R. E. (2011). Fluid dynamics and noise in bacterial cell–cell and cell–surface scattering. *Proceedings of the National Academy of Sciences*, 108(27):10940–10945.

[48] Drescher, K., Goldstein, R. E., Michel, N., Polin, M., and Tuval, I. (2010). Direct measurement of the flow field around swimming microorganisms. *Physical Review Letters*, 105(16):168101.

[49] Drescher, K., Shen, Y., Bassler, B. L., and Stone, H. A. (2013). Biofilm streamers cause catastrophic disruption of flow with consequences for environmental and medical systems. *Proceedings of the National Academy of Sciences*, 110(11):4345–4350.

[50] Dron, O. (2011). *Micro-manipulation acoustique de particules: application aux mesures par micro-PIV*. PhD thesis, Paris 7.

[51] Dunkel, J., Heidenreich, S., Drescher, K., Wensink, H. H., Bär, M., and Goldstein, R. E. (2013). Fluid dynamics of bacterial turbulence. *Physical review letters*, 110(22):228102.

[52] Dyson, M., Woodward, B., and Pond, J. (1971). Flow of red blood cells stopped by ultrasound. *Nature*, 232(5312):572.

[53] Elder, S. A. (1959). Cavitation microstreaming. *The Journal of the Acoustical Society of America*, 31(1):54–64.

[54] Erban, R. and Othmer, H. G. (2004). From individual to collective behavior in bacterial chemotaxis. *SIAM Journal on Applied Mathematics*, 65(2):361–391.

[55] Faraday, M. et al. (1837). On a peculiar class of acoustical figures; and on certain forms assumed by groups of particles upon vibrating elastic surfaces. In *Abstracts of the Papers Printed in the Philosophical Transactions of the Royal Society of London*, volume 3, pages 49–51. The Royal Society.

[56] Fei, C., Ma, J., Chiu, C. T., Williams, J. A., Fong, W., Chen, Z., Zhu, B., Xiong, R., Shi, J., Hsiai, T. K., Shung, K. K., and Zhou, Q. (2015). Design of matching layers for high-frequency ultrasonic transducers. *Applied Physics Letters*, 107(12):123505.

[57] Flemming, H.-C., Neu, T. R., and Wozniak, D. J. (2007). The eps matrix: the "house of biofilm cells". *Journal of bacteriology*, 189(22):7945–7947.

[58] Flemming, H.-C. and Wingender, J. (2010). The biofilm matrix. *Nature Reviews Microbiology*, 8(9):623.

[59] Frampton, K. D., Martin, S. E., and Minor, K. (2003). The scaling of acoustic streaming for application in micro-fluidic devices. *Applied Acoustics*, 64(7):681–692.

[60] Francis, N. R., Sosinsky, G. E., Thomas, D., and DeRosier, D. J. (1994). Isolation, characterization and structure of bacterial flagellar motors containing the switch complex. *Journal of molecular biology*, 235(4):1261–1270.

[61] Garg, S., Huifu, H., Kaul, S. C., and Wadhwa, R. (2018). Integration of conventional cell viability assays for reliable and reproducible read-outs: experimental evidence. *BMC research notes*, 11(1):403.

[62] Geesey, G., Richardson, W., Yeomans, H., Irvin, R., and Costerton, J. (1977). Microscopic examination of natural sessile bacterial populations from an alpine stream. *Canadian Journal of Microbiology*, 23(12):1733–1736.

[63] Goeres, D. M., Hamilton, M. A., Beck, N. A., Buckingham-Meyer, K., Hilyard, J. D., Loetterle, L. R., Lorenz, L. A., Walker, D. K., and Stewart, P. S. (2009). A method for growing a biofilm under low shear at the air–liquid interface using the drip flow biofilm reactor. *Nature protocols*, 4(5):783.

[64] González-Gutiérrez, J., Carrillo-Estrada, J., and Ruiz-Suárez, J. (2014). Nucleation, aggregation, annealing, and disintegration of granular clusters. *Physical Review E*, 89(5):052205.

[65] Gor'kov, L. P. (1962). On the Forces Acting on a Small Particle in an Acoustical Field in an Ideal Fluid. *Soviet Physics Doklady*, 6:773.

[66] Gröschl, M. (1998). Ultrasonic separation of suspended particles-part i: Fundamentals. *Acta Acustica united with Acustica*, 84(3):432–447.

[67] Gutiérrez-Ramos, S., Hoyos, M., and Ruiz-Suárez, J. (2018). Induced clustering of escherichia coli by acoustic fields. *Scientific reports*, 8(1):4668.

[68] Hacker, J. and Blum-Oehler, G. (2007). In appreciation of theodor escherich.

[69] Hagsater, S. M., Jensen, T. G., Bruus, H., and Kutter, J. P. (2007). Acoustic resonances in microfluidic chips: full-image micro-piv experiments and numerical simulations. *Lab Chip*, 7:1336–1344.

[70] Hall-Stoodley, L., Costerton, J. W., and Stoodley, P. (2004). Bacterial biofilms: from the natural environment to infectious diseases. *Nature reviews microbiology*, 2(2):95.

[71] Hammarström, B., Evander, M., Barbeau, H., Bruzelius, M., Larsson, J., Laurell, T., and Nilsson, J. (2010). Non-contact acoustic cell trapping in disposable glass capillaries. *Lab on a Chip*, 10(17):2251–2257.

[72] Harkes, G., Dankert, J., and Feijen, J. (1992). Bacterial migration along solid surfaces. *Applied and environmental microbiology*, 58(5):1500–1505.

[73] Harrison, J. J., Ceri, H., Yerly, J., Stremick, C. A., Hu, Y., Martinuzzi, R., and Turner, R. J. (2006). The use of microscopy and three-dimensional visualization to evaluate the structure of microbial biofilms cultivated in the calgary biofilm device. *Biological procedures online*, 8(1):194.

[74] Hawkes, J. J., Barber, R. W., Emerson, D. R., and Coakley, W. T. (2004). Continuous cell washing and mixing driven by an ultrasound standing wave within a microfluidic channel. *Lab on a Chip*, 4(5):446–452.

[75] Hawkes, J. J. and Coakley, W. T. (2001). Force field particle filter, combining ultrasound standing waves and laminar flow. *Sensors and Actuators B: Chemical*, 75(3):213–222.

[76] Hazelbauer, G. L., Berg, H. C., and Matsumura, P. (1993). Bacterial motility and signal transduction. *Cell*, 73(1):15–22.

[77] Hengge, R. (2009). Principles of c-di-gmp signalling in bacteria. *Nature Reviews Microbiology*, 7(4):263.

[78] Henk, M. C. (2014). Capturing air–water interface biofilms for microscopy and molecular analysis. In *Microbial Biofilms*, pages 301–322. Springer.

[79] Henrici, A. T. (1933). Studies of freshwater bacteria: I. a direct microscopic technique. *Journal of bacteriology*, 25(3):277.

[80] Hernández-Jiménez, E., del Campo, R., Toledano, V., Vallejo-Cremades, M. T., Muñoz, A., Largo, C., Arnalich, F., García-Rio, F., Cubillos-Zapata, C., and López-Collazo, E. (2013). Biofilm vs. planktonic bacterial mode of growth: Which do human macrophages prefer? *Biochemical and biophysical research communications*, 441(4):947–952.

[81] Heukelekian, H. and Heller, A. (1940). Relation between food concentration and surface for bacterial growth. *Journal of bacteriology*, 40(4):547.

[82] Høiby, N. (2017). A short history of microbial biofilms and biofilm infections. *Apmis*, 125(4):272–275.

[83] Huang, K. C., Mukhopadhyay, R., Wen, B., Gitai, Z., and Wingreen, N. S. (2008). Cell shape and cell-wall organization in gram-negative bacteria. *Proceedings of the National Academy of Sciences*, pages pnas–0805309105.

[84] Ingham, C. J. and Jacob, E. B. (2008). Swarming and complex pattern formation in paenibacillus vortex studied by imaging and tracking cells. *BMC microbiology*, 8(1):36.

[85] Jarrell, K. F. and McBride, M. J. (2008). The surprisingly diverse ways that prokaryotes move. *Nature Reviews Microbiology*, 6(6):466–476.

[86] Jenal, U. and Malone, J. (2006). Mechanisms of cyclic-di-gmp signaling in bacteria. *Annu. Rev. Genet.*, 40:385–407.

[87] Johnston, M. D. and Jones, M. V. (1995). Disinfection tests with intact biofilms: combined use of the modified robbins device with impedance detection. *Journal of microbiological methods*, 21(1):15–26.

[88] Jung, Y.-G., Choi, J., Kim, S.-K., Lee, J.-H., and Kwon, S. (2014). Embedded biofilm: a new biofilm model based on the embedded growth of bacteria. *Applied and environmental microbiology*, pages AEM–02311.

[89] Kearns, D. B. (2010). A field guide to bacterial swarming motility. *Nature Reviews Microbiology*, 8(9):634.

[90] Keller, E. F. and Segel, L. A. (1971). Traveling bands of chemotactic bacteria: a theoretical analysis. *Journal of theoretical biology*, 30(2):235–248.

[91] Kharazmi, A., Giwercman, B., and Høiby, N. (1999). [16] robbins device in biofilm research. In *Methods in enzymology*, volume 310, pages 207–215. Elsevier.

[92] Khatami, M., Wolff, K., Pohl, O., Ejtehadi, M. R., and Stark, H. (2016). Active brownian particles and run-and-tumble particles separate inside a maze. *Scientific Reports*, 6:37670.

[93] Kim, Y. W., Subramanian, S., Gerasopoulos, K., Ben-Yoav, H., Wu, H.-C., Quan, D., Carter, K., Meyer, M. T., Bentley, W. E., and Ghodssi, R. (2015). Effect of electrical energy on the efficacy of biofilm treatment using the bioelectric effect. *npj Biofilms and Microbiomes*, 1:15016.

[94] King, L. V. et al. (1934). On the acoustic radiation pressure on spheres. *Proc. R. Soc. Lond. A*, 147(861):212–240.

[95] Klausen, M., Heydorn, A., Ragas, P., Lambertsen, L., Aaes-Jørgensen, A., Molin, S., and Tolker-Nielsen, T. (2003). Biofilm formation by pseudomonas aeruginosa wild type, flagella and type iv pili mutants. *Molecular microbiology*, 48(6):1511–1524.

[96] Knobler, S. L., Lemon, S. M., Najafi, M., Burroughs, T., et al. (2003). Factors contributing to the emergence of resistance.

[97] Koch, A. L., Higgins, M. L., and Doyle, R. J. (1982). The role of surface stress in the morphology of microbes. *Microbiology*, 128(5):927–945.

[98] Kragh, K., Hutchison, J., Melaugh, G., Rodesney, C., Roberts, A., Irie, Y., Jensen, P., Diggle, S., Allen, R., Gordon, V., et al. (2016). Role of multicellular aggregates in biofilm formation. mbio 7: e00237-16.

[99] Kundt, A. (1866). Über eine neue art akustischer staubfiguren und über die anwendung derselben zur bestimmung der schallgeschwindigkeit in festen körpern und gasen. *Annalen der Physik*, 203(4):497–523.

[100] Kuznetsova, L. A. and Coakley, W. T. (2004). Microparticle concentration in short path length ultrasonic resonators: Roles of radiation pressure and acoustic streaming. *The Journal of the Acoustical Society of America*, 116(4):1956–1966.

[101] Lambert, R. A., Picano, F., Breugem, W.-P., and Brandt, L. (2013). Active suspensions in thin films: nutrient uptake and swimmer motion. *Journal of Fluid Mechanics*, 733:528–557.

[102] Lauga, E. (2016). Bacterial hydrodynamics. *Annual Review of Fluid Mechanics*, 48:105–130.

[103] Lauga, E. and Powers, T. R. (2009). The hydrodynamics of swimming microorganisms. *Reports on Progress in Physics*, 72(9):096601.

[104] Lebeaux, D., Chauhan, A., Rendueles, O., and Beloin, C. (2013). From in vitro to in vivo models of bacterial biofilm-related infections. *Pathogens*, 2(2):288–356.

[105] Lega, J. and Passot, T. (2006). Hydrodynamics of bacterial colonies. *Nonlinearity*, 20(1):C1.

[106] Lenshof, A., Evander, M., Laurell, T., and Nilsson, J. (2012). Acoustofluidics 5: Building microfluidic acoustic resonators. *Lab Chip*, 12:684–695.

[107] Lierke, E. (1996). Acoustic levitation–a comprehensive survey of principles and applications. *Acta Acustica united with Acustica*, 82(2):220–237.

[108] Lighthill, S. J. (1978). Acoustic streaming. *Journal of Sound and Vibration*, 61(3):391 – 418.

[109] Liu, H.-L. and Hsieh, C.-M. (2009). Single-transducer dual-frequency ultrasound generation to enhance acoustic cavitation. *Ultrasonics sonochemistry*, 16(3):431–438.

[110] Liu, J., Prindle, A., Humphries, J., Gabalda-Sagarra, M., Asally, M., Dong-yeon, D. L., Ly, S., Garcia-Ojalvo, J., and Süel, G. M. (2015). Metabolic co-dependence gives rise to collective oscillations within biofilms. *Nature*, 523(7562):550.

[111] Ludovic, B. (2017). Manipulation acoustique de cellules souches mesenchymateuses.

[112] Lushi, E., Wioland, H., and Goldstein, R. E. (2014). Fluid flows created by swimming bacteria drive self-organization in confined suspensions. *Proceedings of the National Academy of Sciences*, page 201405698.

[113] Macnab, R. M. (2003). How bacteria assemble flagella. *Annual Reviews in Microbiology*, 57(1):77–100.

[114] Maier, B. and Wong, G. C. (2015). How bacteria use type iv pili machinery on surfaces. *Trends in microbiology*, 23(12):775–788.

[115] McBain, A. J. (2009). In vitro biofilm models: an overview. *Advances in applied microbiology*, 69:99–132.

[116] Moens, S. and Vanderleyden, J. (1996). Functions of bacterial flagella. *Critical reviews in microbiology*, 22(2):67–100.

[117] Mora, T., Yu, H., Sowa, Y., and Wingreen, N. S. (2009). Steps in the bacterial flagellar motor. *PLoS computational biology*, 5(10):e1000540.

[118] Münster, U., Heikkinen, E., and Knulst, J. (1997). Nutrient composition, microbial biomass and activity at the air–water interface of small boreal forest lakes. *Hydrobiologia*, 363(1-3):261–270.

[119] Nanninga, N. (1998). Morphogenesis of escherichia coli. *Microbiology and Molecular Biology Reviews*, 62(1):110–129.

[120] Nash, R. W., Adhikari, R., Tailleur, J., and Cates, M. E. (2010). Run-and-tumble particles with hydrodynamics: Sedimentation, trapping, and upstream swimming. *Phys. Rev. Lett.*, 104:258101.

[121] Niba, E. T. E., Naka, Y., Nagase, M., Mori, H., and Kitakawa, M. (2007). A genome-wide approach to identify the genes involved in biofilm formation in e. coli. *DNA research*, 14(6):237–246.

[122] Nilsson, J., Evander, M., Hammarström, B., and Laurell, T. (2009). Review of cell and particle trapping in microfluidic systems. *Analytica Chimica Acta*, 649(2):141 – 157.

[123] Nirody, J. A., Sun, Y.-R., and Lo, C.-J. (2017). The biophysicist's guide to the bacterial flagellar motor. *Advances in Physics: X*, 2(2):324–343.

[124] Nyborg, W. L. (1958). Acoustic streaming near a boundary. *The Journal of the Acoustical Society of America*, 30(4):329–339.

[125] Ohlin, M. (2015). *Ultrasonic Fluid and Cell Manipulation*. PhD thesis, KTH Royal Institute of Technology.

[126] Olivares, E., Badel-Berchoux, S., Provot, C., Jaulhac, B., Prévost, G., Bernardi, T., and Jehl, F. (2015). The biofilm ring test®: a rapid method for the routine analysis of p. aeruginosa biofilm formation kinetics. *Journal of clinical microbiology*, pages JCM–02938.

[127] Olson, M. E., Ceri, H., Morck, D. W., Buret, A. G., and Read, R. R. (2002). Biofilm bacteria: formation and comparative susceptibility to antibiotics. *Canadian Journal of Veterinary Research*, 66(2):86.

[128] Organization, W. H. et al. (2014). *Antimicrobial resistance: global report on surveillance*. World Health Organization.

[129] Organization, W. H. et al. (2018). High levels of antibiotic resistance found worldwide, new data shows. *Saudi Medical Journal*, 39(4):430–431.

[130] O'Toole, G., Kaplan, H. B., and Kolter, R. (2000). Biofilm formation as microbial development. *Annual Reviews in Microbiology*, 54(1):49–79.

[131] O'toole, G. A. and Kolter, R. (1998). Flagellar and twitching motility are necessary for pseudomonas aeruginosa biofilm development. *Molecular microbiology*, 30(2):295–304.

[132] Ozkan, A., Kinney, K., Katz, L., and Berberoglu, H. (2012). Reduction of water and energy requirement of algae cultivation using an algae biofilm photobioreactor. *Bioresource technology*, 114:542–548.

[133] Parkinson, J. S. (1978). Complementation analysis and deletion mapping of escherichia coli mutants defective in chemotaxis. *Journal of bacteriology*, 135(1):45–53.

[134] Patch, A., Yllanes, D., and Marchetti, M. C. (2017). Kinetics of motility-induced phase separation and swim pressure. *Physical Review E*, 95(1):012601.

[135] Patel, M. V., Nanayakkara, I. A., Simon, M. G., and Lee, A. P. (2014). Cavity-induced microstreaming for simultaneous on-chip pumping and size-based separation of cells and particles. *Lab on a Chip*, 14(19):3860–3872.

[136] Peeters, E., Nelis, H. J., and Coenye, T. (2008). Comparison of multiple methods for quantification of microbial biofilms grown in microtiter plates. *Journal of microbiological methods*, 72(2):157–165.

[137] Pitts, B., Hamilton, M. A., Zelver, N., and Stewart, P. S. (2003). A microtiter-plate screening method for biofilm disinfection and removal. *Journal of microbiological methods*, 54(2):269–276.

[138] Pratt, L. A. and Kolter, R. (1998). Genetic analysis of escherichia coli biofilm formation: roles of flagella, motility, chemotaxis and type i pili. *Molecular microbiology*, 30(2):285–293.

[139] Pratt, L. A. and Kolter, R. (1999). Genetic analyses of bacterial biofilm formation. *Current opinion in microbiology*, 2(6):598–603.

[140] Prindle, A., Liu, J., Asally, M., Ly, S., Garcia-Ojalvo, J., and Süel, G. M. (2015). Ion channels enable electrical communication in bacterial communities. *Nature*, 527(7576):59.

[141] Qi, L., Li, H., Zhang, C., Liang, B., Li, J., Wang, L., Du, X., Liu, X., Qiu, S., and Song, H. (2016). Relationship between antibiotic resistance, biofilm formation, and biofilm-specific resistance in acinetobacter baumannii. *Frontiers in microbiology*, 7:483.

[142] Rayleigh, L. (1884). On the circulation of air observed in kundt's tubes, and on some allied acoustical problem. *Phil. Trans. Roy. Soc*, 175:1–21.

[143] Ren, Y., Wang, C., Chen, Z., Allan, E., van der Mei, H. C., and Busscher, H. J. (2018). Emergent heterogeneous microenvironments in biofilms: substratum surface heterogeneity and bacterial adhesion force-sensing. *FEMS microbiology reviews*, 42(3):259–272.

[144] Richter, L., Stepper, C., Mak, A., Reinthaler, A., Heer, R., Kast, M., Brückl, H., and Ertl, P. (2007). Development of a microfluidic biochip for online monitoring of fungal biofilm dynamics. *Lab on a Chip*, 7(12):1723–1731.

[145] Rittmann, B. E. (2004). Biofilms in the water industry. In *Microbial biofilms*, pages 359–378. American Society of Microbiology.

[146] Römling, U., Galperin, M. Y., and Gomelsky, M. (2013). Cyclic di-gmp: the first 25 years of a universal bacterial second messenger. *Microbiology and Molecular Biology Reviews*, 77(1):1–52.

[147] Roostalu, J., Jõers, A., Luidalepp, H., Kaldalu, N., and Tenson, T. (2008). Cell division in escherichia coli cultures monitored at single cell resolution. *BMC microbiology*, 8(1):68.

[148] Rudney, J., Chen, R., Lenton, P., Li, J., Li, Y., Jones, R., Reilly, C., Fok, A., and Aparicio, C. (2012). A reproducible oral microcosm biofilm model for testing dental materials. *Journal of applied Microbiology*, 113(6):1540–1553.

[149] Schlichting, H. (1932). Berechnung ebener periodischer grenzschichtstromungen. *Phys. z.*, 33:327–335.

[150] Schnitzer, M. J. (1993). Theory of continuum random walks and application to chemotaxis. *Physical Review E*, 48(4):2553.

[151] Schwartz, K., Stephenson, R., Hernandez, M., Jambang, N., and Boles, B. R. (2010). The use of drip flow and rotating disk reactors for staphylococcus aureus biofilm analysis. *Journal of visualized experiments: JoVE*, (46).

[152] Schwarz-Linek, J., Arlt, J., Jepson, A., Dawson, A., Vissers, T., Miroli, D., Pilizota, T., Martinez, V. A., and Poon, W. C. (2016). Escherichia coli as a model active colloid: A practical introduction. *Colloids and Surfaces B: Biointerfaces*, 137:2–16.

[153] Settnes, M. and Bruus, H. (2012). Forces acting on a small particle in an acoustical field in a viscous fluid. *Phys. Rev. E*, 85:016327.

[154] Singh, R., Paul, D., and Jain, R. K. (2006). Biofilms: implications in bioremediation. *Trends in microbiology*, 14(9):389–397.

[155] Singh, S., Singh, S. K., Chowdhury, I., and Singh, R. (2017). Understanding the mechanism of bacterial biofilms resistance to antimicrobial agents. *The open microbiology journal*, 11:53.

[156] Slavkin, H. C. (1997). Biofilms, microbial ecology and antoni van leeuwenhoek. *The Journal of the American Dental Association*, 128(4):492–495.

[157] Sokolov, A., Goldstein, R. E., Feldchtein, F. I., and Aranson, I. S. (2009). Enhanced mixing and spatial instability in concentrated bacterial suspensions. *Physical Review E*, 80(3):031903.

[158] Solon, A. P., Fily, Y., Baskaran, A., Cates, M. E., Kafri, Y., Kardar, M., and Tailleur, J. (2015). Pressure is not a state function for generic active fluids. *Nature Physics*, 11(8):673.

[159] Spengler, J., Coakley, W., and Christensen, K. (2003). Microstreaming effects on particle concentration in an ultrasonic standing wave. *AIChE journal*, 49(11):2773–2782.

[160] Spengler, J. F. and Coakley, W. T. (2003). Ultrasonic trap to monitor morphology and stability of developing microparticle aggregates. *Langmuir*, 19(9):3635–3642.

[161] Spiers, A. J., Bohannon, J., Gehrig, S. M., and Rainey, P. B. (2003). Biofilm formation at the air–liquid interface by the pseudomonas fluorescens sbw25 wrinkly spreader requires an acetylated form of cellulose. *Molecular microbiology*, 50(1):15–27.

[162] Stepanović, S., Vuković, D., Hola, V., BONAVENTURA, G. D., Djukić, S., Ćirković, I., and Ruzicka, F. (2007). Quantification of biofilm in microtiter plates: overview of testing conditions and practical recommendations for assessment of biofilm production by staphylococci. *Apmis*, 115(8):891–899.

[163] Sternberg, C., Christensen, B. B., Johansen, T., Nielsen, A. T., Andersen, J. B., Givskov, M., and Molin, S. (1999). Distribution of bacterial growth activity in flow-chamber biofilms. *Applied and Environmental Microbiology*, 65(9):4108–4117.

[164] Suchanek, V. M. (2017). *Role of Motility and its Regulation in Escherichia coli Biofilm formation*. PhD thesis.

[165] Sundvik, M., Nieminen, H. J., Salmi, A., Panula, P., and Hæggström, E. (2015). Effects of acoustic levitation on the development of zebrafish, danio rerio, embryos. *Scientific reports*, 5:13596.

[166] Sutherland, I. W. (2001). The biofilm matrix–an immobilized but dynamic microbial environment. *Trends in microbiology*, 9(5):222–227.

[167] Sutton, S. (2011). Measurement of microbial cells by optical density. *Journal of Validation technology*, 17(1):46–49.

[168] Tacconelli, E., Carrara, E., Savoldi, A., Harbarth, S., Mendelson, M., Monnet, D. L., Pulcini, C., Kahlmeter, G., Kluytmans, J., Carmeli, Y., et al. (2018). Discovery, research, and development of new antibiotics: the who priority list of antibiotic-resistant bacteria and tuberculosis. *The Lancet Infectious Diseases*, 18(3):318–327.

[169] Takatori, S. C., De Dier, R., Vermant, J., and Brady, J. F. (2016). Acoustic trapping of active matter. *Nature communications*, 7:10694.

[170] Thompson, A. G., Tailleur, J., Cates, M. E., and Blythe, R. A. (2011). Lattice models of nonequilibrium bacterial dynamics. *Journal of Statistical Mechanics: Theory and Experiment*, 2011(02):P02029.

[171] Tino, T. (1977). Genetics of structure and function of bacterial flagella. *Annual review of genetics*, 11(1):161–182.

[172] Tsagkari, E. (2017). *The role of physical and biological processes in biofilms in drinking water*. PhD thesis, University of Glasgow.

[173] van Duin, D. and Paterson, D. L. (2016). Multidrug-resistant bacteria in the community: trends and lessons learned. *Infectious Disease Clinics*, 30(2):377–390.

[174] Vicsek, T. and Zafeiris, A. (2012). Collective motion. *Physics Reports*, 517(3-4):71–140.

[175] Vidal, O., Longin, R., Prigent-Combaret, C., Dorel, C., Hooreman, M., and Lejeune, P. (1998). Isolation of an escherichia coli k-12 mutant strain able to form biofilms on inert surfaces: involvement of a new ompr allele that increases curli expression. *Journal of bacteriology*, 180(9):2442–2449.

[176] Vincenti, B., Douarche, C., and Clement, E. (2018). Actuated rheology of magnetic micro-swimmers suspensions: Emergence of motor and brake states. *Physical Review Fluids*, 3(3):033302.

[177] Wang, J. D. and Levin, P. A. (2009). Metabolism, cell growth and the bacterial cell cycle. *Nature Reviews Microbiology*, 7(11):822.

[178] Wang, Y., Hu, B., Diao, X., and Zhang, J. (2012). Antitumor effect of microbubbles enhanced by low frequency ultrasound cavitation on prostate carcinoma xenografts in nude mice. *Experimental and therapeutic medicine*, 3(2):187–191.

[179] Wensink, H. H., Dunkel, J., Heidenreich, S., Drescher, K., Goldstein, R. E., Löwen, H., and Yeomans, J. M. (2012). Meso-scale turbulence in living fluids. *Proceedings of the National Academy of Sciences*.

[180] Wiegand, I., Hilpert, K., and Hancock, R. E. (2008). Agar and broth dilution methods to determine the minimal inhibitory concentration (mic) of antimicrobial substances. *Nature protocols*, 3(2):163.

[181] Wijman, J. G., de Leeuw, P. P., Moezelaar, R., Zwietering, M. H., and Abee, T. (2007). Air-liquid interface biofilms of bacillus cereus: formation, sporulation, and dispersion. *Applied and environmental microbiology*, 73(5):1481–1488.

[182] Wiklund, M., Green, R., and Ohlin, M. (2012a). Acoustofluidics 14: Applications of acoustic streaming in microfluidic devices. *Lab on a Chip*, 12(14):2438–2451.

[183] Wiklund, M., Green, R., and Ohlin, M. (2012b). Acoustofluidics 14: Applications of acoustic streaming in microfluidic devices. *Lab Chip*, 12:2438–2451.

[184] Wilking, J. N., Zaburdaev, V., De Volder, M., Losick, R., Brenner, M. P., and Weitz, D. A. (2013). Liquid transport facilitated by channels in bacillus subtilis biofilms. *Proceedings of the National Academy of Sciences*, 110(3):848–852.

[185] Wioland, H., Lushi, E., and Goldstein, R. E. (2016). Directed collective motion of bacteria under channel confinement. *New Journal of Physics*, 18(7):075002.

[186] Wioland, H., Woodhouse, F. G., Dunkel, J., Kessler, J. O., and Goldstein, R. E. (2013). Confinement stabilizes a bacterial suspension into a spiral vortex. *Physical review letters*, 110(26):268102.

[187] Wood, T. K., Barrios, A. F. G., Herzberg, M., and Lee, J. (2006). Motility influences biofilm architecture in escherichia coli. *Applied microbiology and biotechnology*, 72(2):361–367.

[188] Woodford, N. and Ellington, M. J. (2007). The emergence of antibiotic resistance by mutation. *Clinical Microbiology and Infection*, 13(1):5–18.

[189] Yazdi, S. and Ardekani, A. M. (2012). Bacterial aggregation and biofilm formation in a vortical flow. *Biomicrofluidics*, 6(4):044114.

[190] Yosioka, K. and Kawasima, Y. (1955). Acoustic radiation pressure on a compressible sphere. *Acta Acustica united with Acustica*, 5(3):167–173.

[191] Zhang, X., Ashida, E., Shono, S., and Matsuda, F. (2006). Effect of shielding conditions of local dry cavity on weld quality in underwater nd: Yag laser welding. *Journal of Materials Processing Technology*, 174(1-3):34–41.

[192] Zhao, Y.-Z., Lu, C.-T., Li, X.-K., and Cai, J. (2013). Ultrasound-mediated strategies in opening brain barriers for drug brain delivery. *Expert opinion on drug delivery*, 10(7):987–1001.

[193] Zimmer, C. (2012). *Microcosm: E-coli and the New Science of Life*. Random House.